PHYSIK-DEPARTMENT

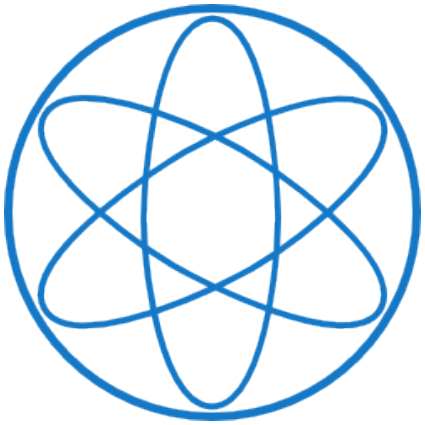

Supramolecular Templates -

Routes Towards Steering Assembly and Electronic Properties at the Nanoscale

Dissertation von

Wolfgang Benedikt Krenner

TECHNISCHE UNIVERSITÄT MÜNCHEN

TECHNISCHE UNIVERSITÄT MÜNCHEN

Lehrstuhl E20

Molekulare Nanowissenschaften & Chemische Physik von Grenzflächen

Supramolecular Templates -

Routes Towards Steering Assembly and Electronic Properties at the Nanoscale

Wolfgang Benedikt Krenner

Vollständiger Abdruck der von der Fakultät für Physik der Technischen Universität München zur Erlangung des akademischen Grades eines Doktors der Naturwissenschaften (Dr. rer. nat.) genehmigten Dissertation.

Vorsitzender:	Univ.-Prof. Dr. Peter Vogl
Prüfer:	**1.** Univ.-Prof. Dr. Johannes Barth
	2. Univ.-Prof. Dr. Sebastian Günther

Die Dissertation wurde am 21.03.2012 bei der Technischen Universität München eingereicht und durch die Fakultät für Physik am 14.05.2012 angenommen.

Abstract

Driven by ever decreasing feature sizes in technological applications, over the past 20 years the field of nanotechnology and -fabrication has emerged. In an effort to gain ultimate control over matter at the molecular and atomic level, techniques employing the self-assembly capabilites of functionalized molecular building blocks have shown to provide a promising, alternative route. Opposed to top-down fabrication protocols, like electron beam lithography or nanoprinting, a bottom-up approach, where molecules are chosen as constituents for the spontaneous formation of nanoarchitectures, offers a fast, parallel and simple fabrication process.

To explore routes towards gaining control over matter at the nanoscale, here, the assembly and organization of different molecular and atomic species on the monocrystalline Ag(111) noble metal surface was studied. The evolving superstructures were studied by scanning tunneling microscopy (STM) and spectroscopy (STS) at liquid helium temperatures in ultra-high vacuum. First, a study of molecular nanogratings and monolayers, self-assembled from N,N'-diphenyl oxalic amide (DOA) is presented. To further explore the functionalization capabilities of the nanostructures, they were exposed to atomic cobalt, leading to a site-selective adsorption and organization process of the single metal atoms. In the next step, molecular bi-component networks self-assembled from sexiphenyl dicarbonitrile (SDC) and DOA molecules, following a hierarchic formation protocol, were investigated. The experimental findings were further complemented by modeling the exact network geometry on the surface at the molecular and atomic scale as well as by theoretical simulations making it possible to identify the hierarchy inducing energetics of the system. Finally, the confinement of the quasi-free 2D surface state electrons on Ag(111) via molecular networks was studied. By reducing the dimensionality of the free electron movement to first 1D via the molecular nanogratings from DOA and 0D by open-porous networks from SDC, quantum wire and quantum dot states evolve in the nanometer sized cavities. The scattering properties of the employed species was compared in detail, before the intricacy of measuring the local density of states in 2D via STM and STS is addressed.

Kurzfassung

Aufgrund der stetig fortschreitenden Miniaturisierung in technischen Anwendungen wurde in den letzten 20 Jahren das Forschungsgebiet der Nanotechnologie und -fabrikation geboren. Um die Kontrolle über Materie auf dem molekularen und atomaren Niveau zu erlangen, werden Fabrikationstechniken, denen die Selbstorganisation von funktionalisierten Grundbausteinen zu Grunde liegt, untersucht. Im Gegensatz zu sogenannten "Top-Down" Protokollen, wie Elektronenstrahl-Lithographie oder Stempeltechniken, stellen "Bottom-Up" Ansätze, bei denen einzelne Moleküle als funktionale Grundbausteine benutzt werden, eine schnelle, parallele und prozesstechnisch mitunter weniger anspruchsvolle Alternative dar.
Um Kontrolle über Materie auf der Nanoskala zu erreichen, wurden in dieser Arbeit die Anordnung und Organisation verschiedener molekularer und atomarer Konstituenten auf der monokristallinen Ag(111) Oberfläche untersucht. Die sich bildenden Nanoarchitekturen wurden durch Rastertunnelmikroskopie (STM) und -spektroskopie (STS) bei tiefen Temperaturen und im Ultrahochvakuum studiert. Zuerst wird eine Studie über molekulare Nanogitter und Monolagen, die durch die Selbstorganisation von N,N’-Diphenyl Oxalsäure (DOA) gebildet werden, vorgestellt. Um weitere Möglichkeiten zur Funktionalisierung dieser Template zu demonstrieren, wurde das selektive Adsorptionsverhalten von atomarem Kobalt untersucht. Weiter wurden molekulare Netzwerke aus Sexiphenyl Dicarbonitril (SDC) und DOA, deren Formierung ein hierarchischer Organisationsprozess zu Grunde liegt, untersucht. Die experimentellen Befunde wurden mit der Adsorptionsgeometrie und theoretischen Simulationen der verschiedenen Bindungsstärken komplementiert, wodurch die hierarchische Ordnung erklärt werden konnte. Zuletzt wird eine Studie über quasi-freie 2D Oberflächenelektronen auf Ag(111) präsentiert. Hierbei werden, durch die Limitierung der Elektronenbewegung in eine oder null Dimensionen, wohldefinierte Quantendraht und -punkt Zustände induziert. Der 1D Fall wird in molekularen Nanogittern aus DOA, der 0D Fall durch offenporige Netzwerke aus SDC realisiert. Die Eigenschaften der involvierten molekularen Streubarrieren wird detailliert dargelegt, bevor abschließend die Herausforderungen bei der Messung der lokalen Zustandsdichte in zwei Dimensionen mit dem STM diskutiert wird.

"You can look, but you better not touch."
- Bruce Springsteen

Contents

Chapter 1

Introduction

Ever since the semiconductor transistor was pioneered by Shockley, Bardeen and Brattain at the AT&T Bell Laboratories in 1947, for which they were awarded the Nobel Prize in Physics in 1956 [1], subsequent technological and scientific advances have led to functional structures with decreasing size and dimensionality. The idea of advancing research to the nanoscale, where atoms and molecules act as fundamental building blocks for applications, was first explored at the end of the 1950's by Feynman [2]. Thereafter, nanostructure science has seen rapid development over the last 50 years that was priorly unprecedented.

Advanced semiconductor nanostructures often rely on interface effects [3, 4]. For example, in field effect transistors, the voltage applied to a gate electrode controls the amount of charge at the interface between two materials. Thus, the conductivity of this transport channel can be tuned over orders of magnitude via this easily accessible control parameter. This property is the basis for the application of this prototype interface device which laid the foundation for their application in present day digital electronics. Since the motion of carriers can only occur in the two spatial directions perpendicular to the interface, rich fundamental physical effects have been studied in great detail in such systems, most notable the integer and fractional Quantum Hall Effects [5, 6].

1. INTRODUCTION

As the properties of interfaces are of crucial importance for a large variety of material systems and devices, they are often throughly investigated, leading to the discovery of intriguing physical effects. The fundamental cause thereby is often the symmetry breaking at interfaces and surfaces due to the abrupt change or end of a bulk material system. Thus, these boundaries can show completely different properties in terms of, for example, charge concentration and mobility than the bulk material.

For this reason, the investigation of surfaces and interfaces has sparked many scientific and technological advances in the past half century. Current challenges in surface science, nanotechnology and molecular chemistry are addressed by numerous experimental techniques being sensitive to structural changes at the atomic scale. The Scanning Tunneling Microscope (STM) and the Atomic Force Microscope (AFM) have proven to be very powerful and versatile tools for investigating surface morphologies as well as their electronic and magnetic properties with atomic precision. Therefore, STM and AFM are among the most prominent and widely recognized experimental techniques in physics, chemistry and biology studies focusing on surfaces and nanoscale objects thereon.

The operation principle of STM was first demonstrated by Binnig and Rohrer in 1982 [7], providing the capability of resolving surfaces with atomic precision. Since then, the STM has seen rapid development both concerning instrumentation and theoretical understanding. The development of this groundbreaking experimental technique led the Royal Swedish Academy to award Binnig and Rohrer with the Nobel Prize for Physics in 1986. Their Nobel lecture [8] was concluded by stating that "*The STM's* "*Years of Apprenticeship*" *have come to an end, the fundamentals have been laid, and the* "*Years of Travel*" *begin. We should not like to speculate where it will finally lead, but we sincerely trust that the beauty of atomic structures might be an inducement to apply the technique to those problems where it will be of greatest service solely to the benefit of mankind.*"

The "Years of Travel" have led the STM far in these past 30 years. The tunneling junction has proven capable to not only be a mere microscope with unrivaled resolution and precision, but has enabled scientists further

to investigate chemical processes involving single atoms and molecules [9, 10], study the electronic properties of complex solid interfaces like high temperature superconductors [11] and even explore inelastic processes such as single molecule vibrations [12] and spin dynamics [13].

The STM is also the technique of choice in the studies of supramolecular templates presented here. As the investigations are performed at interfaces themselves, the research area is also situated at the interface between physics and chemistry. Self-assembly and -organization processes are found in many natural and biological systems, therefore protocols employing these principles were proposed more than 20 years ago [14, 15]. By using molecules as building blocks to form extended, functional structures via self-assembly, a novel route to construct nanoarchitectures may be at hand. Since top-down fabrication techniques, well established for semiconductor structures, are facing limitations while approaching ever smaller feature sizes, realizing nanostructures via self-assembly proposes an intriguing alternative. First real-life applications like displays utilizing organic light emitting diodes [16] were already introduced several years ago and numerous devices incorporating single molecule transistors [17] or single molecule magnets as magnetic storage media and for spintronics applications [18] have been proposed, just to name a few. Spontaneous self-assembly of molecules into networks to host single-molecule devices is thereby a possible route for their real-life implementation.

In this study, the possibilities to use simple organic molecules as fundamental building blocks was explored. Network formation is driven by self-assembly protocols based on hydrogen bonding, metal-coordination bonding and hierarchic principles. Self-assembled networks and films of these molecules were produced on the Ag(111) noble metal surface by organic molecular beam epitaxy in ultra-high vacuum conditions and subsequently studied by STM at cryogenic conditions down to liquid-helium temperature. Thereby, routes towards steering the assembly of nanostructures with single atoms as the smallest conceivable organization unit, molecular templates following hierarchic assembly principles and the nanoscale control of surface electronic properties were explored. This thesis addresses current

challenges in nanoscience and investigates fundamental processes governing the formation and functionalization of the produced structures and the experimental techniques used to do so.

In the following (Chapter 2), fundamental theoretical aspects of scanning tunneling microscopy and spectroscopy are shortly recapitulated before surface electronic properties of materials and the driving principles of molecular self-assembly are briefly revised. Afterwards (Chapter 3), the experimental technique to employ the previously discussed physical phenomena is presented. The operation of a STM at cryogenic temperatures is illustrated, followed by a short description of the experimental setups. Thereby, first the low-temperature STM instrumentation used to perform subsequently discussed experiments, and finally the planning and realization of a novel setup allowing measurements at temperatures close to 1 K, that was built up over the course of the PhD project, is presented.

In the first experiment (Chapter 4) molecular nanogratings and films assembled from N,N' diphenyl oxalic amide are introduced and characterized. The possibility to use these templates for the controlled positioning of single cobalt atoms is studied by investigating the adsorption and distribution at variable preparation conditions.

In the second series of experiments (Chapter 5), the production and understanding of hierarchically organized, open-porous, bi-component networks from co-deposited para-sexiphenyl dicarbonitrile and N,N' diphenyl oxalic amide is investigated. The formed nanoarchitectures are first characterized by STM. After the initial characterization, detailed adsorption and binding patterns on the surface are elaborated and finally studied by numerical simulations to rationalize the hierarchic formation.

The third and final set of experiments (Chapter 6) illustrates the possibility of tuning surface electronic properties via molecular templates. Adsorbed molecules represent scattering barriers for the quasi-free 2D electron gas occupying the Ag(111) surface. Thus, surface electrons can be confined within nanogratings from N,N' diphenyl oxalic amide and open-porous networks assembled from para-sexiphenyl dicarbonitrile into 1D and 0D quantum systems, respectively. The confined respective quantum wire

and quantum dot states are first characterized for several confining structures, before the scattering properties of molecular ligands, different binding types and adsorbates positioned on the molecules are discussed in detail. In a final step, the intricacy of the two dimensional mapping of the local density of states on the surface via different experimental techniques is illustrated.

The final part (Chapter 7) summarizes the presented results and addresses still open questions as well as future perspectives and ideas.

Chapter 2

Theoretical Aspects

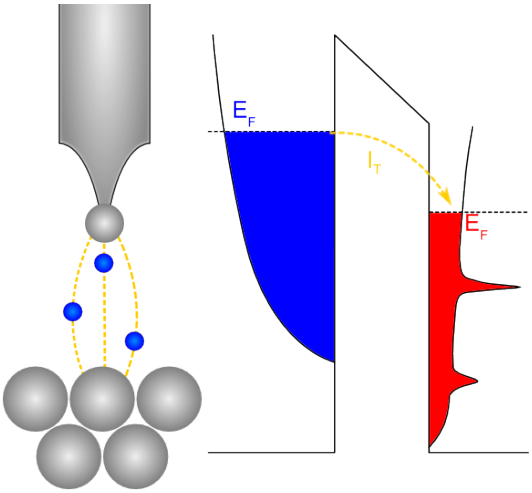

In this chapter the basic theoretical principles of scanning tunneling microscopy (STM) as well as the physical and chemical properties of the investigated samples will be considered. First the tunneling junction between the STM tip and the probed sample is discussed. Via the evaluation of the tunneling current, it will be further shown that the STM also offers the possibility of investigating the local density of states of surfaces and adsorbates. The next part will address the electronic properties of surfaces. As surfaces represent a break in symmetry from the bulk, their electronic properties can differ substantially from the bulk material. The confinement of quasi-free carriers into lower dimensions and at the nanoscale will be further discussed briefly. Finally, introductory remarks regarding molecular self-assembly leading to the formation of nanoarchitectures will be given.

2.1 Scanning Tunneling Microscopy

Ever since the first demonstration of the possibility to utilize the quantum mechanical tunneling current to image the reconstructed Au(110) and $CaIrSn_4$(110) surfaces with atomic precision by Binnig and Rohrer in 1982 [7], scanning tunneling microscopy (STM) and spectroscopy (STS) have evolved to be key tools in modern surface science. However in most experiments the STM tip, and alongside with it the tunneling junction, remain fragile and elusive. Since even small changes in the exact tip geometry and the adsorption of molecules influence its properties dramatically, it is important to discuss the tunneling junction in detail to rationalize how and why STM has become the powerful tool it is today.

2.1.1 The Tunneling Junction

The quantum nature of electrons allows the transfer of charge across a vacuum barrier when the separation between a metallic tip and a conductive substrate is small enough to result in an overlap of the electron wave functions on the tip and sample. In order to generate the tunneling current, a potential difference between the tip and sample is required, which is typically achieved by applying a bias to the substrate. Thereby, unoccupied states in the substrate or tip are created that electrons can tunnel into. Therefore, the effective tip-sample-separation can be increased to several Ångstroms.

This situation is depicted in Figure 2.1.1, where electrons from the tip can tunnel into unoccupied states of the substrate and therefore, a constant tunneling current is established.

2.1.1.1 The Tunneling Current

Since the first demonstration of the STM, several theoretical approaches towards understanding the tunneling current and the capabilities of STM with increasing levels of sophistication have been explored. The first and most basic consideration for the tunneling of electrons between two electrodes

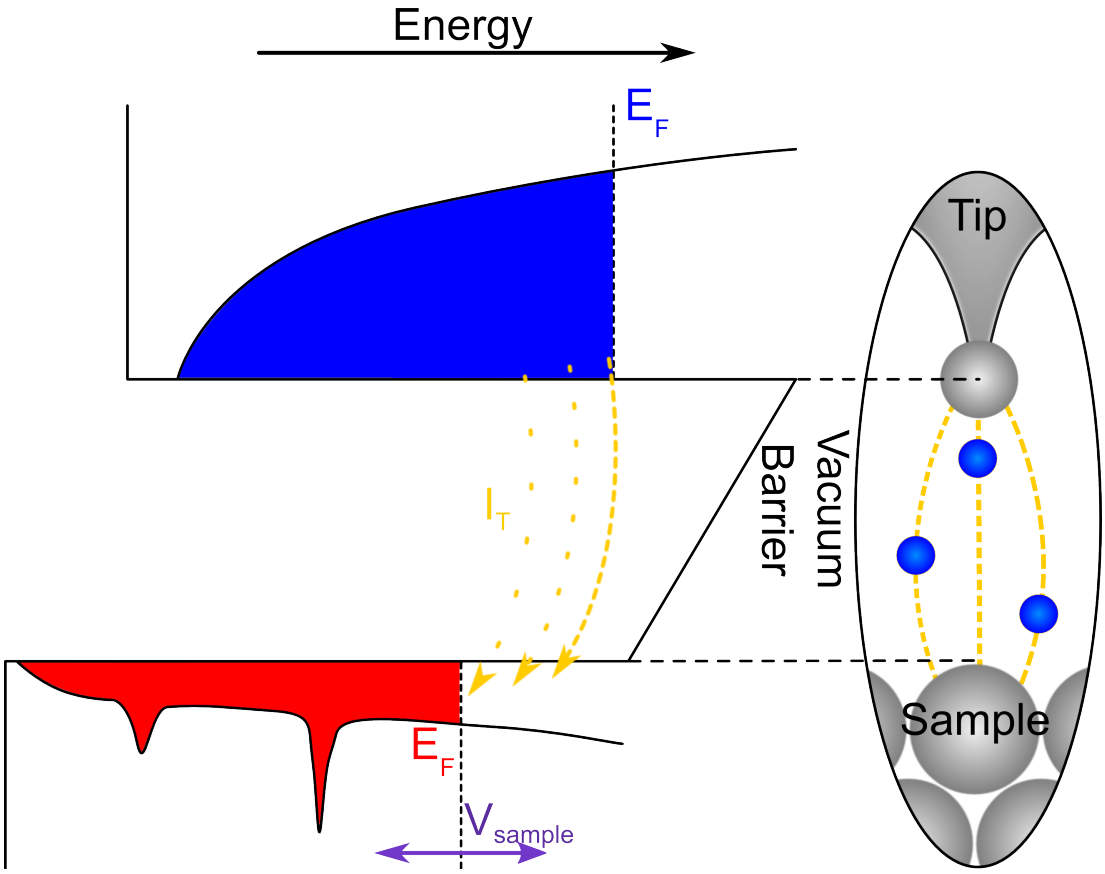

Figure 2.1.1: When a metallic tip is moved into close proximity of a conductive substrate, a quantum mechanical tunneling current I_T of electrons between tip and sample across the vacuum barrier can be established. In a first approximation, only electrons tunneling from the last atom at the tip apex into the substrate are considered. By applying a bias V_{sample}, the number of free states accessible for tunneling into can be tuned by realigning the respective Fermi energies $E_{F,tip}$ & $E_{F,sample}$.

separated by a insulating barrier was elaborated by Bardeen in 1961 [19] more than 20 years before the first operational STM. There, in a first order the tunneling current between two planar electrodes is given as:

$$I = \frac{2\pi e}{\hbar} \sum_{\mu,\nu} f(E_\mu)\,[1 - f(E_\nu + eV)]\,|M_{\mu,\nu}|^2\,\delta(E_\mu - E_\nu) \tag{2.1.1}$$

Thereby, the tunneling current I is described as the sum of the overlap of the respective wave functions of electrons on the two electrodes μ and ν

where an external bias V is applied to electrode ν. The states ψ_μ and ψ_ν are linked by the tunneling matrix element $M_{\mu,\nu}$ where the square of the $M_{\mu,\nu}$ gives the tunneling probability between states μ and ν at the energy $E_{\mu,\nu}$, which is finally taken into account by the δ function. This very general approach includes solutions where reverse tunneling at high temperatures and in the limits of very high external bias are included.

To retrieve an analytic solution, Tersoff and Hamann [20, 21] shortly after the demonstration of STM elaborated a theory for small voltage and temperature. Here, the tunneling current I reduces to

$$I = \frac{2\pi}{\hbar} e^2 V \sum_{\mu,\nu} |M_{\mu,\nu}|^2 \, \delta(E_\nu - E_F) \, \delta(E_\mu - E_F) \tag{2.1.2}$$

where E_F represents the Fermi energy (which is assumed to be identical on the tip and substrate), e is the electron charge, and $\hbar$ is the Planck constant h divided by 2π. The delta functions only regard states at E_F and the voltage dependence reduces to a linear factor increasing the tunneling current. They further showed that for a spherical tip geometry with a known curvature R, a spherically modeled tip potential (s-wave) at a given position $\vec{r}_0$ and a constant density of states on the tip, the tunneling current is greatly trivialized to

$$I \propto \sum_{\nu} |\psi_{\nu(\vec{r}_0)}|^2 \, \delta(E_\nu - E_F) \tag{2.1.3}$$

since it only depends on $|\psi_{\nu(\vec{r}_0)}|^2$ which represents the local density of states of the surface at $\vec{r}_0$ and the delta function again accounts for tunneling at E_F. This in turn also illustrates the fact, that with STM rather the surface electronic density of states is imaged than the pure surface morphology. So when scanning the tip, the experimental observations are always a convolution of the actual surface topography and the local density of states (which, for example, can be observed directly in mixed systems with strong charge localization at individual positions in the compound, see References [22, 23, 24]).

Tersoff and Hamann have further shown that Equation (2.1.2) can be evaluated when the tunneling matrix element $M_{\mu,\nu}$ is handled properly. This

yields the sensitivity of the tunneling current I with respect to the distance between the surface and the center of the tip curvature $R + d$:

$$I \propto exp(-2\kappa(R + d)) \tag{2.1.4}$$

Here κ is the minimum inverse decay length for the tip and sample wave functions in vacuum

$$\kappa = \sqrt{\frac{2m\phi}{\hbar^2}} \tag{2.1.5}$$

with ϕ being the work function for electrons to reach the vacuum level and m the electron mass. Equation (2.1.4) actually explains the high vertical sensitivity of the STM, since the tunneling current I exponentially depends on the tip-sample separation. However, this first approach by Tersoff and Hamann [20] could not explain the high lateral resolution for STM that was later demonstrated on close-packed metal surfaces like Au(111), Al(111) or Cu(100) [25, 26, 27, 28]. In the spherical tip approach, the lateral resolution can be estimated roughly as

$$W = \sqrt{2 \cdot \frac{R + d}{\kappa}} \tag{2.1.6}$$

which for realistic experimental parameters of R = 10 Å, d = 5 Å and $2\kappa^{-1} = 1.6$ Å yields a lateral resolution of ∼5 Å, which is significantly lower than, e.g., the 2.5-3 Å nearest neighbor distance on fcc noble metal surfaces. However, this is not sufficient for atomic or intramolecular resolution in many cases, which would require $R + d \lesssim 3.5$ Å, i.e., a tunneling current out of a single atom which is scanned 1 Å above the surface.

Therefore, more sophisticated attempts to describe the tunneling current trajectory, including contributions from specific sample and tip orbital overlaps and an atom-on-jellium model for tip and surface have been undertaken shortly after these first theoretical considerations. In a semi classical approach Das and Mahanty [29] investigated the contribution of the underlying surface area to the tunneling current onto a spherical tip via reducing the Wenzel-Kramers-Brillouin approximation. By investigating only

one-dimensional tunneling, the wave function of the tunneling particle is

$$\psi = exp\left(\frac{i}{\hbar}[\sigma(\vec{r}) - Et]\right) \tag{2.1.7}$$

in which $\sigma(\vec{r})$ is obtained from the Schrödinger equation

$$(\bigtriangledown\sigma)^2 - i\hbar\bigtriangledown^2\sigma = 2m[E - V(\vec{r})] \tag{2.1.8}$$

where E and V are the total energy of the particle and the potential energy of the tunneling particle, respectively. Therefore, the particles must after expansion and evaluation of σ to the first order of $\hbar$ satisfy the boundary conditions

$$(\bigtriangledown\sigma_0)^2 = 2m[E - V(\vec{r})], \tag{2.1.9}$$

$$(\bigtriangledown\sigma_1 \cdot \bigtriangledown\sigma_0) = \frac{1}{2}\bigtriangledown^2\sigma_0. \tag{2.1.10}$$

The formal solution to Equation (2.1.9) is

$$\sigma_0(\vec{r}) = \sigma_0(\vec{r}_0) + \int_{s_0}^{s} ds\sqrt{2m[E - V(\vec{r})]} \tag{2.1.11}$$

for a tunneling particle moving from one electrode $\vec{r}_0$ to the other $\vec{r}$ through the forbidden vacuum region along the path integral ds. By evaluating the integral paths and only accounting for particles tunneling from the tip to the surface, due to an external bias, a localization of the tunneling current along the tunneling axis is observed leading to an increased lateral resolution.

Further, if one takes into account not only s-wave tips as in the Tersoff-Hamann approach, an intuitive picture of a further increase in resolution based on electronic states and their orbitals localized on the tip, that can exclusively tunnel into appropriate states on the surface, can be given.

Chen [30] investigated this scenario for a tungsten tip that is scanned across a close-packed metal surface. Since most materials used as tips are d-band metals, close to E_F 85% of the density of states originates from d states. Tungsten as the material most commonly used for UHV STM tips forms highly localized metallic d_{z^2} dangling bonds on its surface for small clusters and therefore, it is more sensitive due to the orbital symmetry of

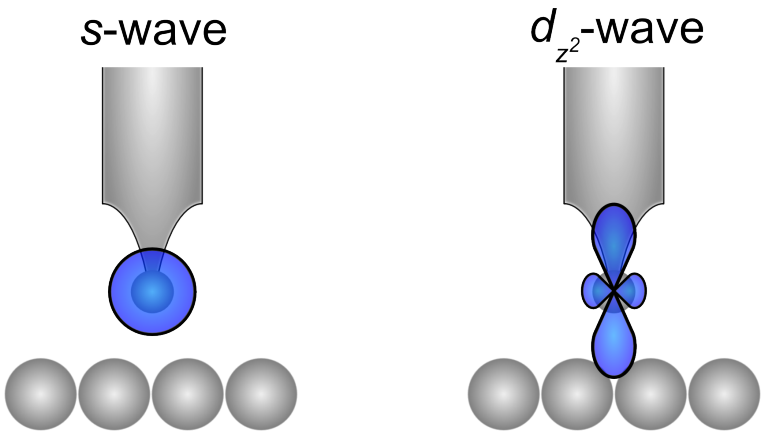

Figure 2.1.2: Schematic illustrating the impact of a *s*-wave and a *d*-wave tip on the lateral resolution capabilities of a STM tip. Due to the more localized nature of the d_{z^2} wave tip below the tip apex, higher lateral resolution is achieved when compared to a pure *s*-wave tip.

the electronic state mostly involved while tunneling. A schematic to illustrate this effect is given in Figure 2.1.2.

It was concluded that *d*-band metals, via d_{z^2} and p_z orbitals localized on small clusters at the tip apex, are capable of providing atomic resolution. The dependence on the metal cluster and therefore tip morphology also explains the strong changes in resolution induced by tip restructuring. The reasoning behind this is the superposition of the surface charge density and the d_{z^2} or p_z orbitals, respectively. The surface charge density of a hexagonal lattice is given up to the lowest nontrivial Fourier component by

$$\rho(\vec{r}) = \sum_{E \leq E_f} |\psi(\vec{r})|^2 \simeq a_o(z) + a_1(z)\phi^{(6)}(\vec{x}) \tag{2.1.12}$$

where

$$\phi^{(6)}(\vec{x}) \equiv \frac{1}{3} + \frac{2}{9}\sum_{j=0}^{2} cos(\vec{\omega}_j \cdot \vec{x}),$$

$$\text{with} \quad \vec{\omega}_0 = (0,1), \quad \vec{\omega}_1 = (-\frac{1}{2}\sqrt{3}, -\frac{1}{2}),$$

$$\text{and} \qquad \vec{\omega}_2 = (\frac{1}{2}\sqrt{3}, -\frac{1}{2})$$

is the hexagonal cosine function with maximum value 1 at each atomic site and minimum value 0 at each hollow site. The $a_0(z)$ term in (2.1.12) is mainly given by the Bloch function near the $\bar{\Gamma}$ point with the lowest Fourier component

$$\psi_{\bar{\Gamma}} \sim exp(-\kappa z) \Rightarrow a_0(z) \propto exp(-2\kappa z). \tag{2.1.13}$$

The superposition of the surface potential with the spherical harmonics of the tip wave function then allows for the numerical simulation of the tunneling current at given tip-sample separation. The comparison with experimental data yielded good agreement with this approach, demonstrating localized metallic surface tip states to be essential for high lateral resolution.

Ultimately, the resolution in STM is dictated by the shape of the metal cluster on the tip used to tunnel from and the chemical identity of the last atom on the tip. In more advanced techniques, single molecules like CO functionalize the tip-sample-junction via providing defined orbitals [31]. Through thorough tip preparation techniques and tip functionalization, intramolecular features and structures have thereby been resolved.

2.1.1.2 Local Density of States in Differential Conductance

As was already established in Equation (2.1.3), the tunneling current is sensitive to the local density of states at the surface. Since very localized surface areas contribute to the tunneling current, STM is, apart from merely delivering topographic information on the atomic scale, also capable of probing surface electronic properties with the high lateral precision.

This is intuitively clear, since the tunneling current should increase or decrease when charge is not equally distributed on the surface, while the tip is scanned at a constant tip-sample separation. In a case, where the local density of states is spatially modulated, the topographic real space image is convoluted with the local current density. The reason for this can be illustrated if a different nomenclature for the tunneling current, such as employed by Selloni et al. [32] or Lang [33], is regarded, in which the tunneling matrix element $|M_{\mu,\nu}|^2$ and therefore the tunneling probability T is assumed as constant:

$$I \propto \int_{E_F}^{E_F+V} dE\ \rho_T(E-V)\ \rho_S(\vec{r}_T, E) \tag{2.1.14}$$

In this description analogous to the one by Tersoff and Hamann [20, 21], the tunneling current I in the low external voltage regime is proportional to the integral over the product of the density of states on the tip ρ_T and the local density of states on the surface ρ_S at the tip location $\vec{r}_T$. Here the Fermi energy E_F is the same on both sides of the junction, therefore, the energy range under consideration is $[E_F \cdots E_F + V]$. For metallic tips under the assumption of a featureless and constant density of states, the integral trivializes to only considering the surface density of states. In this case the differential conductance dI/dV is a direct measure for the local density of states:

$$\frac{dI}{dV} = \frac{d\int_{E_F}^{E_F+V} dE\ \rho_S(\vec{r}_T, E)}{dV} \propto \rho_S(\vec{r}_T, E_F+V) \tag{2.1.15}$$

However, it has to be noted that this assumption is only valid for low voltages since otherwise the tunneling probability cannot be assumed as constant and further corrections have to be taken into account to compensate for this. This scenario is discussed in detail by Hamers [34] or by Kubby and Boland [35]. It has to be further noted that this consideration is only true for a stationary tip with constant tip-sample separation and lateral position.

2.2 Surface Electrons

Symmetry breaking and missing nearest neighbor atoms lead to manifold special electronic properties of surfaces and interfaces. Due to the missing nearest neighbors, dangling bonds, e.g., lead to the reconstruction of semiconductor surfaces and in special cases, the lack of inversion symmetry can lead to effects like strong spin-orbit coupling and splitting. Since the STM tip, while scanning, follows rather the convolution of the LDOS and the actual topography, it is important to consider the surface electronic properties of the investigated solid. Therefore, a short introduction into the theory of surface electrons in contrast to bulk electrons will be given (a more complete summary was elaborated by N. Memmel [36], upon which the following considerations are based).

The basic approach to electronic structure calculations is solving the single-electron Schrödinger equation

$$\left(-\frac{1}{2}\nabla^2 + V(\vec{r})\right)\ \phi(\vec{r}) = E\ \phi(\vec{r}) \tag{2.2.1}$$

for a three dimensional periodic potential, which can be written as a Fourier series:

$$V(\vec{r}) = \sum_{\vec{G}} V_{\vec{G}}\ exp(-i\vec{G}\vec{r}) \tag{2.2.2}$$

Here, $\vec{G}$ denotes the 3D bulk reciprocal lattice vectors. The solutions for the Schrödinger equation have to be of the form of Bloch waves, which are characterized by the 3D wave vector $\vec{k}$:

$$\begin{aligned} \phi_{\vec{k}}(\vec{r}) &= e^{i\vec{k}\vec{r}}\ U_{\vec{k}}(\vec{r}) \\ &\text{with} \quad U_{\vec{k}}(\vec{r}) = \sum_{\vec{G}} u_{\vec{k}\vec{G}}\ e^{-i\vec{G}\vec{r}} \end{aligned} \tag{2.2.3}$$

Finally, by introducing the difference $\vec{k}-\vec{G}$ the set of solutions from Equation (2.2.1) for the Fourier coefficients $u_{\vec{k}-\vec{G}}$ is:

$$u_{\vec{k}-\vec{G}} = -\frac{\sum_{\vec{G}'\neq\vec{G}} V_{\vec{G}-\vec{G}'}\ u_{\vec{k}-\vec{G}'}}{\frac{1}{2}(\vec{k}-\vec{G})^2 + V_0 - E} \tag{2.2.4}$$

For bulk solids these solutions deliver sets of solutions, the well known band structures. However, when surfaces are taken into account, the boundary conditions change, since at the solid-vacuum interface the infinitely extended potential of the bulk ends. Due to this symmetry breaking the electronic structure of the surface must differ from the bulk. This can be described theoretically by a semi-infinite solid. Here, the crystal and vacuum region are evaluated independently and a wave function matching method is used to calculate the DOS on the surface. A schematic for this is shown in Figure 2.2.1.

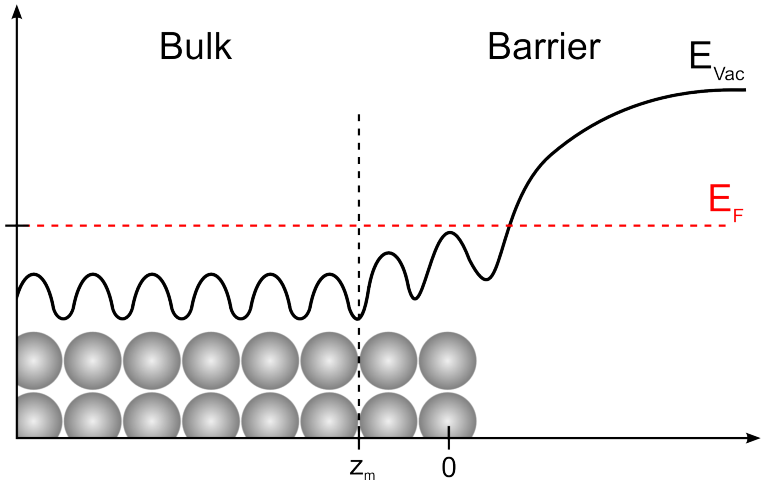

Figure 2.2.1: Schematic illustrating the wave function matching for the electronic potential leaving the bulk going into the vacuum. Adapted from [36]

For the theoretical approach to describe a solid interface the bulk is usually chosen to occupy the half-space $z < 0$, with the center of the outer most atom at $z = 0$. The region for $z < z_m$ is then the crystal described as an infinite solid, whereas $z > z_m$ is the barrier region. The Schrödinger equation is then solved independently for these two regions in a first step. The main difference for both regions thereby is that in the crystal the potential $V(\vec{r})$ is periodic in three dimensions, while $V(\vec{r})$ is only periodic in the two dimensions of the surface plane for the barrier and vacuum region.

Since the crystal region cannot be distinguished from the infinite solid, the wave function in this region again can be written as a linear combination

of 3D Bloch waves $\Phi_{\vec{k}}(\vec{r})$. However, to account for the interface region, the reciprocal vector k_z differs from the original set, therefore the wave function has the form:

$$\Psi^C_{\vec{k}_\parallel}(\vec{r}) = \sum_{\vec{k}=(\vec{k}_\parallel,k_z)} \varphi_{\vec{k}}\ \Phi_{\vec{k}}(\vec{r}) \tag{2.2.5}$$

The projection of the 3D bulk reciprocal vectors onto the surface then yields the 2D surface reciprocal lattice vectors $\vec{k}_\parallel$. This enables the reformulation of the above equation in terms of the surface lattice reciprocal vectors:

$$\Psi^C_{\vec{k}_\parallel}(\vec{r}) = e^{i\vec{k}_\parallel\vec{r}_\parallel} \sum_{\vec{G}_\parallel} e^{-\vec{G}_\parallel\vec{r}_\parallel}\ C_{\vec{k}_\parallel-\vec{G}_\parallel}(z) \tag{2.2.6}$$

Here $C_{\vec{k}_\parallel-\vec{G}_\parallel}(z)$ is built up from Fourier coefficients as in Equation (2.2.4) with the appropriate surface reciprocal vectors and expansion coefficients $\varphi_{\vec{k}}$. Due to the symmetry breaking, the Bloch waves with complex $k_z = p - iq$ now also yield solutions for $q > 0$ with wave functions of the form $\Phi_k(\vec{r}) = e^{qz}e^{ipz}e^{i\vec{k}_\parallel}\vec{r}_\parallel u_k(\vec{r})$. These so-called evanescent waves have a finite amplitude at the matching plane $z = z_m$ and decay exponentially into the bulk.

For the barrier region $z > z_m$ the proceeding to find solutions is similar to the bulk case. The periodic potential is now only defined on the surface in two dimension:

$$V(\vec{r}) = \sum_{\vec{G}_\parallel} V_{\vec{G}_\parallel}(z)\ e^{-i\vec{G}_\parallel\vec{r}_\parallel} \tag{2.2.7}$$

The wave functions for this region are determined as

$$\Phi^B_{\vec{k}_\parallel}(\vec{r}) = e^{i\vec{k}_\parallel\vec{r}_\parallel} \sum_{\vec{G}_\parallel} B_{\vec{k}_\parallel-\vec{G}_\parallel}(z)\ e^{i\vec{G}_\parallel\vec{r}_\parallel} \tag{2.2.8}$$

where the Fourier coefficients $V_{\vec{G}_\parallel}(z)$ and $B_{\vec{k}_\parallel-\vec{G}_\parallel}(z)$ depend on the distance z from the surface. Finally, to determine the unknown Fourier expansion coefficients in the crystal and barrier region, a wave function boundary matching and normalization technique is employed, which will however not be discussed in any further detail (see [36]).

For the Ag, Cu and Au (111)-surfaces this method delivers a special solution, leading to surface states in the gaps of the bulk band structure. Calculations show that surface state electrons on this surface behave nearly as

in a 2D free electron gas. The solution of the Schrödinger equation makes the origin of this effect clear. The wave function for the barrier region is a standing wave that decays exponentially when moving further into the bulk, whereas, in vacuum also an exponential decay however of an evanescent wave is observed. The solution in the surface plane is a plane wave, showing that electrons can move as in a free electron gas on the surface plane. The maximum of charge distribution along the z-axis is situated above the crystal surface. The quasi-free 2D electron gas on Ag(111) shows a parabolic dispersion relation

$$E = \frac{\hbar^2 k_{\parallel}^2}{2m^*} \tag{2.2.9}$$

with the effective mass $m^* = 0.4$ m_e, where m_e is the free electron mass, and the Fermi wave vector for the dispersion crossing the Fermi level being $k_F = \pm 0.08$ Å^{-1}, as was determined experimentally [37]. This then renders the Fermi surface for 2D quasi-free electron states as circles with a radius of k_F centered around the $\overline{\Gamma}$ point.

In STM and STS experiments this effect is observed in the unperturbed case by a step-like onset of the 2D surface state at ~ -67 mV, whereas the plane wave character of the surface electrons can be observed in standing wave patterns close to step edges (both cases are show in Figure 2.2.2) where the electron waves are reflected. The superposition of incoming and reflected electrons produces the observed standing wave pattern.

Due to thermal broadening at finite temperature, as well as experimental effects induced by lock-in technique and spatial drift (thermally, mechanically or piezo-creep induced), the line shape of the onset energy for the 2D free electron gas is slightly broadened. However, the center of the broadened ascent is situated at the expected energy of ∼-67 mV.

2.2.1 Confinement of Surface Electrons

When electron movement is restricted by reducing the dimensions along which electrons can propagate freely, the confinement to lower dimensions has a strong impact on the density of states. This effect is schematically

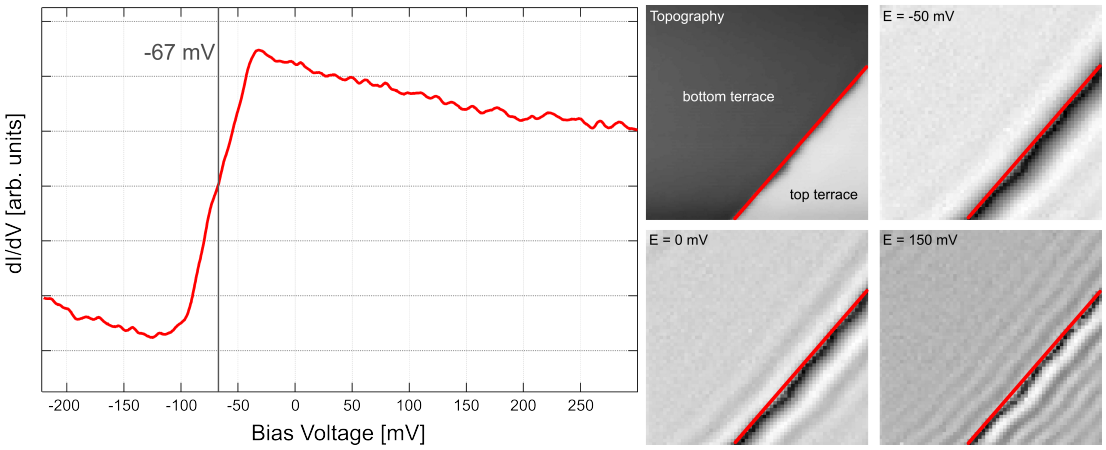

Figure 2.2.2: Exemplary STS data illustrating the 2D free electron gas character of surface electrons on Ag(111). Left: in a single point spectrum taken in the center of an extended terrace the onset of the surface state at ∼-67 mV can be clearly observed. The deviation from the theoretical sharp step-like increase is attributed to thermal broadening at finite temperature. Right: Standing wave patterns observed at an atomic step edge (indicated by a red line). With increasing energy higher order reflections are observed.

shown in Figure 2.2.3. Thereby, the step-like behavior observed for the quasi-free 2D surface state on Ag(111) can be easily understood.

An approach utilized to confine 2D surface state electrons to lower dimensions is the controlled positioning of adsorbates or the epitactical growth of nanostructures. Metallic islands can be grown in nanometer sizes [38], single atoms can be positioned into geometric arrangements [39] or molecules can self-assemble into regular patterns [40, 41], all of which confine the propagation of electrons across the surface plane and act as scatterers.

The example shown in Figure 2.2.2 was already thoroughly investigated, e.g. by Bürgi et al. [42], and a distinctive difference in the scattering behavior for ascending and descending step edges was found. For descending and ascending steps a reflectivity coefficient of $\rho_{\mathrm{desc}} = 0.85$ and $\rho_{\mathrm{asc}} = 0.5$ was determined, respectively. This finding already indicates that the exact geometry and electronic properties of adsorbates have to be taken into account when the confinement of surface charge carriers is investigated.

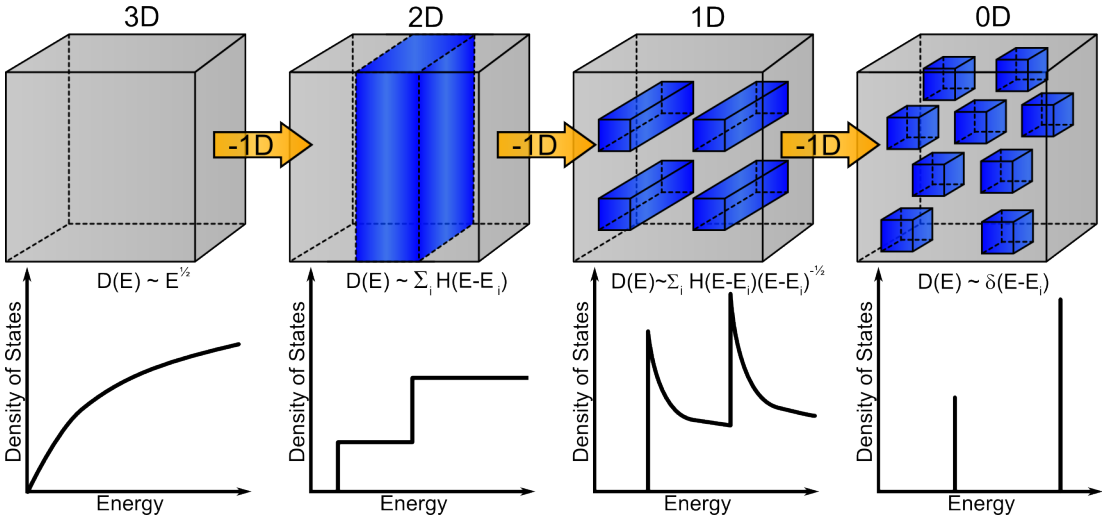

Figure 2.2.3: When electron movement is confined to lower dimensions, the density of states $D(E)$ changes distinctively. 3D: $D(E) \propto E^{1/2}$; 2D: $D(E) \propto \sum_i H(E - E_i)$; 1D: $D(E) \propto \sum_i H(E - E_i) \cdot (E - E_i)^{-1/2}$; 0D: $D(E) \propto \delta(E - E_i)$.

When confining nanostructures are constructed via molecular ligands on the Ag(111) surface, the quasi-free surface electrons can be investigated as particles-in-a-box, whose treatment is well known from quantum mechanics [43]. The situation for a infinite 1D potential confining electrons is schematically illustrated in Figure 2.2.4. The confined states (blue) within two potential landscapes (black), featuring different widths W_1 & W_2, are described as standing waves within these potential barriers. When the potential width is decreased from W_1 (left) to W_2 (right), the onset and spacing of the confined states increases, e.g. ΔE_1. The energetic positioning of the bound states scales with the potential width W and order of the bound state n according to $E_n \propto \frac{1}{W^2} \cdot n^2$. When finite potential heights are considered, the wavefunctions of the bound states are no longer completely confined within the potential barriers. Rather, as the energy approaches the potential height, the wavefunctions extend into the potential. Thereby, tunneling between adjacent potential wells will set in with increasing energy leading to a coupling between the states. Similar effects can be observed for surface state electrons when they are confined within spatially extended,

periodic nanoarchitectures.

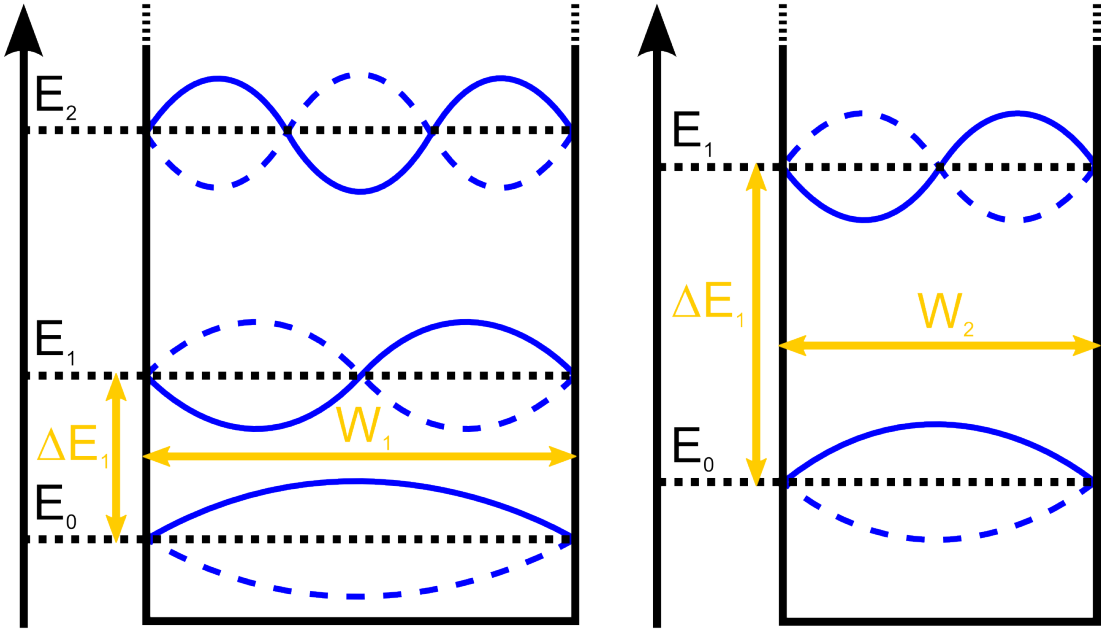

Figure 2.2.4: Schematic illustrating the effect of quantum confinement in a 1D quantum well with infinitely high barriers. With decreasing potential width, the onset and spacing of confined electron states shifts up in energy, reducing the amount of bound states in a finite quantum well.

In a more sophisticated approach, Boundary Element Method calculations based on Green's functions are carried out [44] in which the potential landscape of the adsorbate geometry is transferred as boundary conditions onto a planar patterned surface representing the 2D-FEG. Therefore, the potential landscape is constructed from homogeneous regions of constant potential with their boundaries being considered as abrupt for simplicity. In this framework the Schrödinger equation is solved for each individual element. Finally, by finding physically reasonable evaluations of the functions across the boundaries, the LDOS of the total system at a given energy is obtained. Thereby, the spatial distribution of electrons under the confining effects of potential barriers can be simulated. This method was employed in various simulations for electron confinement on Ag(111) discussed in Chapter 6. The details for the BEM method can be found in Reference [44].

2.3 Molecular Self-Assembly

In this work, several approaches for the realization of functional nanostructures and templates have been utilized, all of them based on the self-assembly of molecular building blocks. Therefore, the physical and chemical processes governing molecular movement and self-assembly will be addressed shortly.

2.3.1 Adsorption and Diffusion of Molecules

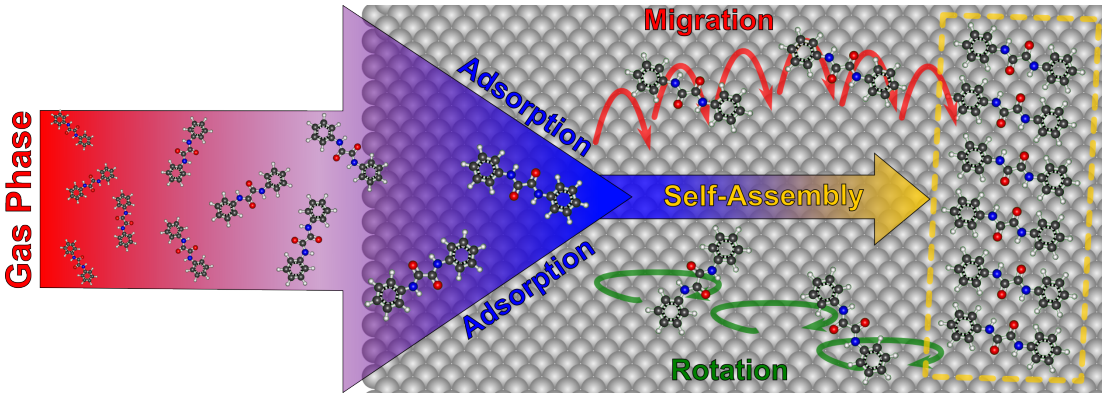

Figure 2.3.1: Schematic illustrating the processes involved during self-assembly. After adsorption, molecules migrate across the surface along with rotational movement, before substrate-mediated and direct lateral interactions between ligands lead to the formation of self-assembled structures.

When molecules or single atoms reach a crystal surface after propagating through vacuum, their subsequent motion depends on the energy stored in the phonon bath and chemical properties of the crystal as well as the kinetic and thermal energy of the adsorbing species. The latter can either stick to the surface, where excess kinetic and thermal energy is dissipated, or desorb again into the gas phase without sticking to the surface. Adsorbate energy is typically transferred directly to the phonon bath of the crystal, rarely other dissipation channels, e.g. radiation or electron emission, interfere. In terms of self-assembly, diffusion and rotation are the most essential of the

mentioned processes, since the ability of adsorbate migration is crucial for the ability of forming self-organized structures. After the initial adsorbate energy from thermal evaporation is dissipated rapidly, the energy provided by the crystal phonon bath, given mainly by the substrate temperature, is the most essential energy contribution to be considered here. Further, upon adsorption, the mobility and accessible vibrational states of atoms and molecules are dictated by the surface binding. Thereby, the lateral and rotational degrees of freedom of adsorbates are limited and determine the capability of adsorbate motion.

In a simple hopping model, surface diffusion takes place as an aleatoric walk of isolated adspecies from one adsorption site to another, once the system is in thermal equilibrium. The tracer diffusion coefficient D^* then follows an Arrhenius law if the thermal energy of the system $k_B T$ is very small compared to the migration energy barrier E_M that has to be overcome to perform a hopping step [45, 46, 47]:

$$D^* = \frac{1}{2d} \langle\lambda\rangle^2 \nu_0 \, exp(-\beta E_M) \equiv D_0^* \, exp(-\beta E_M) \tag{2.3.1}$$

Here ν_0 is the attempt frequency, D_0^* is the prefactor for tracer diffusion and $\beta = (k_B T)^{-1}$ indicates the temperature dependence. The same dependency holds true for the rotational motion of complex molecules, anchored to the surface or confined within a host lattice.

The statement above, however, is correct only for isotropic surfaces. More complex surfaces, such as vicinal surfaces or patterned templates, have to be considered more thoroughly. The diffusion barrier E_m my vary strongly along specific spatial directions of anisotropic surfaces, which needs to be considered in calculations regarding the mobility of adsorbates. Since many effects such as coordination bonding, covalent bonding at specific sites or preferential alignment along selected surface orientations may contribute, a complete study and description even of model systems is often non-trivial.

2.3.2 Theoretical Considerations

When molecular self-assembly is used to design and realize nanostructures, apart from the mobility of the constituents on the surface, also a thermodynamic minimum is required for a gas of mobile molecules on the surface to condense into a self-assembled arrangement [14]. Self-assembly is driven by bonds like metal-ligand coordinations, hydrogen bonds or van der Waals interactions, all of which are rather weak compared to covalent bonds. Therefore, the interplay between enthalpy and entropy is an important factor in the formation of self-assembled nanostructures. The condensation into energetically favorable structures, therefore, sets in only at specific conditions. In most general terms these are given by the temperature of the surface and the respective amounts of provided constituents and their energetics. So when either of these parameters are varied to lie outside of the thermodynamic region of favorable assembly conditions, no structures with long range order can be achieved.

Further the choice of molecular constituents is crucial. Firstly, the desired type of lateral bond must be evaluated before synthesis. The actual bonding is steered by the choice of adequate functional units that are realized during synthesis. This is the first construction principle to achieve the desired nanoarchitecture. Secondly, the choice of molecular backbone, to which functional groups are attached, codetermines the possible geometries. In combination with the surface periodicity the constituents are deposited onto, different networks can be achieved via adjusting the molecule geometry. The last parameter to consider is the rigidity of the entire molecule as it also limits the possible arrangements. When molecules have little to no degrees of freedom in terms of adapting to the surface morphology, then long range order is only achieved when the arrangements find a commensurate adsorption pattern. Otherwise, energetically favorable adsorption sites, which are typically boundary conditions for the network formation, cannot be satisfied. As molecules with rotatable or flexible bonds and therefore many degrees of freedom can adjust to the surface

registry, lateral interactions between ligands can also be satisfied more easily. However, due to their high adaptability, the arrangements tend towards lower quality in terms of long range order and commensurability.

Chapter 3

Scanning Tunneling Microscopy

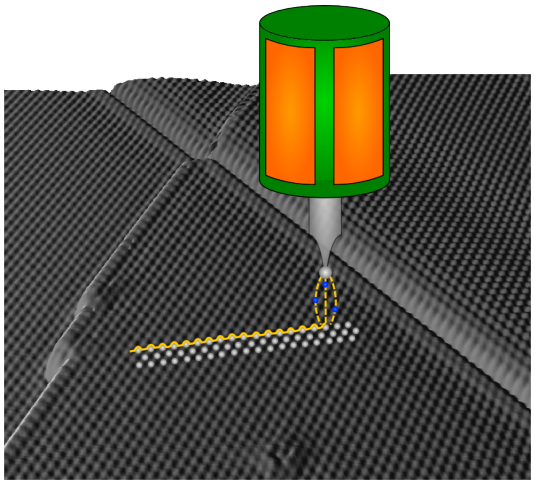

In this chapter the functioning of a scanning tunneling microscope is illustrated. Therefore, the basic operation principles and modes are discussed as well as their limitations imposed by instrumentation. The setup used in the experiments presented in subsequent chapters, a home-built [48] Besocke Beetle-Type STM [49, 50], operated at liquid He^4 temperature, is presented first. Afterwards, a second setup that was built up over the previous two years, featuring a novel Joule Thompson (JT) cooling stage, is introduced. The JT setup enables STM and STS measurements at ~1 K. To achieve high stability, a Pan-style scanner unit [51, 52] is used to position and scan the STM tip. First test and performance measurements are presented at the end of this chapter.

3.1 Operation Principles

3.1.1 Scanning the STM Tip

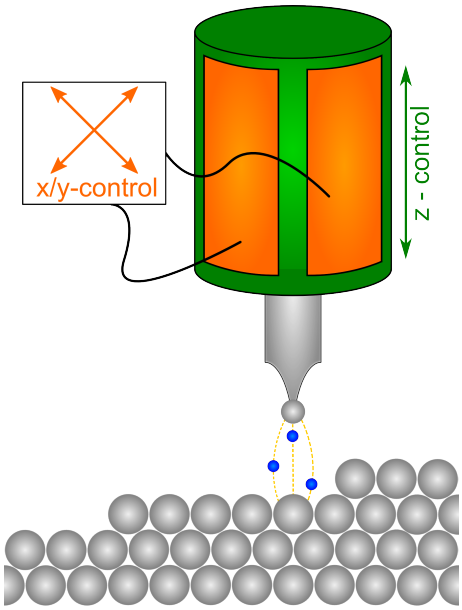

Figure 3.1.1: The STM tip is positioned and controlled utilizing a piezoelectric scanner, here a single-tube. By applying voltages to several different electrodes, the tube is deflected in the $x-$ and $y-$direction to scan the surface, while by contraction and extension the distance between tip and sample is controlled along the $z-$axis.

Since the tunneling junction enables the local probing of the tip-sample separation with high lateral sensitivity and accuracy, it is necessary to control the exact position of the tip apex in three dimensions with precision matching the sensitivity of the junction. Therefore, piezoelectric ceramics are utilized to control the tip movement in respect to the surface. Several concepts for the tip-sample approach have been demonstrated, the two most prominent designs thereby being the Besocke Beetle-Type STM [49, 50] and the Pan-Style STM [51]. In both cases it is possible to control the tip position after the coarse approach via piezoelectric deflection with precision well below interatomic distance. Thus, step sizes for individual data points

with subatomic resolution are achieved. Furthermore, high stability for the tip-sample separation and lateral position ($\lesssim$ 0.01 Å/h) are requirements for long time measurements, which can be achieved in both designs via sufficiently long settling times after coarse motion.

In Figure 3.1.1, a schematic for a single-tube scanner is shown, to illustrate the operation principle. In the Pan-design, a piezoelectric scanner tube is approached towards the surface by a slip-and-stick stepper motor controlling the coarse motion for the approach. Once the surface is reached, applying voltages to several electrodes on the tube leads to a deflection in $x-$, $y-$ and $z-$direction allowing for a highly sensitive scan of the surface.

For topography, two scanning modes can be used, the constant current and constant height mode, see Figure 3.1.2.

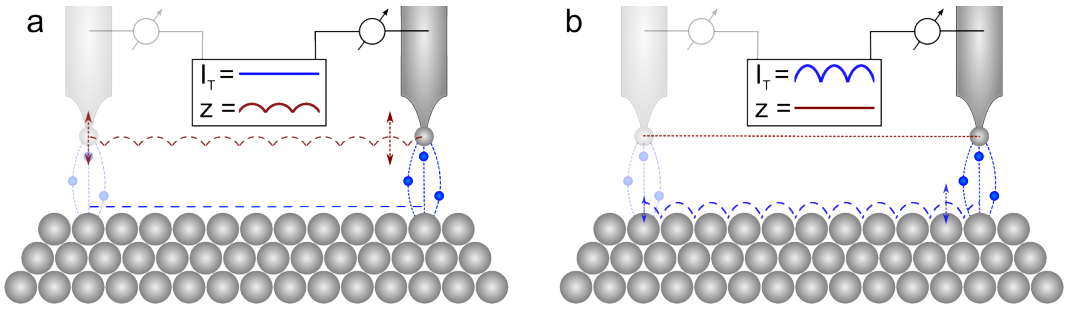

Figure 3.1.2: Operation modes in scanning tunneling microscopy: (a) Constant Current mode in which the tunneling current is kept constant by an electronic feedback loop and the extension and retraction of the tip is recorded. (b) Constant Height mode, here the height of the tip is kept constant and the change in tunneling current is recorded.

In constant current mode a PID-controlled feedback loop is used to maintain the tunneling current at a set value. The actual data recorded while scanning the surface is the extension and contraction of the scanner tube in the $z-$direction corresponding to each pixel, which in turn gives an accurate height profile in x and y for the investigated scan area. When the feedback loop response is slower than the scanning time or a constant tip-sample separation is desired, the PID control may be turned off after the tip was stabilized at a set value for the tunneling current. In constant height

mode, the resulting change in tunneling current during the tip motion reflects the change in height or LDOS of the underlying surface. However, this requires rather flat scan areas which are not tilted with respect to the scanning plane. Otherwise, the tip-sample separation is no longer constant and the tip might touch the surface.

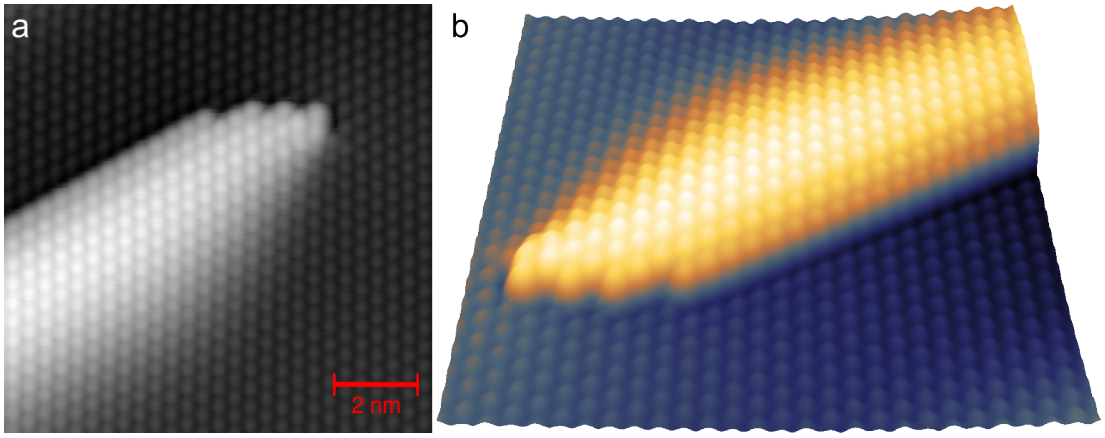

Figure 3.1.3: (a) Atomically resolved Bi(111) surface along with (b) 3D representation acquired in constant current mode ($V_b = 0.1$ V, $I_T = 0.1$ nA). The observed subsurface defect, a screw dislocation, is resolved with atomic precision, demonstrating the high lateral and vertical resolution of the STM.

To satisfy the needs for high stability and low mechanical noise in highly sensitive topographic and spectroscopic measurements, low temperatures are typically a prerequisite. At low temperatures higher mechanical stability due to reduced atomic motion and also lower thermal noise can be achieved. Further, as demonstrated earlier (see Figure 2.2.2), for high resolution spectroscopy measurements low temperatures are advantageous, since the spectroscopic resolution is directly proportional to temperature due to reduced thermal broadening.

3.1.2 Scanning Tunneling Spectroscopy

For the investigation of the LDOS it is necessary to record the change in tunneling current while ramping the sample bias. By numerically deriving

recorded I/V measurements it is possible to gain the desired information on the LDOS. However, since numerically deriving I/V curves yields pronounced mathematical artifacts, it is beneficial to use lock-in technology.

With the lock-in technique it is possible to directly measure the differential conductance signal. In practice, the sample bias U_B is modulated with a *sine*-wave at high frequency (typically between 1 and 50 kHz). The tunneling current I_T is then passed into an AC amplifier of the lock-in amplifier. The signal (I_T) is phase-locked at a difference of 90° to the phase of the reference signal (U_B). Together with a low-pass filter which also acts as an exponential integrator, white noise is integrated to zero and only the relevant phase-locked signal is recorded. Thereby, the differential conductance dI/dV is measured and the LDOS can be investigated with subatomic lateral precision. By increasing the bias modulation, also higher differential conductance signals are measured. However, at increased modulation amplitude, energy resolution is reduced due to the induced broadening. Since the assumption in Equation (2.1.15) is only valid for a fixed probe position, the feedback loop for z-control is turned off when single spectra are taken. Otherwise, the cutoff frequency of several kHz of the feedback loop limits the spectroscopic resolution and further the recorded spectrum is convoluted with the movement of the STM tip. The same holds true, when differential conductance maps are acquired simultaneously with constant current topography maps due to variable tip-sample separation.

3.2 Beetle-Type LT-STM

The STM used in the experiments presented in the following chapters was originally constructed and built by Sylvain Clair [48], inspired by the popular STM design by Gerhard Meyer [53] that has also been commercialized by CreaTec [54]. The setup enables measurements at temperatures below 10 K via liquid helium cooling as well as high temperatures up to 400 K via heating. The instrument is built into an ultra-high vacuum (UHV) system with an in situ sample preparation chamber attached to the cryostat system. Figure 3.2.1 depicts the system, with its essential parts and components, for further details consult [48].

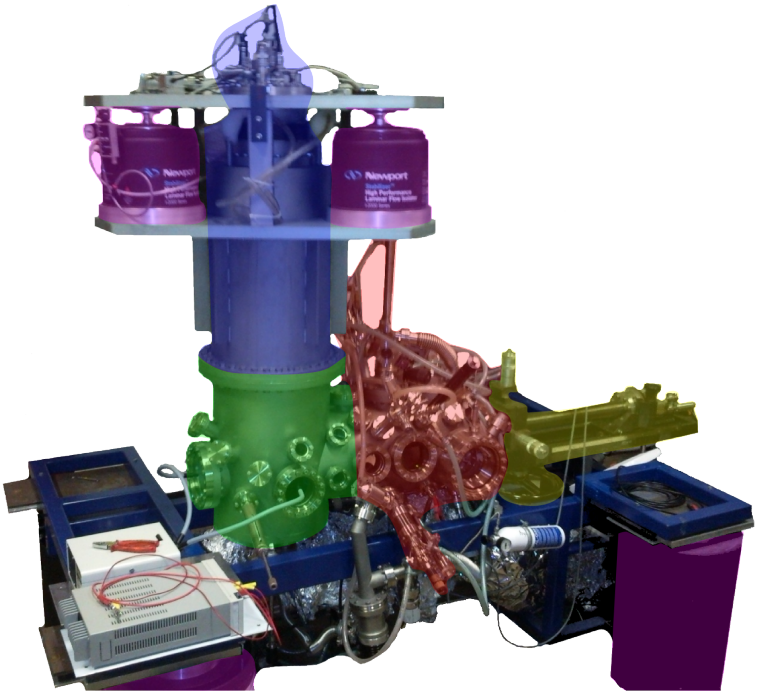

Figure 3.2.1: Photograph of the LT-STM setup. Parts of the UHV system: cryostat (blue), STM chamber (green), preparation chamber (red), sample manipulator (yellow), vibration isolation system (magenta). Underneath the STM chamber and the preparation chamber parts of the pumping system are visible.

3.2.1 UHV System and Sample Preparation

The scanning tunneling microscope as well as all the sample preparation and storage facilities are housed in an ultra-high vacuum (UHV) system with a base pressure $<10^{-10}$ mbar. The ultra-low pressure is achieved by pumping the system with a turbo molecular pump for which the pre-vacuum is established with a turbo molecular drag pump and a reciprocating piston pump. During measurements all mechanical pumping is stopped and the vacuum is maintained by two ion getter pumps, respectively attached to the preparation and the STM chamber, which are separated by a gate valve.

For sample preparation, typical surface preparation and material evaporation components are attached to the preparation chamber. To produce atomically flat noble metal surfaces, single crystals are in a first step cleaned via an Ar^+ ion beam from a sputter gun with a flux of $\sim 7 \frac{\mu A}{cm^2}$. To render the surface atomically flat, the sample is then heated up by an electron-beam heater, which is built into the sample grabber on the manipulator arm, to appropriate temperatures (e.g. ∼470° C for Ag(111)). After the surface has been prepared, molecules can be deposited from a two-cell organic molecular beam evaporator onto the sample, which is held at a controlled temperature. In a similar fashion, single metal atoms can be evaporated from an electron-beam evaporator, in which heating does not occur resistively but by a focused electron-beam. To transfer samples and tips into and out of the vacuum system, a load-lock that can be pumped down to $<10^{-8}$ mbar is attached to the preparation chamber. Via the load-lock, transfer is possible without breaking the vacuum. After preparation, the samples are first precooled using liquid nitrogen, before they are transferred into the LT-STM for measurements.

3.2.2 Cryostat

Figure 3.2.2 shows a schematic of the liquid helium cryostat setup. Thermal isolation of the helium bath is achieved by several features. First, the UHV in the system isolates the cryostat setup from ambient conditions.

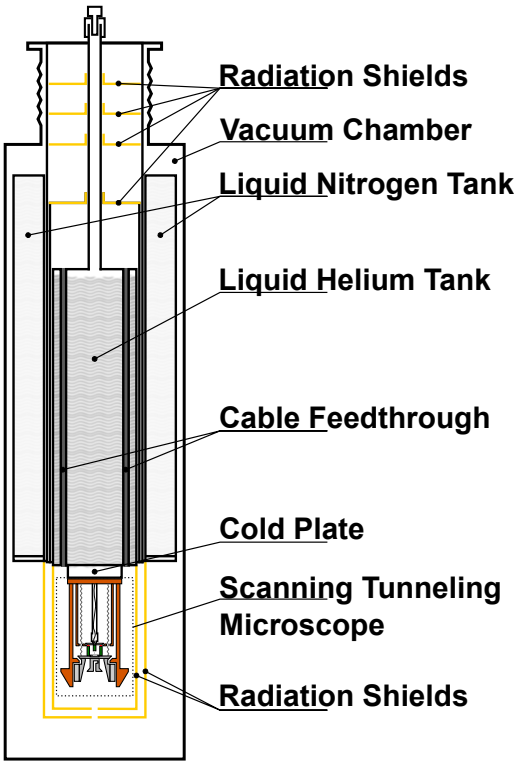

Figure 3.2.2: Schematic of the LT-STM and cryostat. All essential parts are labeled.

A liquid-nitrogen cryo-shield surrounding the helium bath in the center further reduces thermal radiation in combination with several radiation shields over the helium tank. All components are made from stainless steel due its low thermal conductivity.

The STM scanner unit is attached to the cold plate on the bottom of the helium tank and is further surrounded by a set of radiation shields, one at liquid nitrogen and another at liquid helium temperature, which can be rotated to open windows for sample transfer, pulling down the STM head, and optical access. All radiation shields are coated with gold to ensure high reflectivity and prevent oxidization.

All wiring required for measuring temperatures, operating the piezoelectronics and detecting the tunneling current are fed into and through the cryostat, where good thermalization of all wires is accomplished by attaching them to the different cooling stages of the cryostat.

3.2.3 STM Head

The beetle-type scanner unit is situated on the bottom of the helium tanks cold plate. To ensure good thermal contact, the outer body, mounting and base plate are made of copper. A photograph of the scanner unit after the outer copper body has been removed is shown in combination with a schematic illustrating the main parts in Figure 3.2.3.

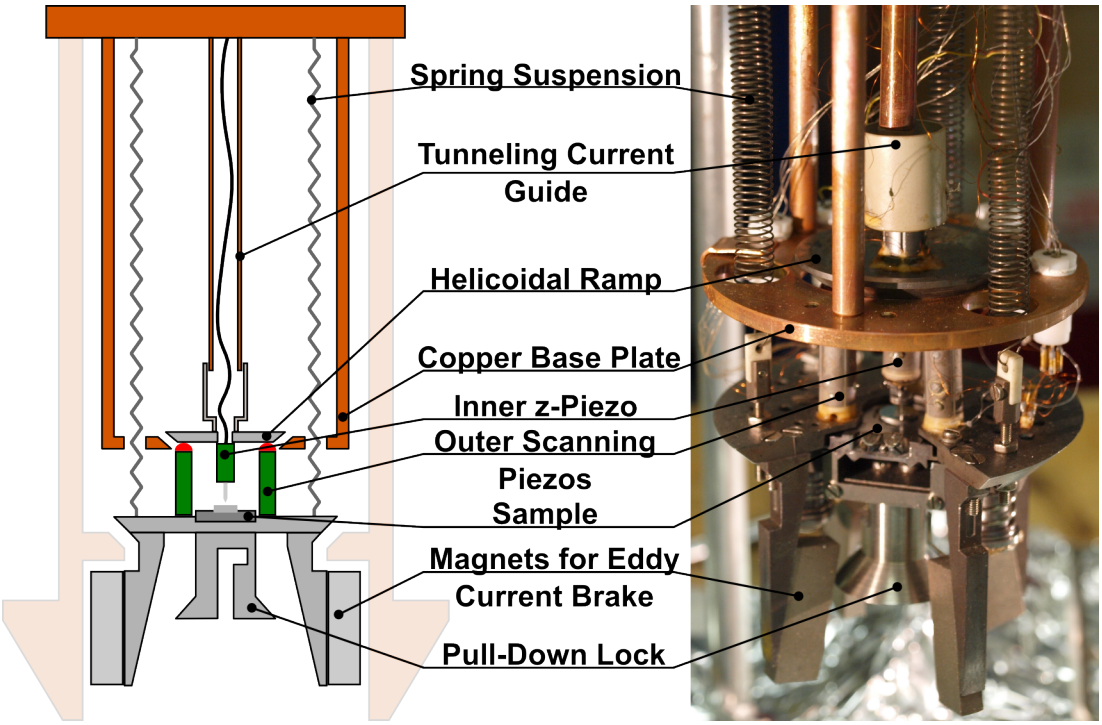

Figure 3.2.3: Schematic and photograph of the beetle type LT-STM scanner unit. All essential parts are labeled.

Since STM is highly sensitive to mechanical noise, the scanner is suspended on springs. In combination with spring suspension, the bottom plate, on which the sample and piezo scanners are mounted, is equipped with CoSm magnets which are used as eddy current brakes (the U-shaped counterpieces attached to the outer body are not pictured). After the sample is transferred into the STM and cooled down to operation temperature, the tip is approached, using the outer piezoceramics. The tip is attached to

a helicoidal ramp, which is segmented into three angled parts on the bottom. Each of the segments rests on a piezo scanner tube with a sapphire hemisphere attached to the top. By deflecting the piezoceramics in a clockwise or counterclockwise fashion, the ramp can be rotated and thereby the coarse approach is controlled. When the piezoceramics are operated in the $x-$ or $y-$direction, the tip can be moved coarsely across the sample area. When the coarse approached is finished, the tip-sample separation is controlled by the scanner tube onto which the tip is attached and held by a CoSm magnet. The inner tube can be used to only control the tip-sample separation, while the tip is scanned by deflecting the outer piezo tubes (standard operation). Alternatively, the scanning of the STM tip can be facilitated by deflecting the scanner tube in x and y. Hereby the calibration and scan range of both operation modes is naturally different. In standard operation the scan direction relative to the sample surface hardly changes.

To transfer samples into or out of the STM, the radiation shields are opened and a bayonet arm is locked to the bottom of the STM via the pull-down lock. When the STM is pulled down, the helicoidal ramp rests on the upper part of the copper base plate, whereas the bottom plate is pressed onto the outer body. Thereby, all positions are mechanically fixed and the sample-grabber can be introduced with the manipulator arm. To transfer tips to and from the STM, a tip-exchange tool can be picked up by the sample grabber. After the fork is positioned around the tip-holder, the manipulator is moved down, until the tip rests on the exchange tool and is then transferred to the preparation chamber.

3.3 Joule Thomson LT-STM

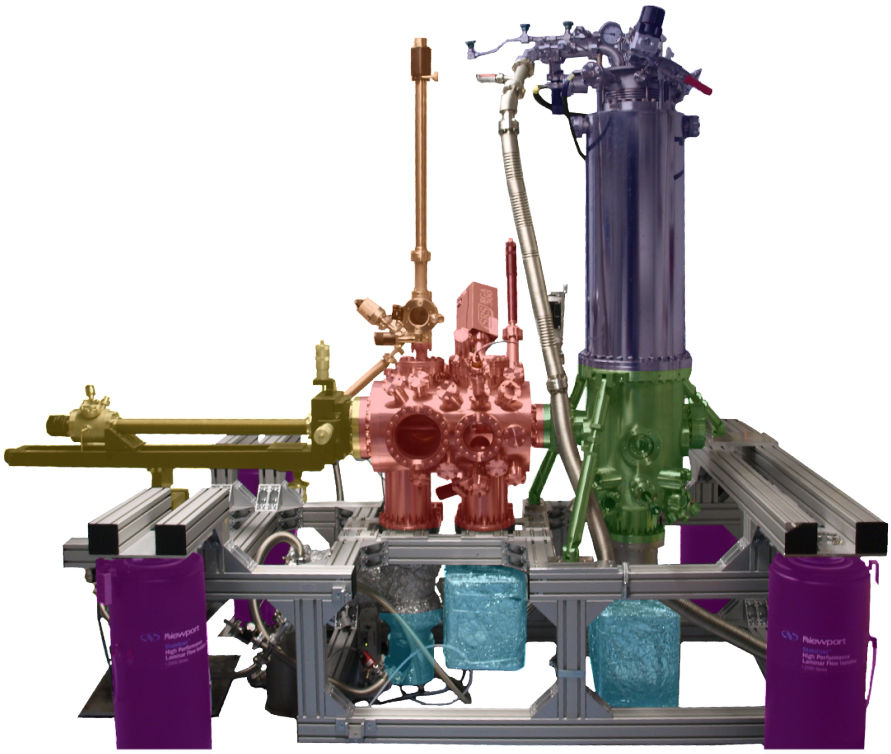

Figure 3.3.1: Photograph of the JT STM Setup. Essential parts: Cryostat (blue), recipient chamber (green), preparation chamber (red), load lock (orange), manipulator arm (yellow), pumping system (turquoise), vibration isolation system (magenta).

Over the course of this PhD project, a novel low-temperature STM setup was planned and realized. The cryogenic system of the STM features a Joule-Thompson expansion cooler, which allows the scanner unit to be cooled down to a base temperature of ∼1 K. This further reduction in temperature compared to conventional, low-temperature setups utilizing a liquid helium bath cryostat yields many advantages. For spectroscopy measurements and first and foremost inelastic tunneling spectroscopy measurements, the resolution R is greatly limited by the experiment temperature, since $R \propto 5.4 \cdot k_B T$ [55, 56] (whereby the sensitivity in spectroscopy experiments is increased by a factor of ∼4 when the temperature is reduced from liquid

helium temperature to 1 K.).

To exploit these advantages, the STM head was designed towards maximum mechanical stability. The design of the cryostat and STM was first realized in the group of Prof. W. Wulfhekel at the Karlsruhe Institute of Technology [57] and shortly afterwards commercialized by SPECS GmbH in Berlin [52]. The presented setup is the first commercialized prototype system. A photograph displaying the major components is shown in Figure 3.3.1.

3.3.1 Peripherals and UHV System

The vacuum and cryogenic system is mounted on a custom designed frame built from aluminum profiles purchased from *ITEM*. The individual profiles were further filled with sand in the bottom part of the frame to move the center of mass of the entire system towards the bottom, and two-component PU foam for the upper profiles. Both measures do not only increase weight, but also increase rigidity and eliminate acoustic coupling into the otherwise hollow profiles. The frame is designed to allow mounting and removal of the cryostat via a hoist that is bolted onto the laboratory ceiling. Therefore, it was important to remain within the restrictions imposed by the room height. To increase the stiffness and rigidity of the frame in order to eliminate mechanical noise, especially for the parts surrounding the manipulator arm, all parts were connected using linear connectors and an aluminum plate to further reinforce the construction was introduced. In Figure 3.3.2 a rendering of the construction drawings of the system during the final planning stage is displayed.

The vacuum chamber consists of two main parts: the preparation chamber and the recipient chamber (see Figures 3.3.1 and 3.3.2), both of which have been manufactured by *VaB*. These two parts are separated by a gate valve which allows shutting off the STM side of the system during sample preparation to avoid contamination. Especially after the cryostat is cooled down, contamination is problematic due to very effective cryopumping. To generate vacuum in the UHV system, a magnetically suspended 300 l/s

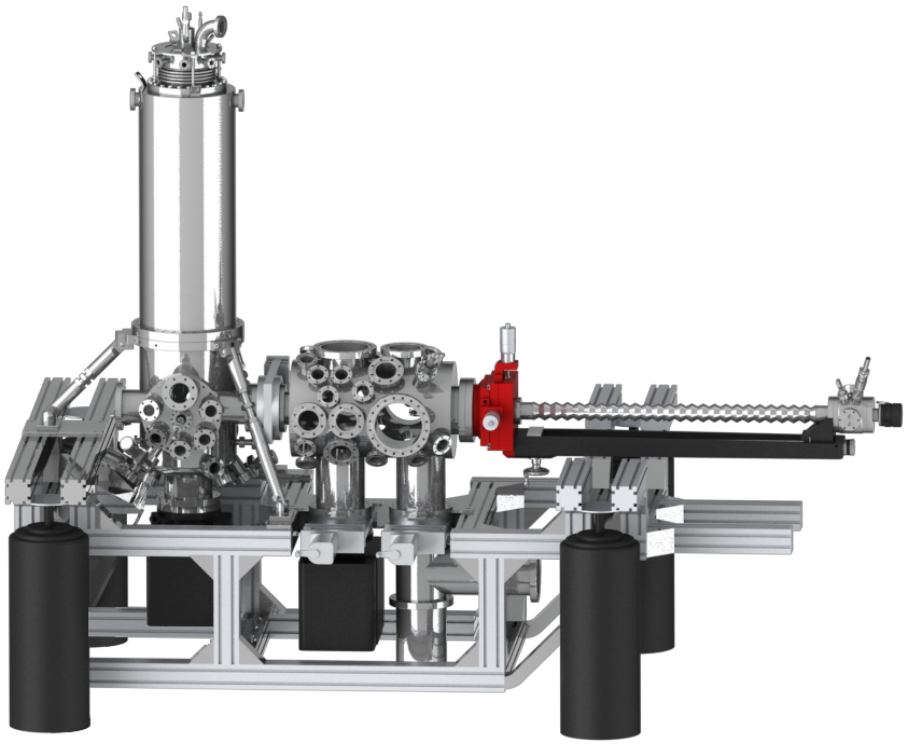

Figure 3.3.2: Rendering of the JT-STM system during the final planing stage. Some parts are only displayed as place holders or missing.

turbo molecular pump (TMP) is attached to the preparation chamber. Between the preparation chamber and the pump, a gate valve situated directly on the chamber and a small T-shaped vacuum chamber housing a titanium sublimation panel (TSP) and cryoshield outside the pumping cross-section are introduced. The pneumatically actuated gate valve is configured in a manner that in case of a power failure, the UHV system is closed. The pre-vacuum required to operate the main TMP is generated by a series of pumps, namely a membrane pump (ultimate pressure <2 mbar) and a drag TMP (ultimate pressure $<10^{-8}$ mbar). Several valves are introduced into the pumping line to avoid contamination when the pumps are stopped during measurements to reduce mechanical noise. A separate valve to vent the system from a liquid nitrogen reservoir is further available. To maintain vacuum when mechanical pumping is stopped and also when the gate valve between preparation and recipient chamber is shut, two ion-getter pumps

(IGP) are operated. One is positioned below the preparation chamber and can be closed off during sample preparation via a gate valve to maintain the pumping capabilities of the getter mesh. The IGP on the STM part of the system (below the recipient chamber) is continuously operated once UHV conditions are reached.

3.3.2 Preparation and Recipient Chamber

The two main vacuum chambers of the system are the preparation chamber and the recipient chamber. All instrumentation required for in situ sample preparation and testing are attached to the preparation chamber, whereas the recipient chamber houses the experimental setup. The required instrumentation and therefore the necessary design considerations for each chamber will be presented shortly in the following.

3.3.2.1 Preparation Chamber

The necessary instrumentation for sample preparation are an Ion Sputter Gun (ISG), an (Organic) Molecular Beam Epitaxy (OMBE) source, a Low Energy Electron Diffractometer (LEED), a Residual Gas Analyzer (RGA), a Sample Cleaving Station, a Load Lock (LL), and a Sample Holder on a manipulator arm. In Figure 3.3.3 the positioning of the instrumentation on the chamber is shown.

Ion Sputter Gun: Ionized argon from a leak valve is accelerated with high voltage, typically 1 kV, towards the sample surface. By the ion bombardment the top most layers and adsorbates are removed from the surface.

(Organic) Molecular Beam Epitaxy source: The home-built evaporation source features four BN crucibles in which molecules are stored. The crucibles are heated by a Pt filament that is wound around each of them. The resistance of the Pt wire is characteristic and thereby allows direct measurement and control of the filament temperature. Instead of crucibles, filaments can be mounted, which can heat metal sources to deposit metal

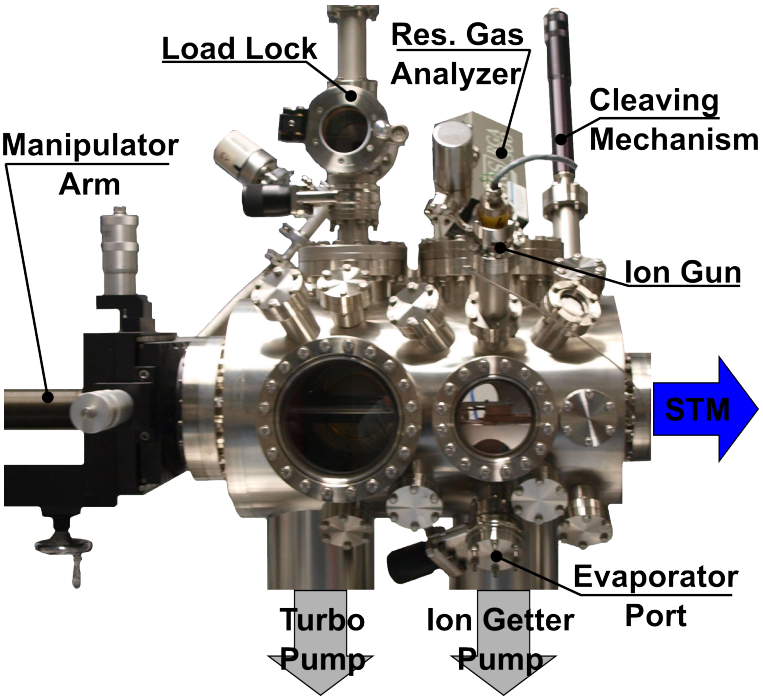

Figure 3.3.3: Photography of the Preparation Chamber. The LEED attached to the chamber resides on the opposite side and is therefore not visible.

atoms via thermal sublimation. The evaporator is connected to the chamber through a valve, therefore evaporation material can be changed without breaking the vacuum in the system. Vacuum in the evaporator volume is reestablished by pumping with a turbomolecular pumping station through a valve, before the gate valve to the chamber is opened again.

Low-Energy Electron Diffractometer: The LEED with rigid luminescent screen position enables the analysis of surface crystallography and ordered structures. Crystal surfaces can be checked to ensure proper preparation prior to molecule deposition. The ordering of adsorbates on the surface can also be studied in this fashion. The instrument is mounted in a length-optimized flange so samples on the manipulator arm can be positioned directly in front of the screen at the ideal distance and position.

Residual Gas Analyzer: The RGA is a mass spectrometer based on a quadrupole design. This enables the analysis of the residual gas in the vacuum chamber. It is mounted opposite to the OMBE, so the deposition rate of molecular species can be estimated and checked. Further it is used to control the purity of gases and can be used to check for leaks on the

vacuum system via He^4 detection.

Sample Cleaving Station: In order to produce defined surfaces by cleaving, samples typically have to be cooled and subsequently the top layers can be ablated along specific cleaving planes. To realize this, samples are cut on their edge to define a cleaving point and then a ceramic rod is fixed with epoxy resin. This rod is then pressed against an edge of the cleaving station, where the ablated material can be deposited into a reservoir attached below. The station is mounted on a linear feedthrough in order not to block movement of the manipulator arm when it is not in use.

Load Lock: Samples and tips can be transferred in and out of the vacuum system via the LL. To accomplish this without contaminating the vacuum, a small vacuum chamber is mounted on top of the preparation chamber which can be pumped with a turbomolecular pumping station through a valve before the transfer. To transfer samples or tips, the manipulator arm is positioned below the load lock and rotated appropriately. Samples are grabbed with a bayonet locking mechanism which is attached to a magnetically actuated linear manipulator which can easily be moved vertically.

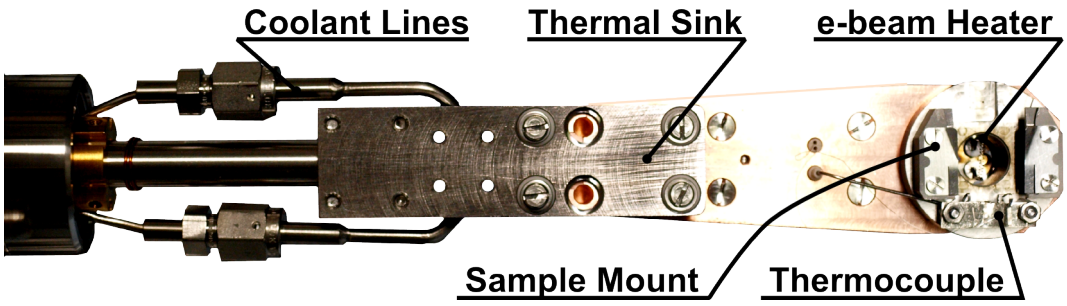

Figure 3.3.4: Photography of the Manipulator Head.

Manipulator Head The Manipulator Head (see Figure 3.3.4) is mounted on a manipulator that allows translational (± 25 mm in the x-y-plane and 750 mm along the chamber axis) and rotational (360°) movement. Thereby samples can be positioned inside the vacuum chamber at defined positions for the individual preparation steps and transfer procedures. Further the Manipulator Head is equipped with an e-beam source below the sample

plane to heat samples from the backside either through resistively heating the emission filament or by applying up to 1.5 kV to the filament and therefore accelerating electrons onto the backside of the sample. The sample temperature is measured with a k-type thermocouple that is pressed against the sample holder. Further, the manipulator arm and head can be cooled with liquid nitrogen down to ∼150 K.

3.3.2.2 Recipient Chamber

The Recipient Chamber is attached to the Preparation Chamber and can be closed off with a gate valve. The construction is further stabilized and suspended by three length adjustable support beams that are directly bolted onto the frame. After preparation, samples are transferred into the recipient chamber with the manipulator arm. Samples are transferred into the STM with a magnetically mounted wobble stick that is attached to a cluster flange along with several view-ports. To grab the sample plate, the wobble stick is equipped with a mechanically actuated pincer grip. Further, the wobble stick is used to open, close and operate different functionalities implemented into the radiation shields. Five sample storage stages are furthermore attached to the outer radiation shield in which samples and tips can be stored (accessible via the wobble stick).

Opposite to the cluster flange, a second wobble stick with lateral and rotary freedom of motion is mounted, see Figure 3.3.5. With the latter other functionalities of the radiation shields are accessed, with the operation of the thermal short between the liquid helium radiation shield and the JT shield being the most important here. Due to thorough thermal isolation, this shortcut is crucial for cooling down the JT-stage and STM to liquid helium temperatures, before cooling to lower temperatures is possible. Facing the sample, several ports, which can be equipped with evaporators or provide optical access, are positioned on the bottom of the chamber. These can be utilized to deposit material onto the sample at cryogenic temperatures. This is a necessary technique, when single, isolated atoms or molecules on surfaces are investigated, since at ambient temperatures adsorbate motion

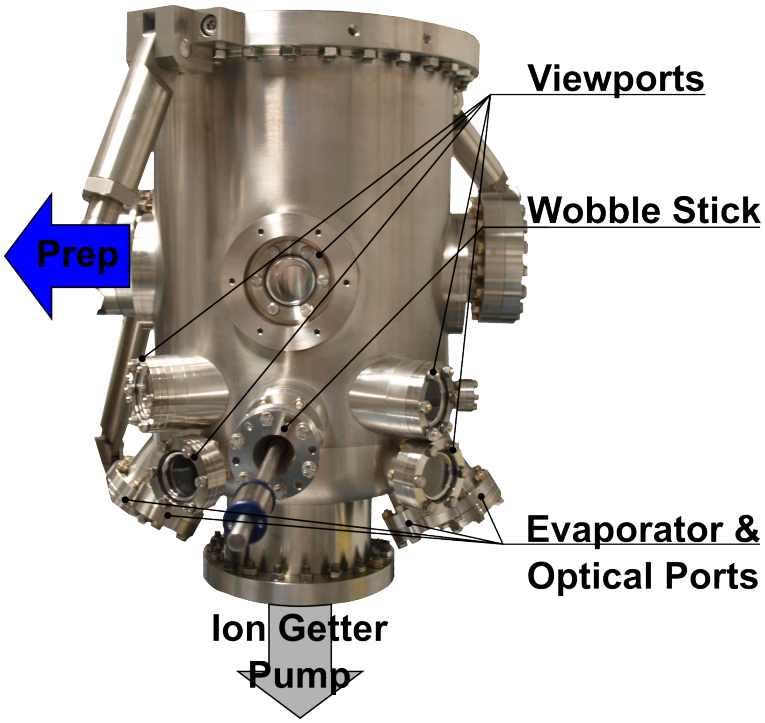

Figure 3.3.5: Backside view of the Recipient Chamber. The Wobble Stick is used to actuate the thermal short between the liquid helium radiation shield and the JT-stage of the cryostat.

leads to cluster formation or self-assembled structures, which is not the case at cryogenic temperatures. The optical access allows the coupling of light from a laser source into the system, which could later be implemented to realize optical experiments.

3.3.3 Cryostat

The basic design of the cryostat differs very little from the one used in the Beetle-Type-STM (cf. Section 3.2.2). For cryogenic temperatures down to liquid helium temperature, again a bath cryostat, surrounded by a liquid nitrogen vessel is used.

The main difference, however, is that temperatures down to ∼1 K are possible. To make experimental conditions below liquid helium temperature accessible, the cryostat used in this setup features a Joule-Thomson expansion stage. To reach conditions under which the Joule-Thomson process sets in, highly pure helium gas from a pressure reservoir is discharged through a very long, very thin capillary, that is thermalized first to liquid nitrogen and

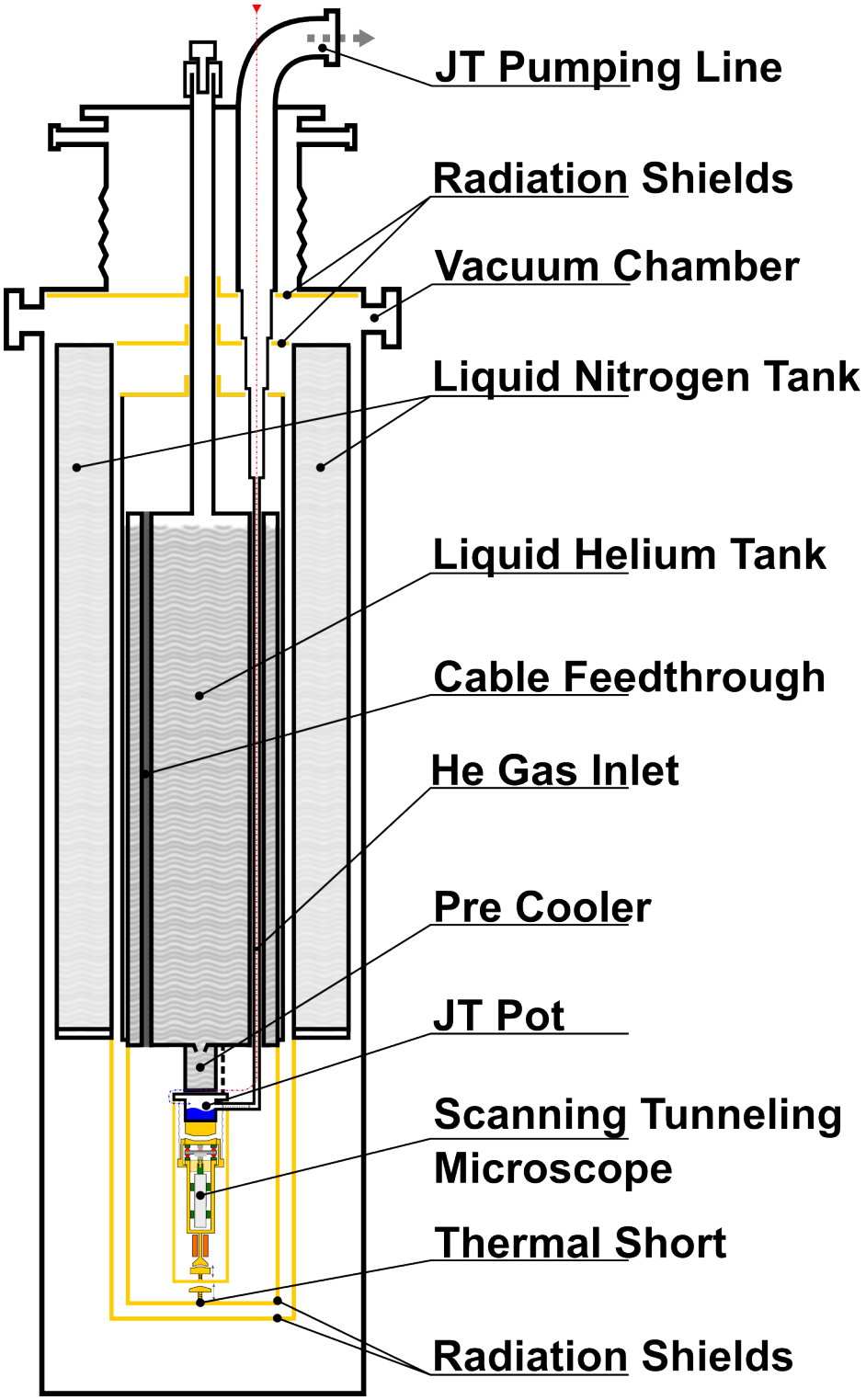

Figure 3.3.6: Schematic of the JT-STM and cryostat. All essential parts are labeled.

afterwards to liquid helium temperature for pre-cooling, into the JT-pot at the bottom of the cryostat. On the other hand the JT-pot is evacuated by a rotary vane pump. Therefore, when gas is passed through the narrow capillary, it reaches the pseudo-vacuum where upon condensation it is cooled down further. The temperature of both the JT-pot and the scanner unit are monitored by two Cernox temperature sensors, directly attached to them. With this technique it was possible to reach temperatures of ∼1.13 K with continuous He gas flow.

The high purity of the He gas is a necessity, otherwise contaminants will freeze-shut the capillary. The JT-pot is thermally isolated from the liquid helium reservoir; for pre-cooling a thermal short between the radiation shield attached to the helium cryostat and the one surrounding the JT-stage and microscope is established which is released once Joule-Thomson expansion sets in.

3.3.4 STM Head

The STM head is similarly to the one discussed earlier, suspended on springs for vibration isolation. To fixate the head for sample transfer, it can be pressed up against the JT-pot by a mechanical actuator connected to the radiation shields that is operated via the wobble-stick. The body of the head is designed to suppress mechanical excitations, since no low-frequency resonant modes are accessible. To ensure a perfect vertical orientation of the body, copper weights can be attached and removed to the bottom to align the main axis of the body when it is hanging freely.

The scanner unit (see Figure 3.3.7) is based on a Pan-style approach system. A Pan-motor is used to approach the tip from the bottom towards the sample. The motor is a piezoelectric slip-stick stepper, where a sapphire prism is held from three sides by shear piezo stacks. When the shear stacks are slowly deflected in one direction and afterwards rapidly released into their equilibrium position by a saw-tooth voltage pulse, the inertia of mass will lead to the sapphire prism remaining in the deflected position. By continuously applying saw-tooth pulses, the prism is thereby moved up or

down, depending on the polarization used, at variable step size, depending on the pulse amplitude, and speed, depending on the pulse frequency.

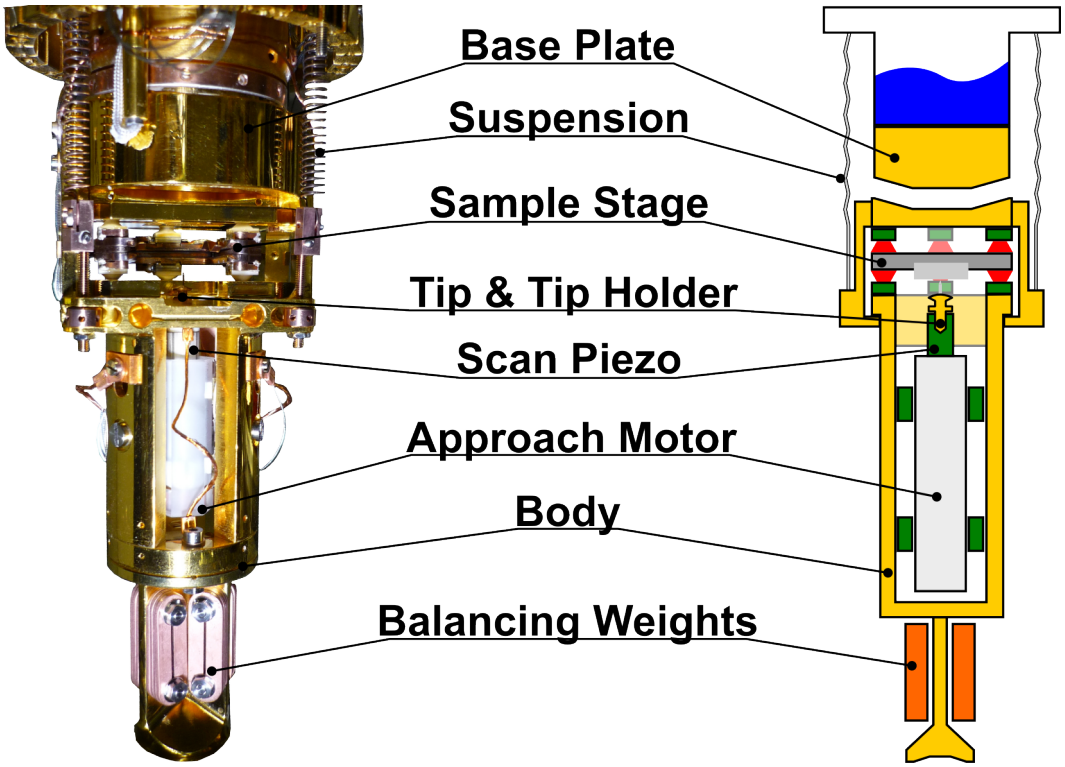

Figure 3.3.7: Photograph and schematic of the Pan-type JT-STM scanner unit. All essential parts are labeled.

The piezo tube is attached to the top of the sapphire prism and is, as already described earlier, used to scan the tip across the sample surface once the coarse approach has finished. The tip is mounted in a tip-holder that is positioned in the scanner tube. To ensure proper thermalization of the STM tip, since in spectroscopy experiments the temperature of the tip is the decisive factor for thermal broadening and resolution, a copper braid connects the body and the scanner tube. Otherwise, the tip would not be cooled due to the low thermal conductance of the the piezo ceramics holding the prism in place.

The coarse position of the sample can be changed along the $x-$axis of the horizontal plane. The sample stage, in which the sample is positioned,

is therefore clamped, similar to the approach motor, by piezoelectric stacks, which allows moving the sample stage along the $x-$axis. Similar to the tip, the sample stage is also thermalized by a copper braid to ensure proper thermal contact.

It is furthermore important to change tips in situ. For tip exchange, a specially designed sample plate, into which the tip holder can be anchored, is placed in the sample stage. After the tip holder is moved up sufficiently, the tip exchange tool is moved so that the tip is hooked. By moving the Pan-motor down again, the tip holder then remains anchored in the exchange tool and thereby pulled out of the scanner tube.

3.3.5 Performance and Test Measurements

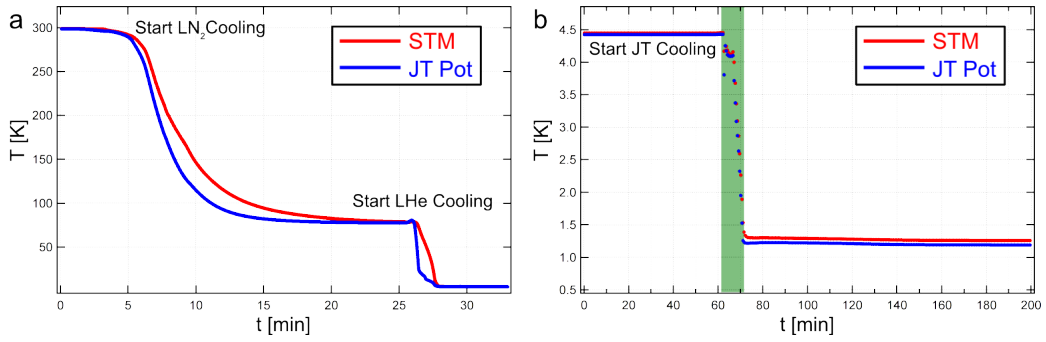

Figure 3.3.8: (a) Subsequent cooling down of the setup first by liquid nitrogen and afterwards by liquid helium. The entire procedure requires approximately 30 hours until stable base temperature is reached. (b) The STM is cooled down using the Joule Thomson cooling stage. To reach base temperature, the system must be cooled for approximately 10 minutes after JT-expansion has started.

After initial installation and bake-out, pressures in the 10^{-10} mbar regime were achieved in the vacuum system after the cryostat was cooled down to 4.5 K. Liquid helium and nitrogen hold times of ∼3 days in each of the vessels were reached. Two typical examples for cooling down the cryostat are shown in Figure 3.3.8. In Figure 3.3.8 (a) the cooling from room temperature to liquid helium temperature (including precooling with liquid nitrogen

over night in the helium cryostat) is shown. Thereafter, cooling down to the lowest temperature, after Joule Thomson expansion starts, is facilitated in approximately 10 minutes (Figure 3.3.8 (b)).

First test measurements showed a strong coupling of mechanical noise into the microscope. These could be eliminated by subsequently modifying the STM suspension. Exemplary noise power spectral density measurements are shown in the left portion of Figure 3.3.9. With JT-cooling enabled, the noise intensity slightly increases at ∼1.2 K (blue) in contrast to measurements at liquid helium temperature (poor STM tip in red, sharp STM tip in green). Scans revealing atomic resolution on Ag(111) with a lattice constant of 2.89 Å, both at ∼4.5 K and ∼1.2 K, are displayed in the right portion of Figure 3.3.9. The experimental data in both cases was not post processed, apart from flattening the images to remove changes in height induced by changes of the STM tip for the example shown for 1.2 K.

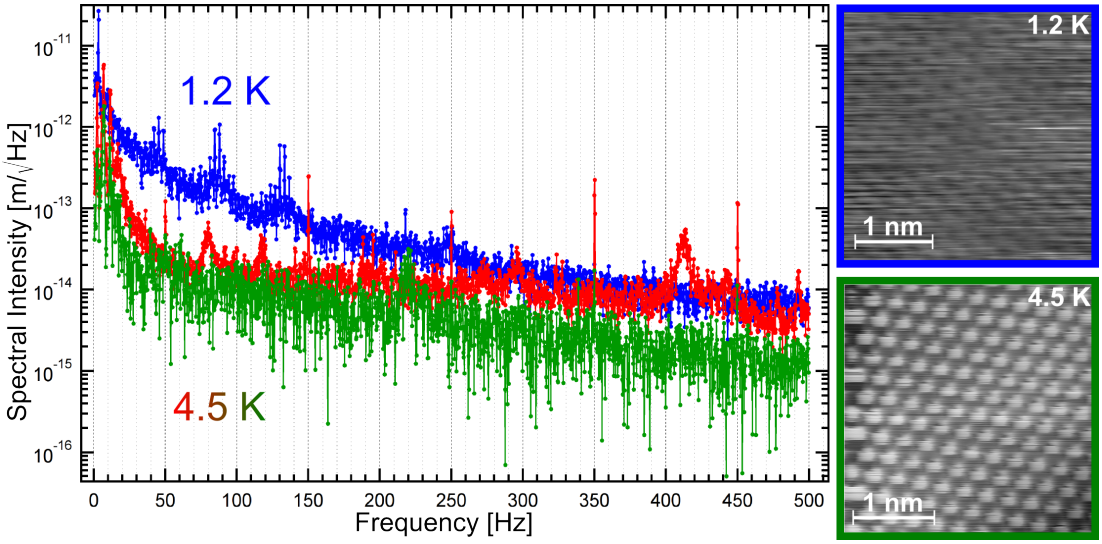

Figure 3.3.9: Examples of the JT-STM performance at 4.5 K and 1.2 K. The noise power spectra shown above were acquired at 4.5 K for red and green and 1.2 K for blue, respectively. The atomically resolved Ag(111) lattice at 4.5 K and 1.2 K is shown below.

Chapter 4

Positioning Single Co Atoms Using N,N’-Diphenyl Oxalic Amide Templates on Ag(111)

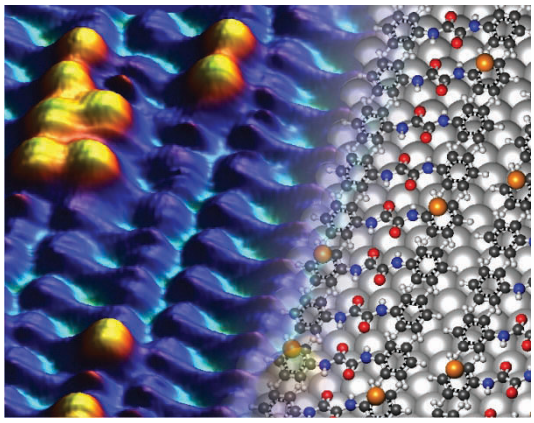

Low-dimensional structures on the nanoscale constructed from single magnetic atoms possess intriguing properties since the Magnetic Anisotropy Energy, which leads to an ordered alignment of the magnetization, strongly depends on the exact size, arrangement and dimensionality [58, 59, 60, 61, 62, 63, 64, 65]. Therefore, the possibility to construct such structures using N,N’-diphenyl oxalic amide molecules as fundamental building blocks has been investigated. In a first step, the self-assembly of these molecules was investigated on Ag(111). The templates formed were then exposed to atomic cobalt for which the phenyl rings of the molecules act as adsorption sites. Further, the temperature and coverage dependence of the monomeric distribution of Co atoms on the template was investigated thoroughly. Parts of this chapter were published in Reference [66]. Reprinted with permission. Copyright 2011 American Chemical Society.

4.1 Molecule Properties and Sample Preparation

The molecules utilized in the experiments are N,N'-diphenyl oxalic amide molecules (DOA), a structure model of the molecule is displayed in Figure 4.1.1. The molecular bricks feature two phenyl rings on the outside of the molecule, which are connected by an oxalic amide group in the center. The molecules have been synthesized according to Meyer and Seeliger [67]. The Ag(111) substrate was prepared by repeated Ar^+ bombardment of a Ag single crystal at an energy of 1 keV followed by annealing to 750 K for ∼10 min. The investigated molecular templates were formed by organic molecular beam epitaxy of DOA molecules from a quartz crucible, which was heated in a Knudsen cell held at ∼417 K onto the Ag substrate held at room temperature (297 K). Subsequently, Co was deposited from an electron beam evaporator unit, which was operated at a deposition rate of 0.0018 monolayers/second (a monolayer here corresponds to all phenyl rings of a full molecular layer being occupied by a single Co atom), with the substrate held at 110 K to 240 K. After preparation the samples were cooled down and investigated via LT-STM. The observed self-assembled molecular templates and their utilization to steer the adsorption of Co atoms will be discussed in the following.

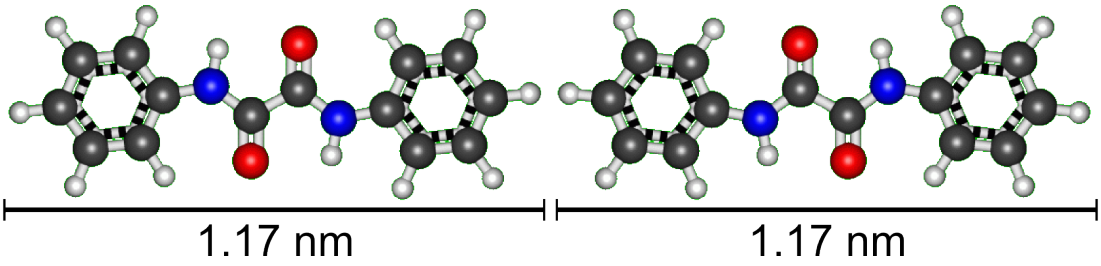

Figure 4.1.1: Structure model of N,N'-diphenyl oxalic amide (H white, C black, O red, N blue). The two phenyl rings on the outside of the molecule are connected by a thinner waist constituting an oxalic amide group. On the surface, the molecule is found in two enantiomers due to adsorption in either orientation on the surface.

4.2 Self-Assembly on Ag(111)

In a first step, the formation of supramolecular architectures formed via self-assembly of N,N'-diphenyl oxalic amide on Ag(111) was investigated. Previous investigations of the assemblies [68, 69] already clarified some of the formation mechanisms and assemblies. However, by illuminating the intermolecular interactions and influence of the substrate registry in a both experimental and extended theoretical investigation, a more precise understanding of the formation principles could be achieved. Therefore, the formation of molecular nanogratings in the sub-monolayer (sub-ML) regime and the dense packed monolayer (ML) assembly is discussed in the following.

4.2.1 Molecular Nanowires

For molecule coverages below one monolayer (ML), an arrangement of approximately equally spaced lines of molecules (appearing brighter than the substrate) is observed (see Figure 4.2.1 (a&b)), similar to supramolecular gratings reported in other experiments [70, 71, 72]. The exact origin of the equal spacing between the supramolecular chains is still not clear. Electrostatic repulsion of the molecular lines towards one another and the Ag(111) surface electron state leading to the periodic assembly have been proposed as formation mechanisms. In the experiments, six directions along which the chains are aligned are observed in total, only three appear in Figure 4.2.1 (a&b). These are closely related to the three high symmetry directions of hexagonal Ag(111) surface registry, indicated by a red star in Figure 4.2.1 (a&b). This finding points towards an assembly of the molecules commensurate with the surface periodicity, since the symmetry of the substrate is also reflected in the alignment of the gratings.

In a higher resolution scan (Figure 4.2.1 (c)), the substructure of the molecular gratings becomes more clear. Pairs of molecules forming fundamental units in the chains are encountered (yellow). The pairs are displaced with respect to adjacent pairs along the molecular line direction by ∼0.5 Å to

Figure 4.2.1: (a&b) Overview images of equally spaced molecular lines assembled on the Ag(111) surface. The three observed alignment directions are closely related to the high symmetry directions of the substrate along with two chiralities reflecting either enantiomer of the molecule observed (V_B = -1.0 V, I_T = 0.1 nA for both). (c) Higher resolution topographs reveal the formation mechanism within the chains. Single molecules are imaged as a dog-bone like protrusion. This appearance originates from the two broader phenyl rings at the outer ends connected by a thinner waist. Pairs of molecules, which are slightly displaced along the chain direction relative to adjacent pairs, form the individual lines. $\alpha \simeq 15°$ indicates the orientation of the nanowires relative to the substrate, whereas $\beta \simeq 55°$ is the orientation of the molecule backbones (V_B = -0.7 V, I_T = 0.09 nA). The orientation of the nanowire relative to the substrate in combination with the two enantiomeric configurations of the molecules leads to the expression of chirality. In this case *Right*, as indicated. (d) High resolution image with molecular models superimposed reveals the internal formation of the chains in detail. The arrangement of molecules forming pairs as a substructure of the nanowires is observed more clearly. This leads to $\gamma = \alpha + \beta \simeq 70°$ between the nanowire direction and the molecular backbone. The bonding mechanism within the pairs is driven by bonding between the functional groups, whereas the oxygen moieties coordinate towards the phenyl rings along the nanowires. The displacement of individual pairs rather than the formation of straight wires is attributed to adsorption commensurate with the surface registry (V_B = -0.3 V, I_T = 0.11 nA).

each other, leading to a staircase like outline of the chains. Due to the two enantiomers possible upon adsorption on the surface for the molecule, along with the three high symmetry directions of the substrates, two chiral assemblies for the chains are found for each high symmetry direction. Thereby, the *Left* and *Right* handedness of the molecule enantiomers leads to the total of six assembly directions found in the experiment, where one high symmetry direction is reflected by two nanograting directions with different chirality. As indicated in Figure 4.2.1 (c), the *Left* and *Right* handedness of the assembly is defined by the rotation of the line directions relative to the related high symmetry direction (in the presented case *Right*).

In respect to the substrate, the individual molecules align within the chains to enclose an angle of $\alpha \simeq 15°$ between the molecular backbone and the related high symmetry direction. On the other hand, the long axis of the molecule chains is rotated away from the same high symmetry direction by $\beta \simeq 55°$ (Figure 4.2.1 (c)). Therefore, the gratings do not follow exactly the high symmetry directions, but are rotated by $\sim 5°$ (Figure 4.2.1 (c)). With respect to the chain substructure, the alignment angle amounts to $\gamma = \alpha + \beta \simeq 70°$ between the direction of the molecular nanowires and the molecular backbones (Figure 4.2.1 (d)). Previous NEXAFS studies [68, 69] pointed to a slight tilt of the phenyl moiety with respect to the surface plane, however, recent theoretical modeling strongly suggests a planar adsorption geometry of the molecules which will be discussed in more detail in an upcoming publication.

According to the modeling, the interaction between adjacent molecules responsible for the chain formation consists of two different bonds. Within the molecule pairs, a binding between the oxygen and opposite hydrogen moieties of the constituents functional groups is encountered, whereas, binding between the oxygen moieties towards the phenyl ring of the adjacent molecule of the next pair is found to link the pairs to another. The difference between the two chain motifs is attributed to the commensurate assembly of the chains in regards to the substrate registry. In contrast, when 3D bulk crystals are formed by the molecules, symmetric double O$\cdots$H bonds are formed.

4.2.2 Dense-packed Molecular Monolayer

For a coverage of a saturated ML, a dense-packed arrangement of the molecules is observed (see Figure 4.2.2 (a)). Even after evaporation of a sufficient amount of molecules onto a sample held at room temperature no multilayer formation occurred. We conclude that excess molecules do not stick or merely remain transiently and desorb again under these conditions (not shown). Therefore, a perfect dense-packed monolayer covering the entire surface can be easily constructed.

Similar to the sub-ML case, assemblies closely related to the substrate high symmetry directions are encountered. Further, *Left* and *Right* orientations related to the chirality of the assemblies are encountered (indicated in Figure 4.2.2 (b-d)). Therefore we can conclude that the assemblies still reflect chirality in regards to the substrate. When the molecule orientation within the supramolecular layer is examined in more detail (Figure 4.2.2 (e)), the high resolution scan clearly shows a distinctly different molecule assembly. In this case the supramolecular structure differs from the submonolayer (sub-ML) case because no pairing occurs within the entire domain. The angle α between the nanowire direction and the molecular backbone amounts to $\alpha \simeq 80°$ (see Figure 4.2.2 (e)). The packing scheme resembles the structure also found in the 3D bulk crystal [69].

In the ML, molecules can therefore be expected to show binding behavior found in the pairs of the nanogratings between adjacent molecules along the supramolecular chain substructure of the assembly. This explains the rectifying of the molecular chains to enclose an angle of $\alpha \simeq 80°$ rather than 70° in the sub-ML case. When the substructure of the ML is examined more closely, it appears that the molecular chains forming the substructure of the assembly are only spaced due to steric hindrance. In order to minimize the distance between the chains, adjacent chains are displaced by half the periodicity of the phenyl ring registry. Thereby, the phenyl ring outline of neighboring chains is interlocked in order to minimize the distance perpendicular to the chain directions.

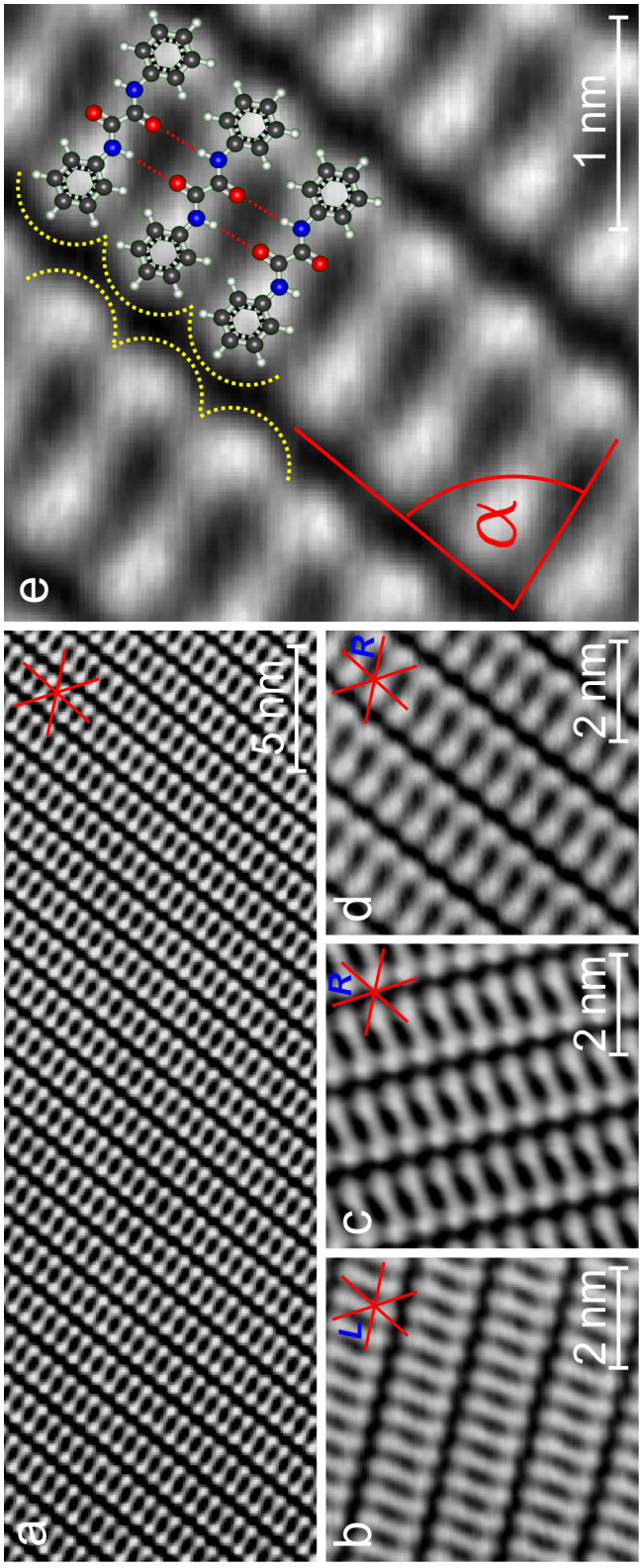

Figure 4.2.2: (a) Overview image of a dense-packed ML of N,N'-diphenyl oxalic amides (V_B = -0.2 V, I_T = 0.09 nA). (b-d) Higher resolution topographs show three orientation of the monolayer in respect to the high symmetry directions of the surface. No pair formation and displacement is observed as a substructure to form the dense phase. Therefore, the expression of chirality is suppressed. (V_B = -0.35 V, I_T = 0.1 nA to 0.25 nA). (e) High resolution image with superimposed molecular model highlights the bonding scheme The molecules form two hydrogen bonds with each adjacent molecule, which leads to an arrangement also observed in bulk crystals of the molecules. The alignment between the grating direction and molecular backbones is shifted and now amounts to $\alpha \simeq 80°$. The individual molecule lines are displaced relative to adjacent lines along the alignment direction by approximately half the periodicity of the wires to achieve full surface coverage (V_B = -0.31 V, I_T = 0.1 nA).

4.3 Template for Monomeric Cobalt Positioning

Recently, structures formed by bonding of Co dimers residing axially on benzene or graphene have been theoretically predicted to show huge magnetic anisotropies and were therefore proposed as candidates for magnetic storage applications [73, 74, 75]. To explore the route towards the realization of such structures, we employed the supramolecular assemblies from N,N'-diphenyl oxalic amide to produce arrays of single magnetic atoms on top of a molecular template. The organization and bonding of Co atoms on the surface templated by the molecular assemblies, on which Co adsorbs on top of the phenyl rings yielding Co-half-sandwich complexes [76, 77, 78], i. e., compounds with a single magnetic metal atom and Co clusters, is investigated. In the saturated organic layer case, the adsorption behavior depends on the substrate temperature during deposition and the cobalt coverage, yielding high amounts of Co monomers.

4.3.1 Deposition onto Nanogratings

Cobalt evaporation onto samples with sub-ML coverage of DOA, held at a deposition temperature (T_{dep}) of 130 K, leads to a decoration of the molecules appearing as white dots on gray molecules, whereas no adsorption on the silver surface (black) is observed (see Figure 4.3.1 (a&b)). For comparison, evaporation of Co onto the pristine surface without the organic template under similar conditions leads to the formation of clusters with a lateral size of several nanometers prevalently attached to the step edges [79]. Thus, in our case the presence of the molecular nanostructure suppresses the formation of large clusters and drastically reduces the size of the Co arrangements.

The smallest objects are in the sub-nm regime and situated on either side on top of the nanowires, but not in the center. However, there are also large clusters, frequently connected with breaking and bending of the molecular lines (see Figure 4.3.1 (c&d)). The limited stability of the nanowires hence prevents the expression of regular nanostructures. In contrast,

it was recently demonstrated by Decker *et al.* [80], that with a more stable template, namely a self-assembled metal-organic network constructed from dicarbonitrile-polyphenyl coordinated to Co centers [81, 82], it is possible to create metal clusters on top of the template without destroying the molecular layer.

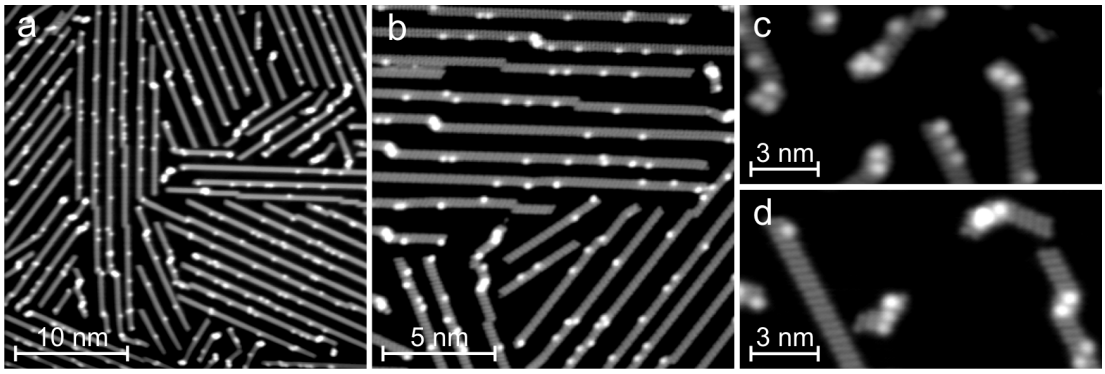

Figure 4.3.1: DOA Nanogratings after Co deposition at T_{dep} = 130 K. (a&b) Overview images show the molecular nanogratings (grey lines) on the Ag(111) substrate (black). Structures induced by Co adsorption are displayed as white protrusions, situated on either side of the molecule for the smallest units or as rather irregular shaped, spatially extended objects. Note that no adsorbates are found on the pristine surface, therefore the adsorption on the molecules is preferred over cluster formation on the substrate (V_B = -1.0 V and V_B = -0.34 V, I_T = 0.1 nA for both). (c&d) The drawback of the DOA nanogratings is the adsorbate induced breaking and bending of the molecule chains. Therefore, no high Co coverages are possible (V_B = -0.2 V, I_T = 0.1 nA).

4.3.2 Deposition onto Monolayer Templates

When Co is deposited onto the organic ML at T_{dep}=130 K, sub-nm sized structures evolve in a highly site-selective process, again. To determine the nature of the observed adsorbates, in a first step only very small amounts of Co were deposited, see Figure 4.3.2 (a). Due to the overall very low coverage ($\ll$ 0.1%) we can assume that the observed species represent the minimal adsorbate size of a single Co atom. With increasing cover-

age (Figure 4.3.2 (b-d)) the characteristic appearance of the smallest observed adsorbates remains unchanged, however more spatially extended structures evolve alongside. First, structures with similar diameter but increased height are observed (red circle in Figure 4.3.2 (b)), followed by the emergence of arrangements with irregular shape and size (red circles in 4.3.2 (c&d)), which can be interpreted as clusters consisting of several Co atoms. As evidenced in the high-resolution image in 4.3.2 (e), the smallest Co-induced nanostructures feature uniform structural characteristics.

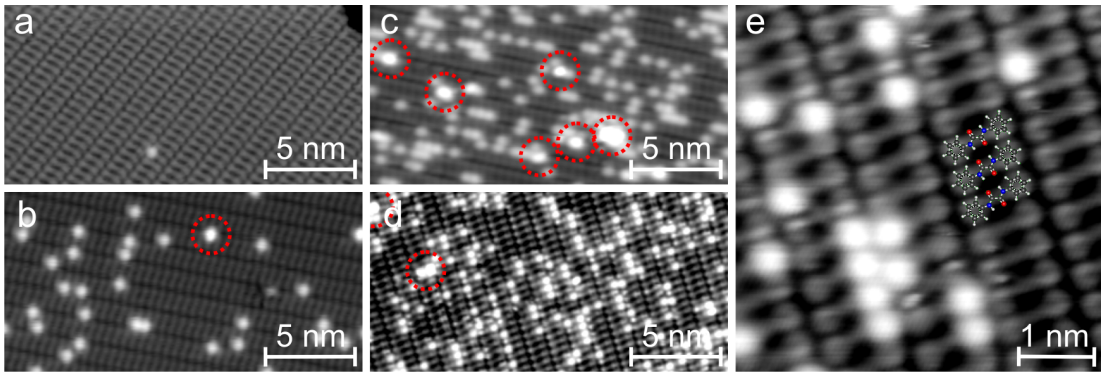

Figure 4.3.2: DOA Monolayer after Co deposition. (a) In the low coverage limit ($\ll 0.1\%$) Co adsorbates can be identified as circular protrusions situated on the phenyl ring of the molecule (V_B = -0.1 V, I_T = 0.09 nA). (b-d) With increasing coverage, also bigger structures situated on the molecular template evolve. First circular protrusions with increased height are observed (red circle in b), followed by the appearance of irregularly shaped accumulations of adsorbates (red circles in c&d) (V_B = -0.52 V, -0.9 V, -0.6 V I_T = 0.1 nA, 0.1 nA, 0.05 nA). (e) The high resolution scan reveals the exact appearance of the smallest observed adsorbed species. The adsorbates appear as circular protrusions, situated on either side of the molecule. They are centered on the phenyl rings and feature an uniform appearance. Therefore, the smallest units are interpreted as single Co atoms forming half-sandwich complexes on the phenyl rings (V_B = -1.0 V, I_T = 0.1 nA).

They are imaged as circular dots with an apparent diameter of $\sim$ 6 Å and an apparent height below 1 Å, with the exact height depending on the experimental conditions, mainly the state of the tip and the bias voltage. Co atoms are positioned at the phenyl ring positions of the molecules. From

the uniform shape and small size we conclude, that each dot actually represents a single Co atom. This interpretation is consistent with the amount of Co expected on the basis of the flux calibration of the evaporator used in the experiments. The unoccupied part of a molecule hosting a Co atom is imaged with the same characteristics as the corresponding part of a molecule without Co attached. This observation indicates, that the Co is residing on top of the phenyl ring. For the case of a Co atom positioned between the phenyl moiety and the Ag substrate, an uplift of the molecule would result, entailing a change in the appearance of the entire molecule, affecting the STM imaging of both phenyl moieties. Furthermore in such a case the lateral bonding scheme would be affected, which is not supported by the data. Also the possibility of the Co centers engaging in lateral metal-ligand interactions and connecting the reactive oxalic amide moieties must be excluded, because major rearrangements of the lateral order scheme appear in such situations [83, 84, 85]. Therefore, we conclude that uniform Co-half-sandwich structures [76, 77, 78] are formed.

In contrast to the sub-ML grating the saturated organic layer is stable enough to host high Co densities without a modification of its structure. This can be attributed to the high packing density increasing the stability due to more lateral intermolecular interaction and steric hindrance in contrast to the sub-ML regime. However, defect and cluster formation cannot be eliminated completely. As shown in Figure 4.3.2 (e), it is possible to prepare samples where the major part of the Co adsorbs monoatomically, whereas defects, i.e., clusters with more than one atom, appear as white regions with irregular shape and height. To investigate the formation and distribution of Co defects in comparison to monomeric adsorbates, the positioning statistics concerning the monomer distribution in dependence of the preparation parameters were studied.

4.4 Cobalt Positioning at Variable Temperature and Co-Coverage

In order to gain further insight into the effects governing the statistics and dynamics of the Co and DOA system, a series of experiments with variable preparation parameters, namely the substrate temperature during Co deposition and the total Co coverage, were carried out. To evaluate the statistics of the observed arrangements, first the nature of the individual adsorbates was determined.

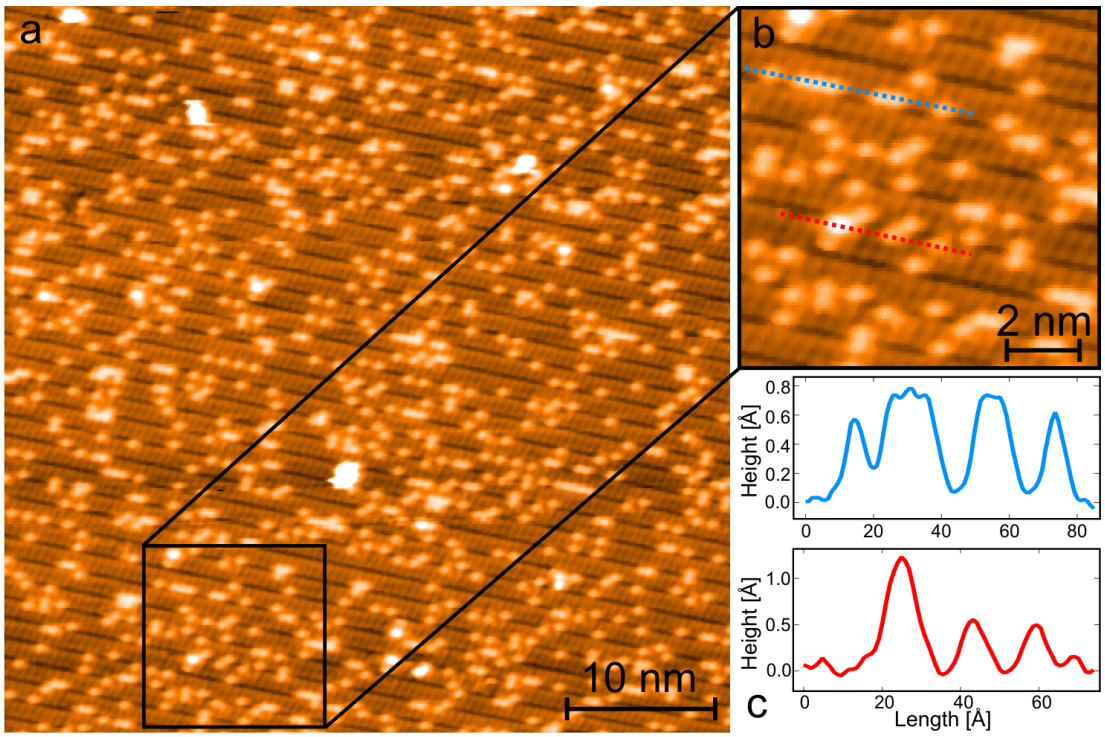

Figure 4.4.1: (a) Overview image of Co atoms adsorbed on the dense-packed ML (0.23 MLs, T_{dep}=180 K, V_B = 1.0 V, I_T = 0.1 nA). Co monomers appear as yellow protrusions, whereas defects are imaged as white protrusions on the orange molecular template. In a zoomed in area of the sample (b) an enhancement in the apparent height (~30%, from ~0.6 Å to ~0.8 Å) for adatoms adsorbed on neighboring phenyl rings (blue dashed line) can be distinguished from the enhancement (~100%, from ~0.6 Å to ~1.2 Å) due to the presence of a dimer (red dashed line) as can be seen in the corresponding line scans (c).

In Figure 4.4.1 (a), mainly small, uniform adsorbates (imaged as yellow dots residing on the molecular template depicted as orange, dog-bone like protrusions), corresponding to the smallest structures determined in the low coverage limit (Figure 4.2.2 (a)) are observed. A high-resolution image (Figure 4.4.1 (b)) is used to exemplify the following analysis of cluster sizes based on their apparent height. The upper linescan across a line of monomers (blue) shows a maximal variation of the apparent height of atoms adsorbed along the phenyl ring chain of adjacent molecules of only 0.2 Å (Figure 4.4.1 (c), upper panel). The lower linescan across two monomers and a cluster (Figure 4.4.1 (b), red) displays an apparent height difference of ∼0.6 Å, which can be clearly distinguished from the variations of the monomers. Clusters with characteristics as defined by the red linescan are assumed to consist of two Co atoms probably stacked upwards on one another. Such a stacking was already demonstrated on the bare Ag(111) surface for Mn atoms by Kliewer *et al.* [86]. Thus the protocols employed in our approach potentially yields the upright Co-dimers as proposed by Xiao, *et al.* [73, 74] and Cao, *et al.* [75] in small numbers. However, with increasing coverage higher concentrations of Co-dimers may become more likely to be formed.

In the following, the amount of Co monomers as a fraction of the total amount of deposited Co will be evaluated. For the statistical analysis of the monomer fraction in the conducted experiments the amount of Co captured in clusters was estimated by determining the size of the clusters and calculating the amount of Co atoms in the corresponding volume. For the cluster shape a radial cone geometry was assumed and an effective volume of 6 $Å^3$ for a single Co atom was estimated. This approach produces reasonable results at Co coverages of up to ∼0.4 MLs. However, at higher coverages or sample preparation in the temperature range outside the ideal regime the cluster size exceeds the limit under which reliable results are produced. Therefore, the Co deposition rate was determined from samples with 0.23 MLs coverage, yielding 0.0018 ML/s. For samples with coverages exceeding 0.34 MLs only monomers were evaluated and compared to the total amount of Co deposited in the experiment according to

the deposition time. All monomer fractions were normalized to the amount of Co calculated from the deposition rate and deposition time.

To evaluate the uncertainty of the determined monomer fraction, an inherent error of 10% for the total amount of Co deposited in the experiments (and therefore the deposition rate) was taken into account. Since after the flux was calibrated, only the amount of monomers was evaluated, the uncertainty of the MF varies with the deposition temperature and total coverage. The variation of the total amount of deposited Co entails an uncertainty of the monomer fraction in the range of 2.5% - 1.5% for low coverages. The error accordingly increases with increasing Co coverage, up to approximately 10% at 0.91 ML.

4.4.1 Temperature Dependency

First, we examine the ratio between monoatomic Co adsorbates and defects in dependence of the substrate temperature during Co deposition (Figure 4.4.2) alongside the evaluation procedure presented above. A series of experiments was carried out, wherein the total evaporated amount of Co was kept constant, while the sample temperature during metal evaporation was varied from 110 to 240 K. The nominal amount of Co was chosen to cover ∼23% of the phenyl rings provided by the template if all Co atoms were adsorbed monoatomically. Thus, the samples had a Co coverage of 0.23 MLs, defining the metal monolayer corresponding to one Co atom per one phenyl ring of the organic template.

For low temperatures, starting at 110 K (Figure 4.4.2 (a)), a substantial amount of the deposited Co atoms is found to form clusters (irregular, white protrusions) instead of to single atoms (yellow dots). The fraction of monoatomic Co of the total amount of deposited metal atoms, from here on referenced to as monomer fraction (MF), is determined to be ∼50%. In this fraction the total Co amount is the nominal amount calculated from the flux calibration and the evaporation time. With increasing sample temperature, the MF increases (Figure 4.4.2 (b&c)) until a maximum is reached at T_{dep}=190 K. An image recorded on samples prepared at T_{dep}=190 K and

T_{dep}=200 K (Figure 4.4.2 (d&e)) demonstrates that the majority of adsorbates appear as circular and uniform protrusions, whereas defects show a tendency towards increased size, but clearly form less frequently. Under these optimal deposition conditions the MF peaks at ∼80%. For temperatures exceeding 200 K cluster formation increases, therefore the MF declines. As shown for 220 K and 240 K in Figure 4.4.2 (f&g), the number of single atoms (yellow protrusions) is strongly reduced, whereas the formation of clusters with rather similar shape and size (bright protrusions) is encountered at the end of the investigated temperature range, with the MF being reduced to ∼45%.

The dependence of the MF on T_{dep} is displayed in Figure 4.4.2 (h), where the value for all samples of the series are given with blue dots. The curve exhibits a maximum at an optimal temperature T_{opt} = 190 K. With increasing temperature difference to T_{opt} the MF decreases monotonically to lower as well as to higher temperatures. This behavior suggests two competing effects which govern the ordering process. Based on the comparison with the model value we suggest the following scenario to govern the MF dependence. The MF at low temperature ($T_{dep} < T_{opt}$) is significantly less than the expectation value calculated in the hit-and-stick model, where a random bonding at phenyl moieties without diffusive displacements is posed (see p. 12 for further discussion and SI for a detailed description of the calculation procedures). This difference indicates spurious or hidden effects leading to cluster formation, with Co atoms possibly undergoing transient motion after their impact on the organic layer until the adsorption energy is dissipated (note that such effects have been rarely reported for metals [47, 87] and frequently involve precursor states in the adsorption process [46]). With increasing T_{dep} less clusters evolve until at T_{opt} the model MF for Co monomers is reached, which can be reproduced within the simple hit-and-stick model. In the high-temperature regime ($T_{dep} > T_{opt}$), thermally activated processes mediate the formation of larger clusters which are stable at these temperatures and to which the monomers may aggregate.

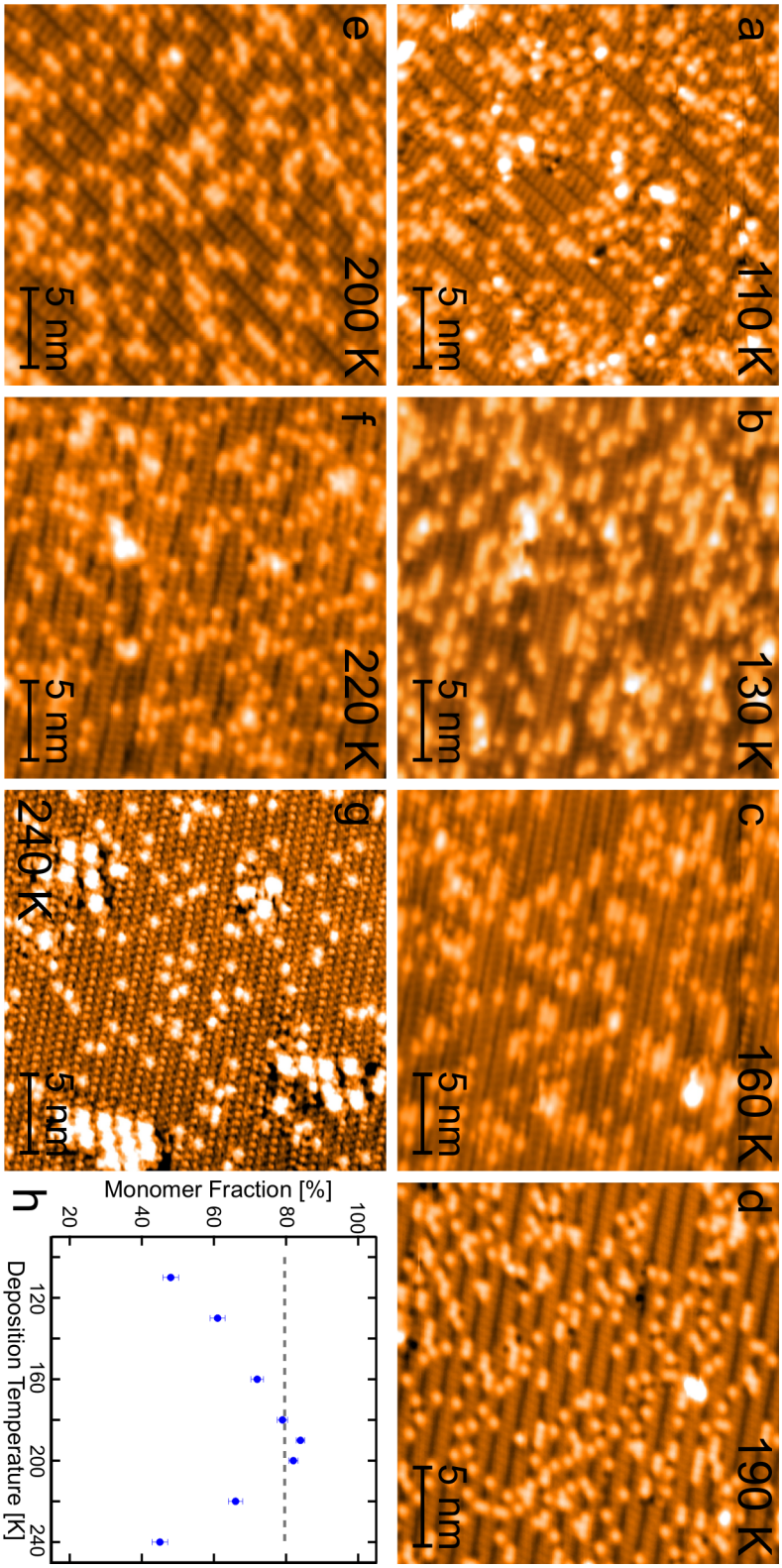

Figure 4.4.2: Exemplary topographs of samples with a constant Co coverage (0.23 MLs) evaporated at varying deposition temperatures (T_{dep} as indicated) onto the dense-packed organic template and monomer fraction analysis for the complete series of experiments. (a-g) For different deposition temperatures, distinct distributions of the Co adsorbates is observed. At lower temperatures (a-c) first a statistical distribution with increasing monomeric adsorption towards higher temperatures is found. In the intermediate temperature range (d&e, for 180 K see Figure 4.4.1) mostly Co monomers and very little clusters are encountered, whereas for high temperatures (f&g) cluster formation increases again until rather uniform clusters in shape and size evolve. (h) The monomer fraction is small (~40%) at both ends of the studied temperature range and increases monotonically towards the optimal deposition temperature (T_{dep} = 190 K). The gray dashed line indicates the value expected for such a coverage from a simple hit-and-stick statistics. Under ideal deposition conditions this value is nominally slightly exceeded.

4.4.2 Optimized Protocol at Increasing Coverage

After optimizing the deposition temperature, a series of samples was prepared with increasing Co coverage at T_{dep} = 180 K. The coverage was increased in three steps from 125 s deposition time, corresponding to 0.23 ML of Co, to 510 s, corresponding to 0.91 ML of Co. Exemplary topographs from this series of experiments are shown in Figure 4.4.3 (a-c).

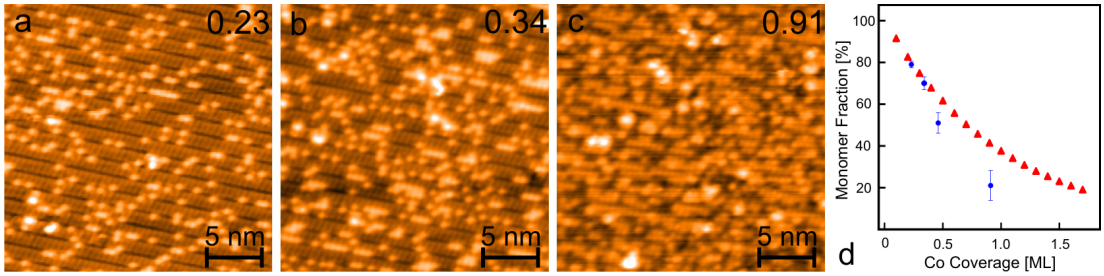

Figure 4.4.3: (a)-(c) Overview topographs of samples with increasing Co coverage and constant T_{dep} = 180 K. The fraction of a ML is indicated in the upper right corner of each image. With increasing coverage an increase of Co atoms arranged in linear chains is observed (V_B = 1.0 V, I_T = 0.1 nA for all). (d) The MF decreases with increasing coverage (blue dots, Co flux of 0.0018 MLs/s during deposition). The calculations (red triangles) following a hit-and-stick adsorption in the diffusionless limit show a deviation from experimental values (blue dots) for Co coverages exceeding ~0.4 MLs.

In Figure 4.4.3 (a), the majority of Co atoms adsorb as single species (yellow protrusions on orange molecular template), whereas the amount of clusters (brighter protrusions) is comparably low. With increasing Co coverage (Figure 4.4.3 (b)) the amount of monomers increases as well as the density of defects. At high Co density (0.91 ML in Figure 4.4.3 (c)) it becomes difficult to make a clear distinction between monomers and other features. The result of a statistical analysis of the MF for the four coverages 0.23, 0.34, 0.47 (topograph not shown) and 0.91 MLs is reproduced in Figure 4.4.3 (d) (blue dots). With increasing Co coverage the MF decreases monotonically.

4.4.3 Theoretical Analysis of Co Distribution

To gain further insight into the positioning process, we simulated the distribution of atomic Co on the molecular precursor following a strict hit-and-stick process. In these calculations we assumed that adsorbates do not perform any diffusion steps across the molecular precursor, but rather directly stick to the first adsorption site encountered upon impact. As adsorption site the area of a phenyl ring is taken into account and sticking to this site is possible no matter whether the phenyl ring is still free or already occupied by a previous Co atom. In the model the adsorption sites cover the full surface, i. e., Co atoms hitting the central moiety of the organic building block are counted to the nearest adsorption place. In the set of calculations presented, surfaces with 1000 adsorption cells were utilized. Adsorbates are then positioned on this template by evenly distributed random numbers determining the adsorption site on that the Co atom resides. Subsequently, the number of cells occupied by a single adsorbate is determined and thereby the monomer fraction of the total number of adsorbates is calculated. To reduce statistical errors, several iterations (typically 1000) of this algorithm were run in sequence and an average for the monomer fraction was calculated. By assuming a random statistical distribution for hitting the different adsorption sites, an expectation value for the MF was calculated. As shown in Figure 4.4.2 (h) the expected value for the MF from this simulation is ∼79% (gray dashed line) for a coverage of 0.23 MLs of Co. The evolution of the MF depending on the Co coverage at 180 K is compared to the respective expectation values in Figure 4.4.3 (d).

Comparing the experimental results of the MF in dependence on the coverage to the statistical hit-and-stick analysis, it is found that for coverages up to 0.34 MLs the experimental MF can be reproduced with numerical predictions. However, for higher coverages the fraction of Co monomers falls below the calculated value. This discrepancy is consistent with the hypothesis that the formation of stable clusters depends on the statistic probability of Co collision events, which in turn increases with coverage at identical temperatures.

4.5 Conclusion

To summarize, we demonstrated a novel approach towards the construction of arrays of single magnetic atoms. When Co atoms adsorb on top of phenyl rings, provided by an organic template, namely a dense-packed layer of N,N'-diphenyl oxalic amides, monoatomic Co-half-sandwich complexes and multiatomic Co clusters, with relative amounts of each depending on the sample temperature during deposition, are formed. The deposition conditions were optimized to yield a high portion of monomer complexes. The optimal temperature of the substrate was found to be in the range of 180 - 200 K. The nonlinear formation dynamics of the monoatomic Co adsorption is interpreted to be a result of two competing effects, leading to the formation of small clusters at low temperatures and the statistic formation of stable large clusters at high temperatures, respectively.

The realized half-sandwich compounds bear interesting aspects for surface-confined metallosupramolecular chemistry [88, 89]. They notably represent potential templates to create surface analogons to bis(benzene) organometallic sandwich complexes. Employing an organic molecular template anchored on a surface may therefore prove to be a feasible route towards the construction of novel magnetic storage devices as proposed recently by theory [73, 74, 75].

In conclusion, this work demonstrates the possibility of creating hybrid organometallic surface nanoarchitectures constructed from single atoms using an organic molecular precursor, which acts as an ordered template for atomic organization. Structures constructed in this fashion may open up new possibilities for the realization of novel nanomagnetic or spintronic concepts, whereby single atoms and their spins act as smallest functional units.

Chapter 5

Hierarchic Formation of Bi-component Organic Molecular Networks

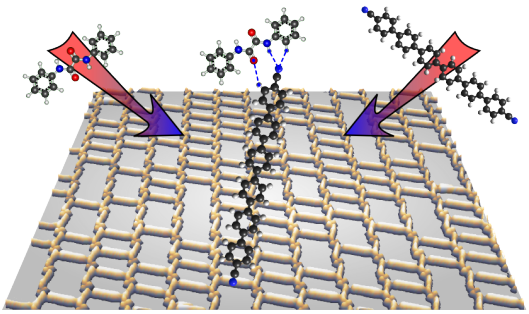

For the construction of functional nanostructures, molecules as smallest functional building blocks have been under extensive research in recent years [14, 15, 83, 84, 89, 90, 91, 92, 93]. Moreover, investigations towards the realization of functional structures like molecular switches, motors and rotators have demonstrated the great potential of this surface supramolecular chemistry approach [94, 95, 96, 97]. Further studies foresee applications in nanomagnetism [18, 59, 60, 66, 98, 99] or gas sensing [100, 101, 102, 103]. Molecular self-assembly on various surfaces has been studied, leading to nanogratings [69, 104, 105] or open-porous nanomeshes [81, 82, 106], which can be further functionalized or used as templates for the growth of host lattices to steer atomic or molecular motion [96]. In an attempt to increase the control

over the resulting architecture, protocols following hierarchic principles due to different bonding mechanisms and strengths are of great interest since it is also an intriguing concept found in natural systems [107, 108, 109, 110, 111, 112]. Hierarchic self-assembly requires specific functional groups of the presynthesized building blocks engaged in multiple bond motifs at different organizational levels, thus putting further emphasis on the control over the binding energetics of the systems and the bond-types involved in network formation [113, 114, 115, 116, 117, 118, 119, 120]. Moreover, a variety of geometric arrangements can be achieved when multicomponent mixtures self-assemble on the surface [121, 122, 123, 124, 125]. Therefore, developing hierarchic organization principles to steer the growth of nanostructures is an important step towards functional molecular nanoarchitectures. In the following, an approach towards the realization of hierarchic assembly of an open porous molecular template through the co-deposition of chemically functionalized organic molecules, namely N,N' diphenyl oxalic amide (DOA) and sexiphenyl dicarbonitrile (SDC) (see Figure 5.1.1 for structure models) is presented. We investigated how the resulting supramolecular structures depend on the stoichiometric ratio of the molecular constituents provided during growth. It was found, that for ratios with higher SDC fractions an open-porous ladder-pattern is realized, where the excess SDC that is not bound to a DOA acts as a spacer between SDC-DOA wires. At an even ratio, a dense-packed phase with minimal pore size is found. Here the spacing of the SDC-DOA wires is dictated only by steric hindrance. For ratios with higher DOA concentration a formation of networks following the arrangement of the pure DOA nanowires on the one hand and SDC closely related to the high symmetry directions of the substrate on the other hand is found to occur. The experimental findings are further analyzed utilizing first principle calculations for the binding energies of the observed arrangements. The simulations unravel the energetics of the different binding at hand and allow for a better understanding regarding the specifics of the observed networks and the principles driving the hierarchic growth. This chapter was published in Reference [126]. Reprinted with permission. Copyright 2012 American Chemical Society.

5.1 Molecule Properties, Sample Preparation, and Theoretical Approach

The molecules used in the experiments are N,N'-diphenyl oxalic amide (DOA) and sexiphenyl dicarbonitrile (SDC), see Figure 5.1.1. The organization of pure DOA nanogratings was presented in the previous chapter. SDC features six phenyl rings in linear arrangement bonded by σ C-C bonds and terminated on either end with a carbonitrile group. The constituents were deposited from a quartz crucible in an organic molecular beam epitaxy (OMBE) source at 379 K and 585 K for DOA and SDC, respectively, while the substrate was held at the room temperature. The Ag(111) surface was prepared by repeated cycles of Ar^+ sputtering (flux approx. $7\frac{\mu A}{cm^2}$) and annealing to 740 K, in order to obtain flat terraces separated by monoatomic steps. LT-STM measurements were conducted at temperatures below 14 K after the samples were cooled down.

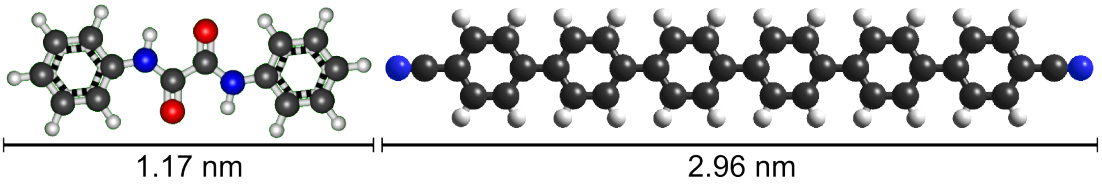

Figure 5.1.1: Structure models of the molecules used in the experiments (H white, C black, O red, N blue). The respective length in gas phase is indicated for N,N'-diphenyl oxalic amide (left) and sexiphenyl dicarbonitrile (right).

The adsorption models for the different network phases were constructed by positioning ball-and-stick models of the molecular constituents on a model of the hexagonal Ag(111) lattice. The orientation of the underlying substrate was determined several times by atomically resolved STM measurements and can be assumed to be constant throughout the experiments conducted on the same single crystal. Relative positions and orientations of the molecular building blocks were extracted from numerous experiments for each phase. In a first step the orientation of the SDC-DOA chains was

determined relative to the substrate high symmetry directions, followed by positioning the nitrogen atoms of the end groups over hollow sites of the substrate. Thereby, the periodicity of the assembly and the exact position of the molecules and their functional units relative to another were determined and finally compared to experimental data.

For the simulation of binding energies, we used first principle methods, and more precisely the Density Functional Theory framework, within the Projector Augmented-Wave approach and the Local Density Approximation on exchange-correlation energy, as implemented in the Abinit code [127, 128]. For the large superstructure unit cells exhibited by the networks, a global approach, i. e., the simultaneous simulation of molecules and substrate, is extremely demanding with respect to computational resources. Thus, thorough investigations of the binding energy landscape as well as the role of each component (molecules, substrate) cannot be conducted due to practical time restraints. Furthermore, this heavy global approach suffers of several limiting parameters: the very thin substrate used (down to 1 monolayers), the tight simulation cells considered, and the use of light exchange correlation functionals that poorly reproduce the van der Waals interaction between molecules and the substrate. Here, we have deliberately decided to use an adlayer-focused approach, in which only the molecular interactions are simulated within the DFT framework and the substrate is considered merely as a position-selective filter. Since computations then are faster, this approach can be used for a stepwise understanding of the underlying construction principles. In more detail, we first characterized the original driving forces for the different binding motifs between isolated species by fully relaxing the systems. Then, several maps of the interaction energy versus the relative position of the two rigidly displaced molecules are calculated. This provides a complete overview of the binding energy landscape around the optimal binding positions of the fully relaxed simulations. Then, the theoretic binding energy for the different networks is computed by taking into account the relative positions of the organic constituents as defined by the strong constraints of the substrate periodicity.

5.2 Different Networks Depending on the Stoichiometry

The pure phases of the DOA and SDC molecular building blocks employed in this study have been investigated previously [68, 69, 106]. It was shown that templates grown from these moieties can be utilized to act as host lattices to confine supramolecular rotors [96], to control surface electronic states in arrays of quantum dots [40, 41] or steer the adsorption of single metal atoms [66] and clusters [80].

SDC network formation in the pure phase is driven by the interaction of the carbonitrile moieties with the aromatic rings of adjoining molecules where a four-fold coordination theme is observed [106]. The homo-bonded networks feature several geometries depending on molecule coverage, whereas honeycomb nanomeshes are formed exclusively following cobalt exposure [82]. In STM the molecular bricks appear as double protrusions connected by a thinner waist for DOA, whereas SDC appear as longer stick-like features (Figure 5.2.1 (a-d)). When both molecules are co-deposited on the Ag(111) metal surface, new networks evolve (Figure 5.2.1 (a-c)), where the binding of the carbonitrile terminations of the SDC to the central part of the DOA proves to be the preferred binding motif among all (see Figure 5.2.1 (d) for a schematic of all motifs). After cooling the arrangements down to liquid helium temperature, no patterns exclusively formed from a single type of molecule was observed as long as sufficient amounts of either constituent were provided. Therefore, hetero-bonding (SDC-DOA$^{\alpha}$ in Figure 5.2.1 (d)) can be assumed to be favorable over homo-bonding, preventing the formation of pure phases. The different realized network geometries depend on the stoichiometry, where first the lower ratio constituent is utilized to saturate the SDC-DOA bonding, before excess molecules of the other constituent determine the exact arrangement. Therefore, molecular self-assembly driven by hierarchic principles persists.

For ratios with excess SDC in respect to DOA the formation of a ladder-shaped network, in which SDC acts as rung-like spacers, is observed (Figure

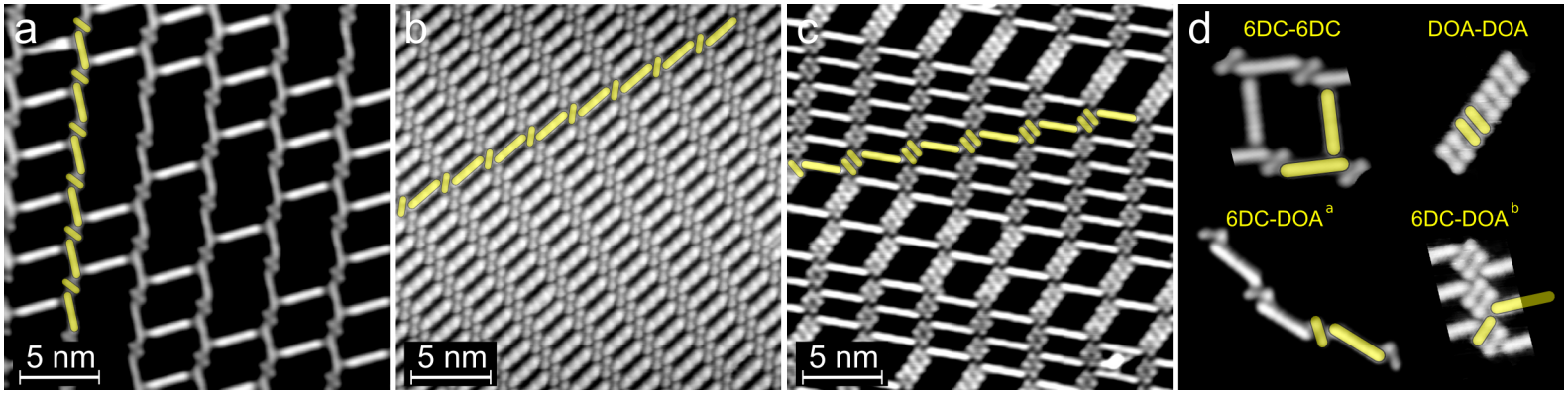

Figure 5.2.1: The energetically favorable SDC-DOA^{a} chains driving the network formation are indicated with yellow bricks. (a)-(c) Different network types formed depending on stoichiometry: (a) Open porous phase with SDC:DOA = 2:1. After the formation of SDC-DOA-chains excess SDC act as spacers interconnecting the lines establishing a ladder-shaped geometry (I_T = 76 pA, V_B = 0.2 V). (b) At even ratio 1:1 no spacers are present and the lines are dense-packed maintaining their original directionality, while the distance is limited only by steric hindrance (I_T = 68 pA, V_B = 0.8 V). (c) With increasing DOA concentration (1:2 - 1:6) again open-porous arrangements are formed where pairs of DOA interconnecting the SDC-DOA-planes define the exact geometry. Thereby variable pore sizes are observed while the long range order of the network remains intact (I_T = 72 pA, $V_B = -1$ V). (d) Schematic of the elementary coordination motifs observed in all networks. The SDC-SDC and DOA-DOA bondings also observed in the respective pure phases reemerges at excess concentration of either species. At even ratio only the novel SDC-DOA coordination is present in the entire domain. As can be seen at low coverage also chirality interconversion along a SDC-DOA^{a} chain appears.

5.2.1 (a)). From a detailed analysis it became clear that the SDCs in the mixed chains follow closely the high symmetry directions of the substrate (indicated by a yellow star) enclosing an angle of 1.6° between the molecular backbone and the high symmetry orientations, whereas the rungs connect the chains bonding under ∼83° to the aromatic rings. This phase features pores with a van der Waals area of approximately 7 nm^2.

At an even ratio of SDC and DOA a dense phase of SDC-DOA chains is observed (Figure 5.2.1 (b)), where only SDC-DOA interactions are present (both SDC-DOA^a and SDC-DOA^b shown in Figure 5.2.1 (d)) in the entire domain. The rows are dense-packed while the assembly appears to be only spaced due to steric hindrance perpendicular to the growth direction of the chains. The samples were prepared with an higher ratio of SDC than DOA at high coverage. The dense phase covered entire terraces, whereas partially empty terraces were observed in between. The partially covered terraces were then filled exclusively by SDC that was not involved in SDC-DOA binding. Therefore, the 1:1 phase evolves by increasing the total coverage of the 2:1 phase to a point where rungs no longer interconnect SDC-DOA chains but are instead removed from the bi-component domains entirely.

When the relative amount of DOA is increased, the formation of DOA-chains as observed in the pure phase reemerges as a binding motif (Figure 5.2.1 (c)). Instead of single DOA molecules with one SDC binding on either side of the functional unit, pairs or numbers thereof acting as binding points are encountered. Only blocks of two or multiples of two are observed as spacers but never odd numbers of DOA molecules connecting the SDC planes. We therefore conclude that the pair-formation is also the basic principle as for the molecular nanogratings of pure DOA. With an increasing amount of DOA spacers also increasing pore sizes with van der Waals areas of approximately 2 nm^2 for two spacers up to 7 nm^2 for six spacers are observed.

For all types of arrangements it was found that the symmetry of the substrate was reflected in the networks, giving rise to three orientation domains (rotated by 60°) for each handedness (*Right* or *Left*) as illustrated in Figure 5.2.2. The handedness of the assemblies reflect the two chiral

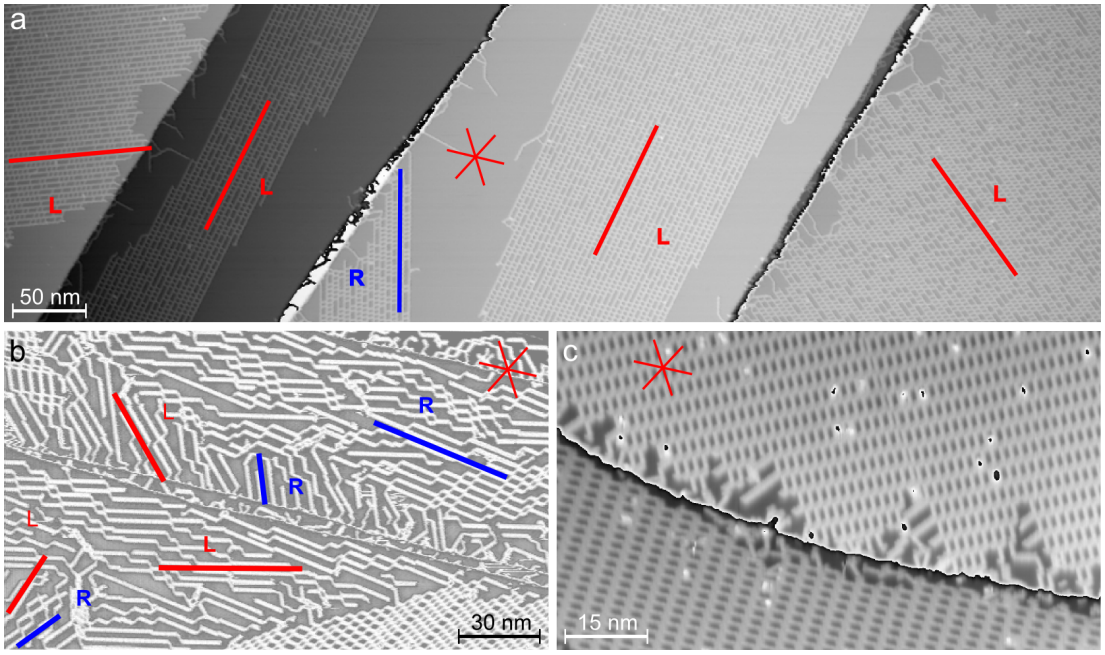

Figure 5.2.2: STM image of different networks arising at different SDC:DOA stoichiometries. *Right* and *Left* handedness of the domains are marked by blue *R* and red *L* letters respectively. High symmetry directions of the substrate are indicated with red stars. (a) Large area image of the open porous 2:1 phase. From the long-range order and continuously unchanged geometry, a commensurate adsorption pattern on Ag(111) is plausible. The observation of different directions related to the high symmetry directions of the substrate and different handedness further suggest commensurate ordering (I_T = 76 pA, V_B = −0.6 V). (b) Different directional arrangements and handedness of DOA lines interconnected by single SDC are observed in samples with high DOA concentration, pointing towards a commensurate adsorption pattern (I_T = 78 pA, V_B = −0.7 V). (c) Sample with SDC:DOA close to 1:2 ratio demonstrates the preference of the SDC-DOA bond over pure SDC-SDC and DOA-DOA coordinations. No pure phases of either constituents are observed (I_T = 66 pA, V_B = 0.8 V).

orientations of DOA, where SDC either connects towards the *Right* or *Left* side of DOA along the chain directions. This leads to a rotation of the chain directions away from the high symmetry directions of the substrate.

In Figure 5.2.2 (a), the different chiral arrangements of the 2:1 ladder

shaped network are evidenced along with the related handedness as indicated. The *Right* and *Left* rotations away from the related high symmetry directions are clearly observed along with the long range ordering in the 2:1 phase. When only small relative amounts of SDC are provided during growth, chains of DOA formed from pairs as in Figure 5.2.1 (c) evolve again exhibiting different handedness. Higher local SDC concentration leads to the same structure found in Figure 5.2.1 (c) as can be seen in the bottom right portion of Figure 5.2.2 (b), whereas no long-range order is observed in the remainder of the scan range. SDC there merely interconnects DOA chains, leading to step-like chains. After an increase in SDC close to the 1:4 scenario from Figure 5.2.1 (c), extended domains with high quality evolve covering entire terraces of the substrate in the high coverage regime (Figure 5.2.2 (c)), where defects are observed only close to the step edges. From the observed long-range ordering and different chiralities of the individual phase, we conclude that the adsorption of all phases can be assumed to be commensurate with the substrate, due to the substrate symmetry and periodicity being reflected in the networks.

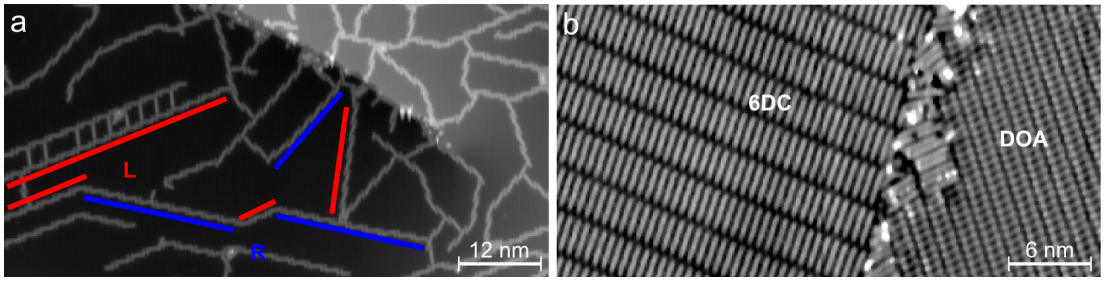

Figure 5.2.3: (a) For low coverages no long range ordered networks evolve, but rather short chains of SDC-DOA also showing chirality interconversion are encountered (I_T = 63 pA, V_B = −1.2 V). (b) After a full monolayer of DOA was deposited, SDC deposited afterwards thrusts DOA out of the preassembled monolayer and dense-packed networks as in the pure phase of each constituent evolve rather than the dense phase of the bi-component network ($I_T = 84$ pA, $V_B = -1.4$ V).

Finally, in order to examine the impact of the total coverage, samples with very low and very high molecular coverage were prepared. In the case

of extremely low coverage, it is found that only the SDC-DOA binding is realized in short chains, see Figure 5.2.3 (a). However, no long range order is observed, but rather short chains following the different surface directions as found in the long-range order bi-molecular networks described above. These chains also show chirality interconversion along the chains, which in turn leads to the conclusion that no highly regular and mono-chiral extended networks, such as islands, form in the low coverage regime. The expression of regular networks therefore requires a sufficiently high total coverage. In the other extreme case, samples were prepared in a different fashion. Rather than depositing low to medium amounts of either constituent, first an entire monolayer of DOA was deposited. Due to weak vertical bonding, no adlayer formation occurs for pure DOA deposition at room temperature [66]. In a second step, an amount of SDC corresponding to ~ 0.5 monolayers was deposited onto the saturated DOA layer. After cooling down it was found that dense-packed networks known from either constituent in the pure phase at high coverage [66, 106] are formed, see Figure 5.2.3 (b). This leads to the conclusion that SDC molecules penetrate and thrust out DOA molecules from the predeposited monolayer, which in turn desorb due to weak vertical bonding. SDC then forms dense-packed islands inside the DOA layer or cover entire terraces. Therefore, at saturated coverage no bi-component networks similar to the dense packed phase discussed above are formed but a dense assembly based on the pure phases is encountered.

5.3 Network Characteristics

To determine the orientation and exact alignment of the molecules in the networks and on the surface, the orientation of the underlying Ag(111) surface was determined beforehand via STM. Furthermore, angles between motifs of *Right* and *Left* handedness domains in the same pictures were extensively measured to minimize the impact of drift in the STM images. Thereby, it was possible to compare experimental findings with adsorption models for the different phases discussed before. In investigations of pure organic SDC networks it was shown recently that the aromatic backbone of the SDC does play an important role in the orientation of the molecules [106]. It was found that the molecules align predominantly along crystallographic directions of the substrate so that the nitrogen atoms rest over hollow or bridge sites. Following the principles for the construction of adsorption models in this previous work in combination with the known relative orientation of the DOA and the directionality of the Ag(111) surface underneath, it was possible to understand the principles governing the molecule adsorption in the bimolecular structures. For simplicity, only planar models for the molecules are displayed, where the length of both SDC and DOA are those determined for the gas phase. All models fit experimental data with only minor corrections for extended domains, therefore the experimental error is negligible (< 3%).

Adsorption models presented in Figure 5.3.1 were constructed by positioning ball-and-stick models of the molecules on the hexagonal Ag(111) substrate (blue-gray circles, hollow sites are indicated by green dots). They are superimposed onto experimental data for each phase, with the unit cells in combination with the corresponding unit cell vectors indicated by transparent red and green areas along with arrows, respectively. The unit cells representing the basic ordering in all stoichiometric mixtures are found in the dense 1:1 phase in Figure 5.3.1 (b). This unit cell can then be expanded accordingly to deliver the unit cells for different SDC:DOA ratios as will be discussed in the following.

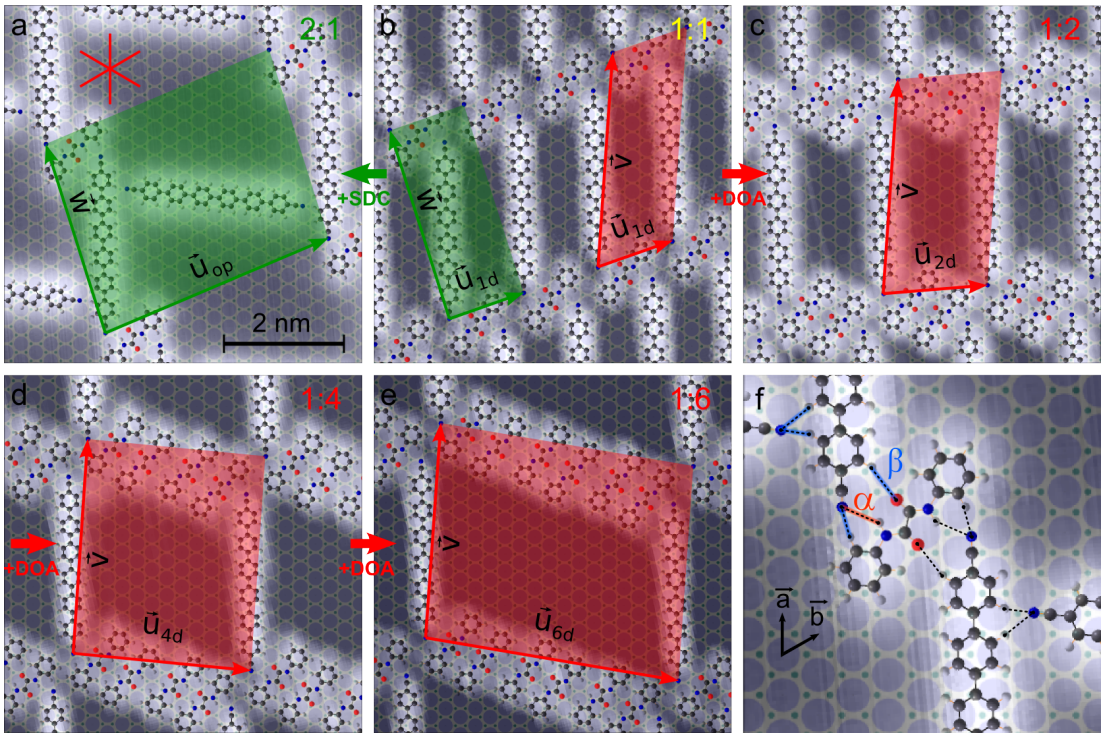

Figure 5.3.1: (a)-(e) Adsorption models for networks at different stoichiometry. Stick-and-ball models for molecules are placed over a model of the Ag(111), and superimposed onto experimental data, showing good agreement. Unit cells are indicated in red and green. (a) Open porous phase with SDC:DOA ratio of 2:1 per unit cell (b) Dense packed phase 1:1 (c)-(e) Increasing DOA concentration from 1:2 up to 1:6 shows systematic increase of pore size while the direction of the SDC-DOA chains is maintained. (f) Close up model of bonding in the elementary SDC-DOA motif. Two types of interactions connect the molecular constituents. A hydrogen bond (bond α, in red) contributes to the connection between SDC and DOA, and a weak interaction (bond β, in blue) between a proton acceptor (carbonitrile end groups or oxygen atoms) and the hydrogen atoms of the aromatic rings finished the connection between SDC and DOA and binds SDC constituents to one another in the open porous phase. $\vec{a}$ and $\vec{b}$ indicate the lattice vectors used to describe the unit cell vectors in the models ($|\vec{a}|=|\vec{b}|=2.89$Å).

The open porous phase (see Figure 5.3.1 (a)) features chains built from successive SDC and DOA moieties, where an angle of 44° is found between the constituents. The SDC constituents of these chains are aligned close to the high symmetry directions of the substrate (1.6° between molecular backbone and substrate orientation), whereas the SDC molecules, acting as spacers, bind under 83° in between the first and second aromatic ring of the SDC in the chains. The unit cell (green) therefore is constituted from one DOA and two SDC with the vectors describing the unit cell pointing along the

$$\begin{pmatrix} \vec{W} \\ \vec{U}_{op} \end{pmatrix} = \begin{pmatrix} 11 \cdot \vec{a} - 4 \cdot \vec{b} \\ 15 \cdot \vec{b} - 2 \cdot \vec{a} \end{pmatrix}$$

direction with respect to the surface unit cell defined by $\vec{a}$ and $\vec{b}$. The nitrogen atoms of the both SDC types (in the chains and the spacers) functional groups are situated close to the hollow sites of the Ag(111) lattice in close agreement with the modeling by Kühne *et al.* [96, 106].

In the adsorption model for the dense-packed phase, shown in Figure 5.3.1 (b), the orientation of SDC-DOA chains is identical (hence the same vector $\vec{W}$, green) to the orientation also found in the open porous phase. The lack of SDC spacer gives rise to a dense-packed arrangement, where every molecular line is shifted by $\vec{U}_{1d}$ in respect to the adjacent rows. The unit cell is then:

$$\begin{pmatrix} \vec{W} \\ \vec{U}_{1d} \end{pmatrix} = \begin{pmatrix} 11 \cdot \vec{a} - 4 \cdot \vec{b} \\ 5 \cdot \vec{b} - 1 \cdot \vec{a} \end{pmatrix}$$

One must however note that the vector $\vec{W}$ can be replaced by the vector $\vec{V}$ to have the equivalent unit cell:

$$\begin{pmatrix} \vec{V} \\ \vec{U}_{1d} \end{pmatrix} = \begin{pmatrix} 12 \cdot \vec{a} + 1 \cdot \vec{b} \\ 5 \cdot \vec{b} - 1 \cdot \vec{a} \end{pmatrix}$$

When a higher concentration of DOA is present, they tend to assemble into pairs, breaking the simple SDC-DOA chains. Therefore, the vector $\vec{W}$ no longer persists throughout the observed assemblies but rather the vector $\vec{V}$ defines then the new periodicity, originating from the red unit cell defined in Figure 5.3.1 (b). One can observe that the binding between SDC and DOA molecules in the SDC-DOA chains (Figure 5.3.1 (b)) is identical to that in the

SDC-DOA_2 (Figure 5.3.1 (c)) chains. This implies that both DOA units within DOA pairs must be of the same handedness, otherwise the carbonitrile end-group of the SDC would align with the oxygen moiety of the DOA, which in turn is not possible due to strong repelling forces. This contravenes with the hypothesis proposed in a previous work [68], and will be detailed in a separate publication.

Coming back to the unit cells of the networks presented in Figure 5.3.1 (c-e), we observe that they consist of one SDC and two, four or six DOAs, respectively. The unit cell along the new SDC-DOA chain remains the vector $\vec{V}$, whereas the vector in the direction of the DOA chains ($\vec{U}_{\mathrm{nd,n=2,4,6,...}}$) increases by $\vec{\Delta} = 5 \cdot \vec{b} - 4 \cdot \vec{a}$ for each supplementary DOA pair, maintaining strict periodicity between the network and the Ag(111) substrate. The unit vectors thus evolve from:

$$\begin{pmatrix} \vec{V} \\ \vec{U}_{1d} \end{pmatrix} = \begin{pmatrix} 12 \cdot \vec{a} + 1 \cdot \vec{b} \\ 5 \cdot \vec{b} - 1 \cdot \vec{a} \end{pmatrix}$$

to

$$\begin{pmatrix} \vec{V} \\ \vec{U}_{2d} \end{pmatrix} = \begin{pmatrix} 12 \cdot \vec{a} + 1 \cdot \vec{b} \\ 7 \cdot \vec{b} - 3 \cdot \vec{a} \end{pmatrix}$$

$$\begin{pmatrix} \vec{V} \\ \vec{U}_{4d} \end{pmatrix} = \begin{pmatrix} 12 \cdot \vec{a} + 1 \cdot \vec{b} \\ 12 \cdot \vec{b} - 7 \cdot \vec{a} \end{pmatrix}$$

$$\begin{pmatrix} \vec{V} \\ \vec{U}_{6d} \end{pmatrix} = \begin{pmatrix} 12 \cdot \vec{a} + 1 \cdot \vec{b} \\ 17 \cdot \vec{b} - 11 \cdot \vec{a} \end{pmatrix}$$

The commensurate adsorption of the bi-component networks allows an easy rationalization of the long range order demonstrated in Figure 5.2.2.

5.4 Theoretical Analysis of Binding Motifs and Hierarchic Assembly

In order to understand the origin of the observed hierarchic organizations, we simulated the different bonding motifs identified experimentally. Details on the computational methods are found in the methods section. The energy optimized geometries of the different binding motifs as obtained from full relaxation simulations are displayed in Figure 5.4.1 (a-c). As already indicated in Figure 5.3.1 (f), the total binding strength can be deconvoluted into strong (α) and weak (β) contributions of the individual bonds involved. The contributions to the total binding energy of the SDC-DOA motif were deconvoluted by further performing calculations where the carbonitrile moiety attached to the SDC phenyl ring was replaced with a hydrogen atom (not shown). Thereby, the contribution of the CN$\cdots$HN bond could be extracted via comparison with the contributions of only the lateral CN$\cdots$phenyl and phenyl$\cdots$OC interactions.

For the modeling of the SDC-SDC motif (Figure 5.4.1 (a)), we used diphenyl dicarbonitrile (DDC) and quadriphenyl dicarbonitrile (QDC) to reduce computation time. Imposing the 2D character of the motif by forcing all N atoms to stay within one plane, we obtain a relaxed binding energy of 220 meV which appears for the perpendicular configuration. The equilibrium distance between the binding N atom and the nearest H atoms is close to 2.4 Å. From the geometric proximity one might suspect a bifurcated hydrogen bond as the origin of the attraction, but as we will show in an upcoming publication the interaction is a non-local one, originating from the full phenyl rings involved. The tilting of the phenyl rings (-15 meV) as well as a planarization of the molecules (+10 meV) results in only little differences with the relaxed configuration. Contrary, for the relative position as defined by the commensurate substrate registry the binding energy decreases significantly down to 185 meV, which is therefore termed a β-bond.

In a second step, the pair formation in the pure DOA-DOA bonding motif is investigated (Figure 5.4.1 (b)). After full relaxation, the DOA molecules

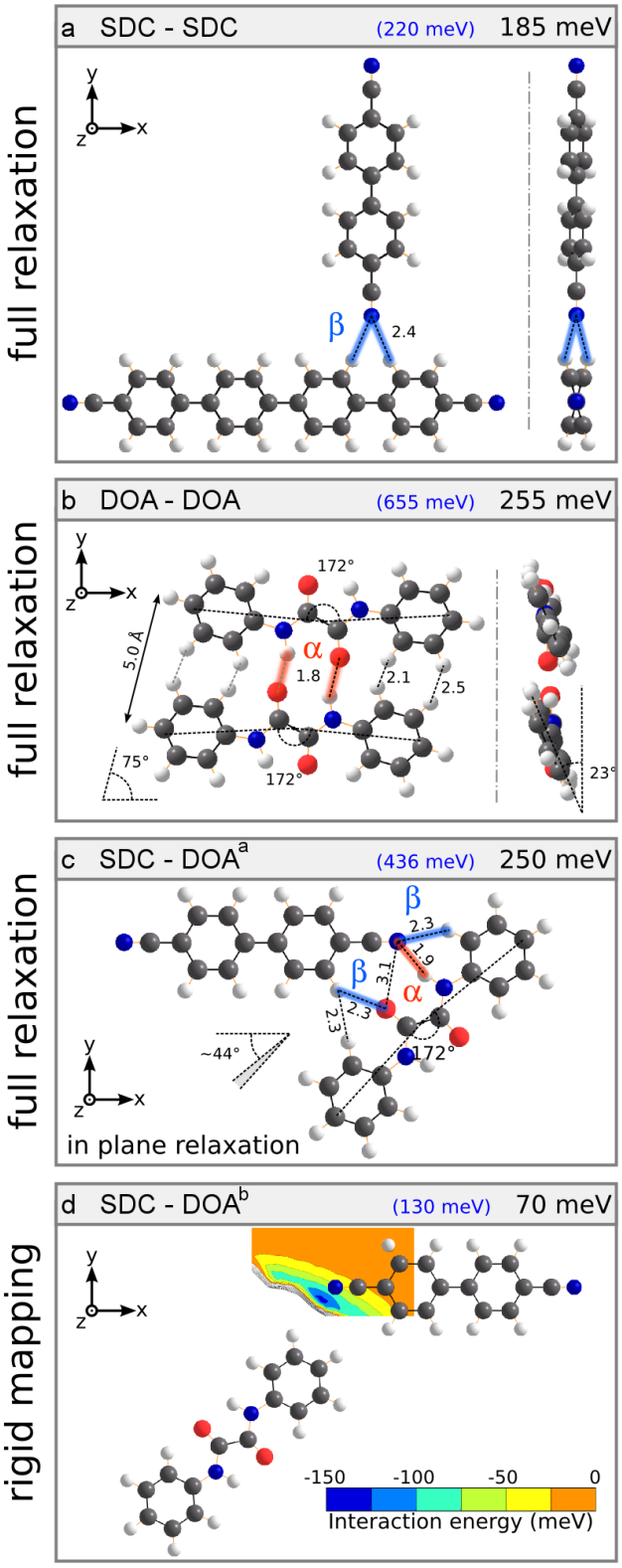

Figure 5.4.1: Computed geometries and energies of all observed bonding motifs, as presented in Figure 5.2.1 (d). Values of energy in blue and brackets are the minimum energy, whereas the normal ones are those applicable in the experimental conditions, taking into account the influence of the substrate periodicity. SDC are replaced by QDC and DDC for computational reasons. Inter-atomic distances are given in Å, and angles in degree. (a) SDC-SDC; atomic coordinates are fully relaxed, except for N atoms which are maintained in the (xy) plane. (b) SDC-DOA[a]; atomic coordinates are relaxed in the (xy) plane. (c) DOA-DOA; atomic coordinates are fully relaxed, except for the amide groups which are maintained in the (xy) plane. (d) SDC-DOA[b]; Energy map obtained by rigidly displacing the DDC molecule around the experimentally observed position.

exhibit a notable bending, and a tilting of the phenyl rings occurs, which was already proposed in a previous work [68]. Two CO···HN H-bonds (α) are responsible for a binding energy of the pair, leading to a binding energy of 655 meV in the equilibrium position. However, in the experiment this arrangement is not observed exclusively. Rather, pairs of DOA are formed with every pair being displaced notably. This finding is attributed to the substrate periodicity, since the distance between DOA molecules within a pair is increased by $\sim$ 1Å and the position of the DOA pairs follows the surface periodicity and the whole arrangement is therefore commensurate with the substrate. Again, by restricting the molecule geometry to the more complex experimental arrangement, we find that the molecules should be in fact flat and the inter-atomic distances are much larger than in the fully relaxed scenario. In the relative position after self-assembly the binding energy is strongly decreases to 255 meV, including a cooperative effect due to the periodic formation of molecular lines.

Next, we studied the SDC-DOA$^{\alpha}$ bonding motif, which for simplicity was reduced to DDC-DOA$^{\alpha}$ in the computations (Figure 5.4.1 (c)). By calculating the interaction energy mapping (not shown) only one preferred bonding site emerges. By full in-plane relaxation a bonding energy of 436 meV is determined, yielding a relative angle of 44° between the two molecules, along with a bending of the DOA molecule, similar to that observed in the DOA-DOA bonding motif. By further considering the different inter atomic distances, the presence of the 3 major interactions is revealed. Contributions to the bond were evaluated to be around 50% contribution for the CN···HN bond, 30% for the CN···phenyl interaction and 20% of the phenyl···OC interaction. Upon restricting the molecules relative positions to those determined from experiments, there is a strong reduction of the total binding energy, reducing the total binding energy from 436 meV to 250 meV. This result does not explain the hierarchic formation observed experimentally, due to the similar binding energy found for the DOA-DOA binding motif. However, the strong decrease in binding energy for DOA pairs induced by the geometric restraints already makes clear why the DOA-DOA interaction is not dominating.

Finally, the SDC-DOA^b interaction is investigated only via the map of the respective energy (Figure 5.4.1 (d)), coming to 130 meV at its minimum. Again, the experimentally observed configuration (as used in Figure 5.4.1 (d)) leads to a lowering of interaction energy down to 70 meV. However, this contribution alone is not the enough to justify the dominant expression of the SDC-DOA^a bonding motif found in the experiment.

With the interactions between individual molecules probed, we present a second row of calculations for each of the SDC-DOA bonding motifs (Figure 5.4.2), focusing simultaneously on the impact of the cooperative effect and on the effect of the size of the molecules (namely by using SDC instead of DDC and QDC). Note that the periodic boundary conditions in our calculations make the computed chains and networks effectively infinite in the (xy) plane. First, we find that the SDC-DOA^a energy (Figure 5.4.2 (a)) exceeds that of the DDC-DOA^a by 15 meV, similar to the findings for the SDC-SDC interaction discussed earlier. Then, by comparing the total bonding energy of a SDC-DOA chain (Bond N°1 + Bond N°2) to the single SDC-DOA^a bond (2 × Bond N°1), we evaluate the cooperative effect to be 60 meV, *i.e.* 30 meV per bond, increasing the bonding energy to 295 meV. Again, we notice a slight discrepancy between the minimum energy position of the binding and the lattice periodicity. Nevertheless, the global bonding energy in the experimental separation is overall 295 meV. This makes the SDC-DOA^a bond effectively the strongest of the possible combinations, explaining the preferential formation for SDC-DOA chains over other networks, and consequently the hierarchic formation.

A similar approach is used for the SDC-DOA^b bonding motif (Figure 5.4.2 (b)), with this time a complete mapping of the lateral interaction between SDC-DOA chains. The global bonding energy in the experimental conditions is found to be 60 meV, *i.e.* very close to the value given by our simple model of Figure 5.4.1 (d). There seems to be almost no cooperative effect, and the replacement of the DDC by a SDC does not significantly alter the situation. The map of the interaction energy is however very instructive, as it reveals the frustration of the experimental configuration, forced by the

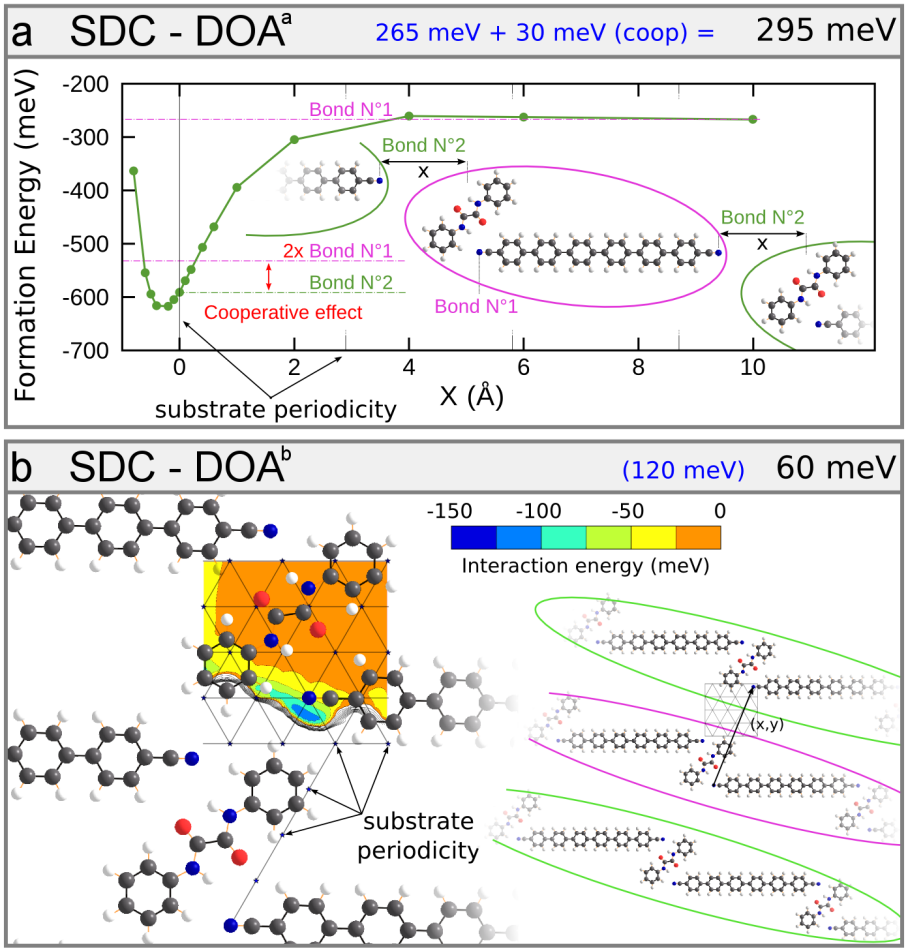

Figure 5.4.2: Computation of the cooperative effect on SDC-DOA interactions. (a) SDC-DOA^{a}; Energy curve obtained by rigidly displacing the SDC-DOA pairs with respect to one another. X(Å) is thereby the displacement between the nitrogen atom of 6DC towards the hydrogen atom of the top functional group of DOA forming the stronger α bond. When two SDC molecules are bonded to one DOA molecule (in the observed configuration), a total cooperative energy of 60 meV is obtained. (b) SDC-DOA^{b}; Energy map obtained by rigidly displacing the SDC-DOA chains with respect to one another. The cooperative effect is minimal. The difference in energy manly arises from the change of molecule from 2DC to SDC

substrate periodicity, despite a complex energy landscape of the laterally interacting SDC-DOA chains.

5.5 Conclusion

To conclude, we investigated the hierarchic self-assembly of bi-component organic molecular networks constructed with SDC and DOA. Further, the mechanisms driving the emergence of the distinct network types, formed at different stoichiometric ratios, was analyzed. In this manner the exact geometry and alignment of all formed phases could be understood thoroughly. The preferred formation of SDC-DOA chains found in the experiment could be rationalized through theoretically investigating the different binding properties of each individual nodal motif observed. The geometry of the networks is dictated by the interplay between the energetic hierarchy of the different binding motifs and the requirement of commensurate superstructures. Therefore, by using hierarchic construction principles we demonstrated supramolecular architectures which are tunable by the stoichiometry of the two organic constituents. The presented model system is highly versatile as the pore size in the networks can easily be tuned via the relative amounts of the constituents provided during growth. In a further step we could recently show that the hierarchic networks presented here can be used to guide the thermally activated diffusion of SDC spacer molecules (in the 2:1 phase) in one dimension along the more stable SDC-DOA lines [129]. Due to the universal nature of hierarchic organization protocols, the concepts of our work can be adapted for a large variety of nanoarchitectures. For example, hierarchic protocols similar to the one presented can be expanded to different substrates or increasing emphasis can be put on realizing network functionalization such as the integration of molecular switches via suitably designed molecular building blocks.

Chapter 6

Electron Confinement in 2D Molecular Architectures

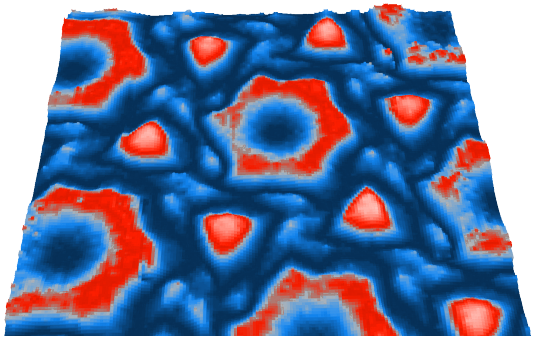

Beyond investigating the topography of surfaces and adsorbates positioned on them, the STM can be used to probe the local density of states with atomic precision. Thereby, it is possible to characterize bulk material systems and their interfaces [11, 130, 131] or identify and investigate molecular electronic states [9, 132, 133, 134]. Furthermore, by determining the lateral changes in the LDOS, detailed two dimensional maps of the surface charge carrier density and its spatial variation can be acquired. The surface electronic properties can differ drastically from the behavior found for the identical bulk material. A prototype system is the formation of a quasi-free 2D electron gas on Ag(111) (see Chapter 2.2.1). When scatterers are deposited and positioned on the Ag(111) surface, it is possible to confine the quasi-free electrons to lower dimensions, as was first demonstrated by Crommie *et al.* [39] for Fe atoms being arranged in such a fashion that quantum corrals evolve on Cu(111). Later similar experiments

were carried out on Ag(111) [135], where the scattering on step edges and therefore standing wave patterns were evidenced [42, 136, 137], finally evidencing quantum confinement in small islands of Ag epitactically grown on Ag(111) [38].

Molecules acting as scattering barriers for surface electrons were already briefly introduced earlier. However, in networks where molecules segment the surface into one- or zero-dimensional partitions, electrons are not only scattered by the molecular boundaries but rather confined within these structures [40, 41, 72]. When the confined areas are on the same size scale as the wavelength of the surface electrons, well-defined electronic states evolve within the boundaries. This presents the possibility to use molecular nanostructures to reduce the confinement dimensionality subsequently from 2D, for the free surface electrons on Ag(111), down to 0D when closed pores are considered.

In this chapter, the confinement of surface state electrons on the Ag(111) substrate within nanoarchitectures self-assembled from sexiphenyl dicarbonitrile and N,N' diphenyl oxalic amide along with theoretical modeling for the observed confined states is discussed. Further, a comparative study of the LDOS measurements by constant current dI/dV mapping and open feedback loop point spectroscopy mapping will be presented and discussed. All subsequent color coded intensity plots are displayed in the color code presented below. Dark and light blue corresponds to low spectral intensity, violet and dark red to intermediate intensity, whereas orange and yellow indicates high intensity. The displayed intensity plots are displayed with similar value ranges for the intensity.

All samples were prepared according to deposition temperatures and procedures outlined in the previous chapters. $^{dI}/_{dV}$ signals were recorded with bias modulation at ∼1400 Hz at a modulation amplitude of 5 mV rms, while the lock-in time constant was set to 20-50 ms.

Parts of the results in this chapter were published in References [40] (reprinted with permission, copyright 2009 American Chemical Society) and [41] (copyright 2011 by The American Physical Society).

6.1 1D Confinement in N,N'-Diphenyl Oxalic Amide Nanogratings

In a first step, to reduce the dimensionality of the surface state electrons, the confinement between nanowires assembled from N,N' diphenyl oxalic amide is investigated briefly. The assembly mechanisms and their ordering was already discussed in Chapter 4. The effect of electrons being confined within 1D architectures, leading to the expression of standing waves, which can be described similar to Fabry-Perot interferometers, was already studied in great detail in other experiments [72, 137]. Therefore, no in detail study of the confined states between the nanogratings is presented. Rather the influence of Co adsorbates positioned on top of the molecules on the scattering and thereby confining properties of the molecules is discussed.

In Figure 6.1.1 a series of spectra taken along a line as indicated between the molecular boundaries of the cavity is displayed. When selected positions within the cavity are examined in more detail (Figure 6.1.1 (b)), the center of the cavity (blue) shows only one clear peak that is centered around 0 mV in the energy range under consideration. At positions further away from the center, a continuous decrease in intensity for this first bound state is found along with an increase of the intensity of the second eigenstate centered around 150 mV. This second state shows a depression in the center, which means that a node in the standing electron wave confined in the cavity is expressed.

When all spectra taken along the line are displayed as a 2D color plot (Figure 6.1.1 (c)) the spatial and energetic distribution within the cavity can be clearly resolved. Further the onset of the third bound state close to 400 mV is evident, which should show three intensity maxima along with two nodes. However, this state lies outside the energy range that was investigated. Further a strong increase in intensity is found close to and on the molecular boundaries (black and magenta data points in Figure 6.1.1). In these positions, a steady increase in electron density is evident onto which the second and third excited state within the cavity are super-

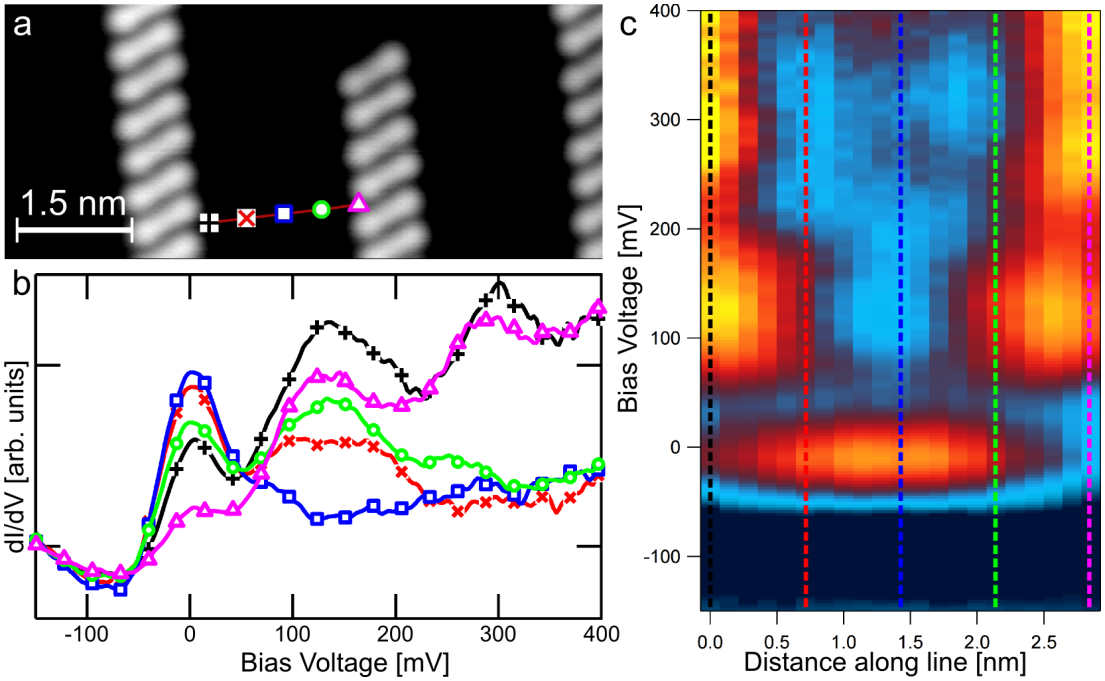

Figure 6.1.1: (a) High resolution topography measurement of N,N' diphenyl oxalic amide nanogratings. The line between the gratings along with selected positions indicated by colored markers show the path along which spectroscopy measurements were performed. The spacing between the molecular lines is approximately 2.2 nm (I_T = 0.11 nA, V_B = −0.29 V). (b) Individual point spectra as indicated by the appropriate colors and markers in (a). A clear maximum in the LDOS around 0 mV can be associated with the first confined electron state in the cavity. The intensity of the lowest state reduces further away from the center (blue), where in turn the second confined mode around 150 mV is evident: due to symmetry no increased intensity is observed in the center. (c) Color plot of all 20 spectra taken along the line. The selected positions are indicated by colored dashed lines, respectively. At the highest investigated energies (400 mV), the onset of the third confined state in the cavity is observed by a slight increase in intensity in the center of the cavity.

imposed with increased intensity that is broadened across a wide energy range. Therefore, it can be assumed that with increasing energy, the penetration of the standing electron wave into the cavity rim also increases. This is expected since the energy continuously approaches the height of the scattering barrier and therefore tunneling of electrons into and finally

across the molecules will set in.

To study the effect of Co adsorbates positioned on the template (also see Chapter 4) on the confinement within the cavity, several lines were recorded in parallel to the DOA chains at similar distances from the molecules, see Figure 6.1.2. The distance from the molecular rim was chosen similar to the positions red and green in Figure 6.1.1. When no Co adsorbates are present, see Figure 6.1.2 (a&b), two distinct increases in intensity at $\sim \pm 40$ mV are observed, followed by a spatially modulated scattering pattern between 100 and 220 mV. At higher energies, a broad maximum with homogeneous spatial distribution appears.

When a single Co atom or two Co atoms are positioned on the phenyl ring of the molecule on either side of the grating, however, the scattering pattern observed is far more complex. Reduced intensity close to the Co position and associated with this a shift to higher energy of the lowest lying states is found to occur, see Figure 6.1.2 (c&d). At energies above 100 mV, a reduced total intensity along with a complex fine structure is present. Whereas the fine structure can be expected to depend strongly on the distance of the respective next molecular boundary and the exact geometry, the reduced intensity clearly points to an increase of the scattering barrier height. This is in agreement with theoretical predictions of a dipole moment induced upon adsorption of Co onto the phenyl moiety according to [75, 76]. Since no DOA line is situated opposite to the single Co atom, the observed complex scattering pattern must be attributed to the different superposition of standing waves. For the double Co case, see Figure 6.1.2 (e&f), only up to the Co atoms a neighboring DOA line is present, which in turn also explains the disparity between the fine structure on either side of the adsorbates at increased energy. In this case also a decrease in the LDOS correlated to the Co adsorbate is found along with reduced intensity at energies exceeding 300 mV.

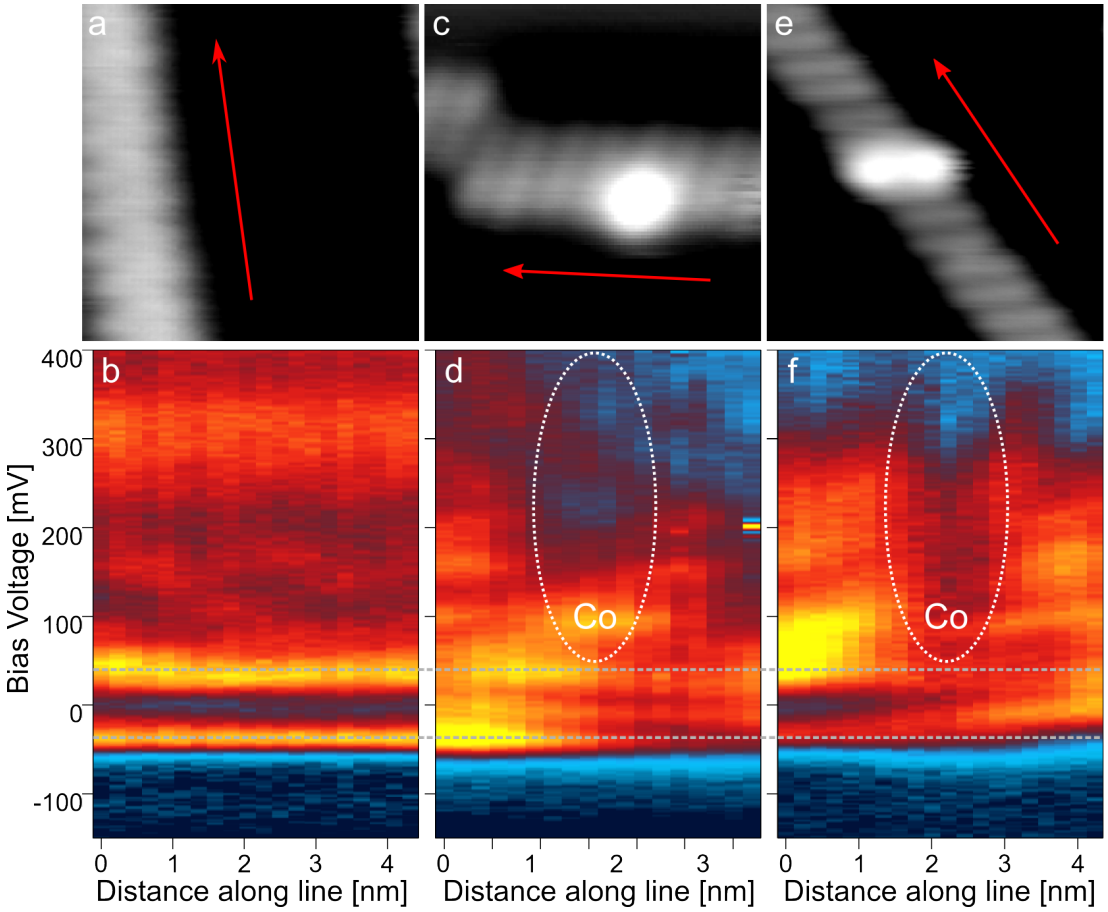

Figure 6.1.2: (a&b) Line of spectra recorded in parallel to a DOA grating. At this distance from the nanograting (similar to the red and green positions in Figure 6.1.1) two distinct increases in intensity at ∼ ±40 mV are observed. (c&d) A more complex scattering behavior appears, when a single Co atom is adsorbed on top of one of the adjacent phenyl rings. At higher energies (marked area), a reduced spectral intensity is found. (e&f) When both phenyl rings are occupied, a clear depression close to the Co position (marked are in f) is observed. The decrease in spectral intensity points to an increased, local scattering potential due to the Co adsorbates.

6.2 0D Confinement within Sexiphenyl Dicarbonitrile Networks

Two-dimensional molecular nanostructures formed via self-assembly, providing open pores represent fundamental architectures that can potentially be functionalized in further steps. Therefore, in recent years networks and films formed from Para-Sexiphenyl Dicarbonitrile (which were already introduced in the previous chapter) have been thoroughly investigated in our group [40, 41, 82, 83, 96, 106, 138, 139].

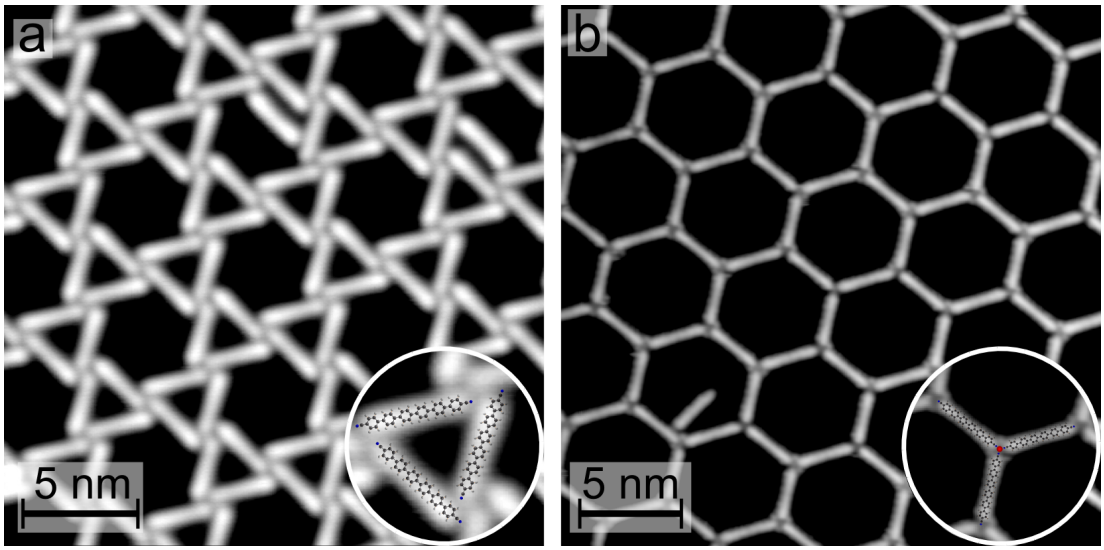

Figure 6.2.1: Two examples for open-porous networks formed by self-assembly of SDC on Ag(111): (a) Kagomé phase for pure organic networks ($I = 0.1$ nA, $V_b = -0.5$ V) (b) Metal-organic honeycomb networks evolve in the presence of Co atoms ($I = 0.15$ nA, $V_b = 0.95$ V) Structure models of SDC are superimposed in both cases onto a zoomed inset in the bottom right corner, illustrating the binding geometry.

It was found that the molecules self-assemble on Ag(111) (after deposition onto the sample held at room temperature) into various geometries, depending on the total coverage. The organic networks share a common 4-fold symmetric binding motif [106], where one possible open-porous arrangement is the so called Kagomé network, see Figure 6.2.1 (a). This spe-

cific network features pores of different size within a single domain along with a complex geometry, while the network is commensurate with the substrate.

Following atomic cobalt exposure during growth, a three-fold metal-coordination binding motif leads to the formation of a network of hexagonal pores, see Figure 6.2.1 (b). The honeycomb-like lattice is of high, crystal-like quality in two dimensions, facilitated by the arrangement being commensurate with the underlying Ag(111) lattice [82]. Large, defect-free domains are formed that are stable up to room temperature and can further be functionalized to confine the rotational motion of caged supramolecules [96]. The confinement of surface electrons within the pores of these networks down to zero dimensions and the pertaining bound states will be discussed in the following.

6.2.1 Kagomé Lattice

The Kagomé lattice features two different pore sizes in the unit cell of the network. The central pore has a van der Waals diameter of approximately 3.2 nm. Therefore, similar energy ranges as for the 1D confinement between DOA nanogratings with comparable distances presented earlier can be expected.

In Figure 6.2.2, a series of spectra was recorded traversing both, the smaller, triangular outer pore and the bigger quasi-hexagonal pore in the center. In the center of the inner pore (6.2.2 (b), blue), a strong intensity increase indicating the lowest bound state at ~ -5 mV is found. Further away from the center (6.2.2 (b), red and green), the peak is reproduced at lower intensity, which is in accordance with the expected highest intensity in the center due to symmetry. A second maximum, centered around ~ 80 mV, at the edge of the inner pore (red and green) indicates the second bound state, which exhibits no intensity in the center. Furthermore, at $\sim$280 mV, maxima are found in all three positions, consistent with the expected distribution for the third bound state. Due to the smaller confined area in the outer pores (6.2.2 (b), black and magenta), the first bound state

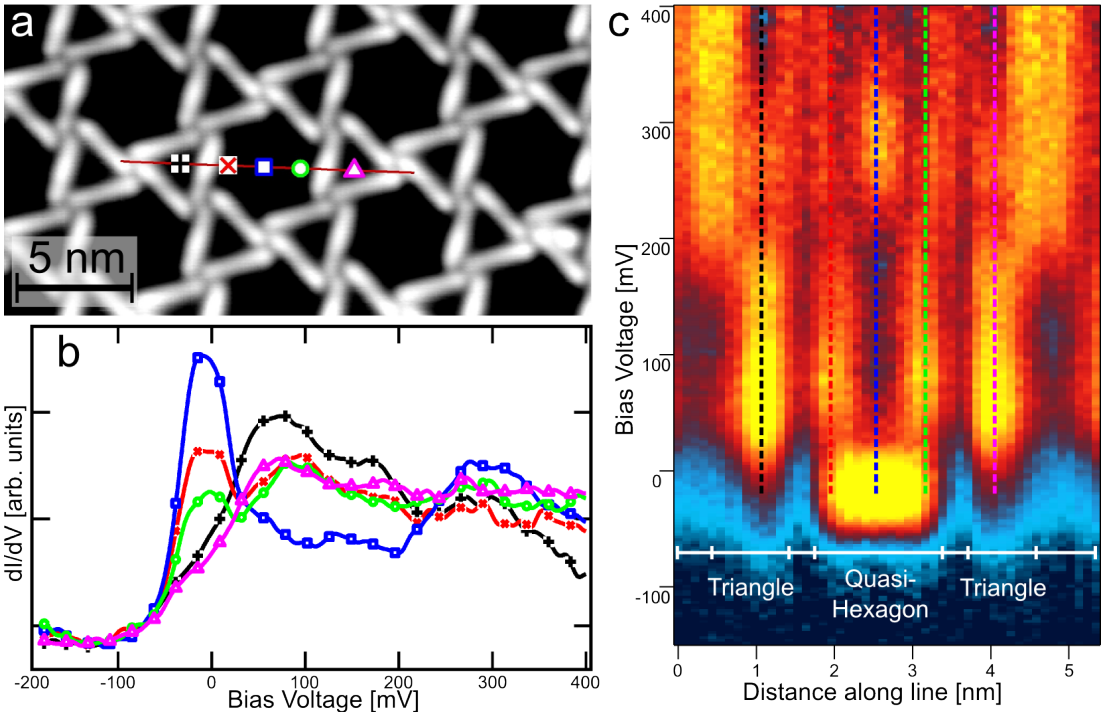

Figure 6.2.2: Spectroscopy within the Kagomé Pores.

is shifted upwards in energy with respect to the central pore to ~ 75 mV, which is close to the second excited state of the inner pore. The difference in intensity at the black and magenta positions is attributed to the different orientation and therefore positions of the spectra taken within the triangle.

When all spectra recorded along the line displayed in Figure 6.2.2 (c) are plotted in a color plot corresponding to spectral intensity, the spectral distribution of the observed bound states can be understood more easily. The first bound state in the central pore is broadened over an energy range from -50 up to 25 mV. The second state, a distinct two-peak structure, spans the energy interval between 50 and 200 mV, until a threefold structure corresponding to the third confined state is present for higher energies. In the triangular pores the intensity maximum spans the energy interval between -25 and 225 mV. The first bound state thereby spans an energy interval that is larger by a factor of 2.5 than that for the central pore. Before and after the energy interval between 225 and 325 mV, a slight depression is

observed. This indicates the second bound state. However, since no clear minimum is observed, the second bound state can be expected to feature no depression in the center, but rather a more complex spatial distribution of the LDOS. Finally, close to maximum energy (starting at 350 mV), a depression in intensity occurs, indicating the onset of the third bound state with lower intensity in the center of the pore.

At positions corresponding to the center of the molecules low intensity is found for energies below 200 mV. However, at higher energies, intensity similar to within the pores indicates increased tunneling into and across the molecules and binding motifs. This effect will be discussed in more detail in Section 6.3.

The observed spatial distribution and scaling effects depend strongly on pore size. In order to characterize the spatial distribution of surface electrons within the pores in full detail, a series of open-feedback loop point spectra on a 2D grid (84x84 point spectra, energy interval -200 mV to +400 mV, data point spacing 25 mV) were recorded. When the intensity of the individual spectra at a given energy is then displayed as a 2D color plot, the spatial distribution of the confined surface electrons can be visualized. To enable a thorough intensity comparison, all spectra were normalized to a value of 1 in the flat part of the LDOS below the onset of the 2D surface state (-200 to -100 mV). Maps extracted at selected energies are displayed in Figure 6.2.3. The same color code as in Figure 6.2.2 was used and all maps are displayed with the same color range. A semi-transparent topography scan recorded simultaneously, indicating the molecules positions, is superimposed onto the spectral maps for clarity.

At zero bias, a dome shaped feature in the central pore with high intensity is found alongside with low intensity in the smaller triangular pores (see Figure 6.2.3 (a)). As already observed in the spectra in Figure 6.2.2, the onset of the first confined state in the smaller pores is shifted to higher energies. Therefore, at 0 mV a maximum is found for the bound state in the central, quasi-hexagonal pore, whereas only low intensity displays in the smaller triangular pores. Even lower intensity is found at the molecule positions.

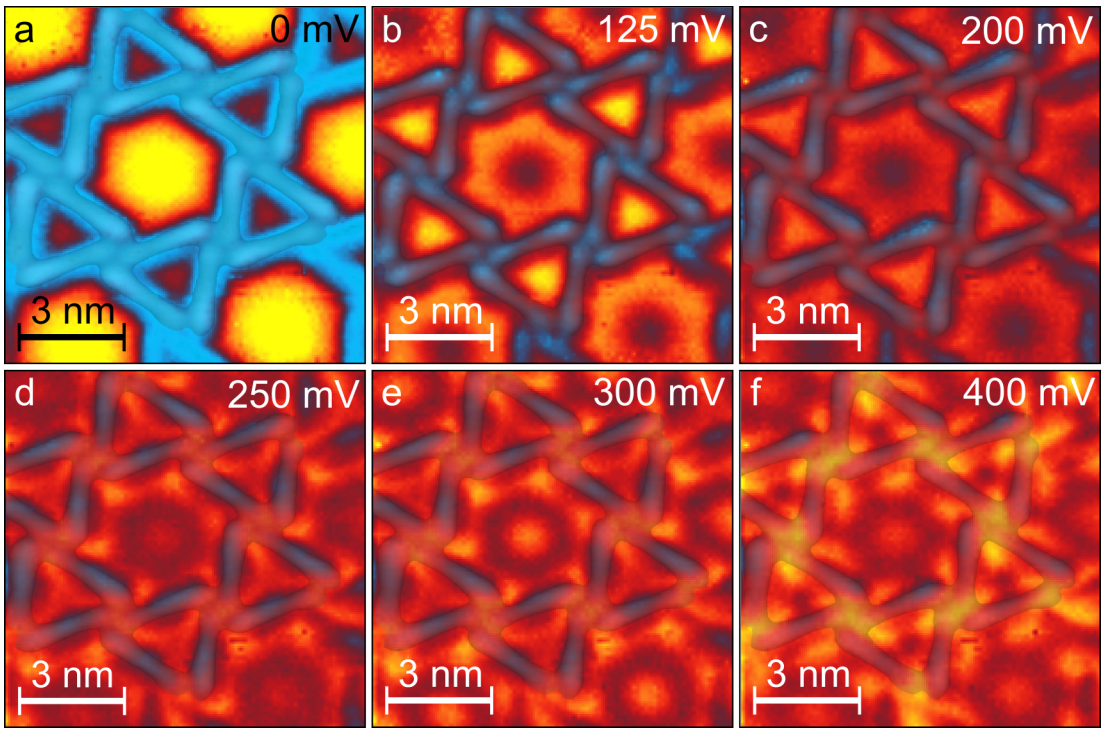

Figure 6.2.3: Spectroscopy maps showing the nanoscale confinement of surface electrons within the network pores. A transparent topography measurement of the molecule positions is superimposed onto all maps for clarity. (a) At 0 mV a dome shaped pattern in the central pore shows the first confined state, whereas only low intensity indicates the onset of the first state in the triangular pores. (b) Maximum intensity within the triangular pores is found for the first state in the triangular and a depression in the center of the quasi-hexagonal pore for the second bound state, respectively. (c-e) In the triangular pore the evolution into the third confined state is observed featuring a sombrero shape with higher intensity in the corners of the quasi-hexagonal rim. For the triangular pores the first state evolves into an intermediate trigonal geometry alongside with increasing intensity at the molecular binding motif in opposition to low intensity along the molecular backbone. (f) At the highest investigated energy the triangular pores feature a depression in the center and strong intensity in the corners. In the quasi-hexagonal pore stronger intensity is found localized in the corners of the pore, whereas the central maximum reduces in intensity.

Close to 100 mV, the second bound state in the central pore is evident, compare Figure 6.2.3 (b). A depression in the center combined with high intensity at intermediate distance between the center and the rim of the quasi-hexagon, indicates the expected torus shape for the second confined state. This coincides with the energy range following the maximum of the first bound state in the smaller triangular pores. Since the first bound state in the smaller pores is broadened over a large energy interval, it can be observed alongside both, the first and second bound state in the quasi-hexagonal pore.

At intermediate energies between 200 mV and 300 mV, the continuous evolution of the torus shape into a sombrero shape in the quasi-hexagonal pore is observed. The third confined state then features two maxima separated by a minimum. Towards the rim of the central cavity, a more complex distribution of confined electrons is found, where a higher intensity is found in the corners of the quasi-hexagon, following the outline of the molecular boundary. For the triangular pores a transition from the first triangular shaped bound state with a maximum in the center towards an intermediate state featuring a threefold geometry occurs. This transition coincides with increasing intensity at the positions of the 4-fold molecular binding motif. In contrast the molecular backbones retain low intensity, pointing towards only low tunneling into and through these positions. This also rationalizes the higher intensity found in the corners of the central quasi-hexagon, where a stronger coupling between pores leads to higher intensity.

At the highest investigated energy of 400 mV, the intensity of the central maximum of the quasi-hexagonal pore has declined, whereas higher intensity is found towards the corners and also alongside the molecular backbones. In the triangular pores the second confined state, featuring a depression in the center of the trigonal intermediate state with high intensity in the corners, is reached. High intensity is now found in the center of the binding motif, along with an overall increased intensity along the molecular ligands. This indicates that at 400 mV strong tunneling through the ligands and the functional groups of the molecules is possible. Therefore, the carrier energy is similar to the height of the scattering potential

imposed by the molecules. Thus, coupling between the different pores can be expected.

In a final step, the confinement properties of the molecular network were investigated via a boundary element method (BEM) simulation, which was already briefly introduced in Chapter 2.2.1. In these simulations, the Schrödinger equation is solved for a planar surface, which is segmented into regions of homogeneous, constant potential separated by areas of higher potential with a width of 0.25 nm and a length of 2.9 nm representing the molecules. These potentials are arranged in a fashion to reproduce the Kagomé lattice observed in the experiment and the barrier height was chosen as $V = 500$ meV with respect to the remaining area. For the surface state the effective electron mass $m^* = 0.42m_e$ (m_e is the free electron mass) and an onset energy of 65 meV was chosen as these are experimentally well established [37, 136, 140]. Further an energy-independent broadening of 25 meV was introduced for all electronic states to account for the energy width of the confined surface states. Conductance maps (LDOS(x, y)) were then calculated at the energies where distinct bound states exist, as discussed above.

The simulated conductance maps at -5 meV, 127 meV, 293 meV and 415 meV are reproduced in Figure 6.2.4 (a-d). For clarity, the experimental dI/dV maps extracted at similar energies are again displayed alongside the simulated maps (Figure 6.2.4 (e-h)). All maps are displayed using the same color code, which enables a direct comparison of the relative intensity in both simulated and experimental data.

Overall, simulated and experimental data show excellent agreement in both shape and intensity of the investigated features. At the maximum of the first confined state in the quasi-hexagonal pore (Figure 6.2.4 (a&e)), both theory and experiment feature a dome shaped feature. In the experiment, the outline of the dome follows the outline of the pore rim more closely than in theory. Furthermore, the onset of the first confined state in the triangular pore is not as pronounced in the simulations as it is in the experiment at this energy. Only a very slight increase in intensity can be observed. However, the low intensity in the triangular pore can also be

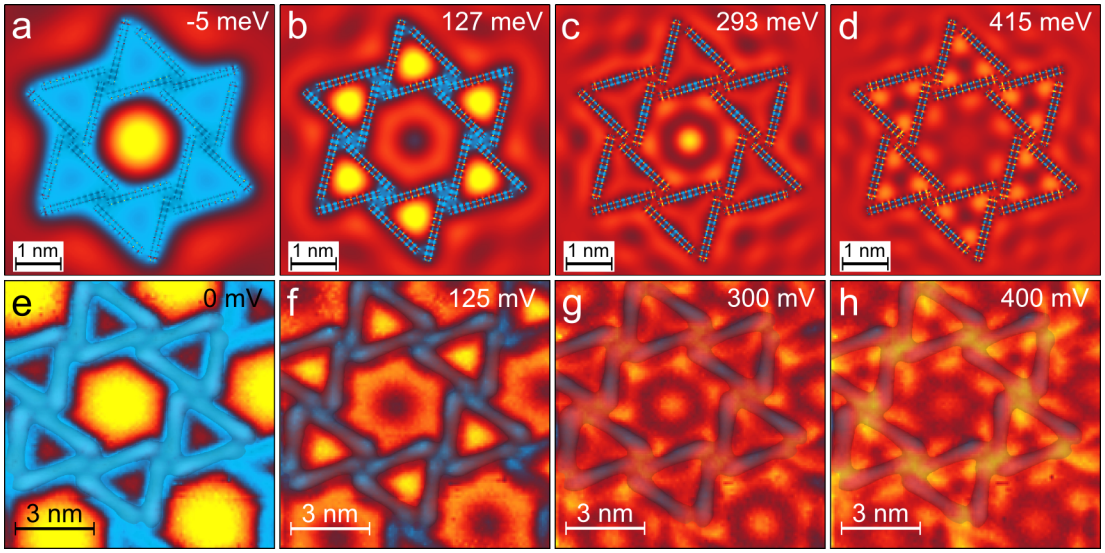

Figure 6.2.4: (a-d) BEM simulations of the confined states in the pores of the molecular network. In the simulations the molecules are represented as rectangular potential barriers of a constant height of 500 meV. (e-h) *dI/dV* maps acquired at similar energies as in the simulations. Overall simulation and experiment show good agreement. The simulation reproduces experimental findings regarding relative intensities and fine structure of the confined states in remarkable detail.

attributed to the slightly lower energy at which the LDOS map was calculated. Nevertheless, this is sill overall a good agreement with the intensity observed in the point spectra (see Figure 6.2.2 (b), black and magenta), since only the onset of the first bound state in the smaller pore is reached at -5 mV.

When the first bound state in the triangular pore is reached, the overall relative intensity of experiment and theory is in good agreement. The torus shaped state in the center is reproduced at lower intensity compared to the outer pore in both cases. In the simulation, the state in the quasi-hexagon again features rather a pure hexagonal geometry, whereas a more pronounced emphasis is observed in the experiment towards the molecular boundaries. The low intensity at the binding motif and slight penetration at the center of the molecule backbone is present in both experiment and

theory.

At 300 meV, where the third, sombrero shaped confined state appears in the central pore, again also in the simulation, the shape and intensity is reproduced in great detail. High intensity in center and an outer ring modulated corresponding to the molecule rim is observed in both cases in good agreement. The intermediate trigonal bound state in the triangular pore is also reproduced in both spatial distribution and magnitude relative to the central pore. An enhanced intensity at the binding motif along with low intensity at the center of the molecules forming the quasi-hexagonal pore is observed in both cases. The same holds true at the highest investigated energy, where the trigonal confined state with a depression in the center is found in the triangular pores.

In the quasi-hexagonal pore, the center now also exhibits a significantly lower intensity compared to the six outer lobes. However, the features observed in the corners of the quasi-hexagon do not reproduce entirely in the simulation as they appear more elongated in the experiment. Furthermore, the high intensity localized at the 4-fold binding motif sites as observed in the experiment is absent in the simulation. This observation points towards a non-homogeneous scattering potential along the molecules and further rationalizes the slightly different spatial distributions of the lobes along the pore rim. Therefore, to reproduce the experiment in full detail at higher energies, a more sophisticated approach, in which a non-constant scattering potential along the molecules is employed, would be required.

6.2.2 Honeycomb Lattice

Similar to the Kagomé lattice discussed above, the confinement of surface electrons within the pores of the honeycomb lattice formed via metal-coordination of SDC to cobalt atoms was investigated by spectroscopy mapping. In a first step, the energetic and spatial distribution of the confined states was investigated by recording numerous spectra situated on lines. Here special emphasis is put on the difference between the metal-coordination bond and molecular backbone, as a non-trivial scattering behavior was already observed in the organic Kagomé networks. Therefore, spectra taken on a line across the hexagonal pore along two different paths are compared. Path I is chosen between the central positions on the molecules, whereas path II spans over the pore from one metal-coordination bond to the other (see insets in Figure 6.2.5 (a&c)).

In Figure 6.2.5 (a&c) spectra taken at specific sites within the pore (see inset in both cases) are displayed. For the center of the pore (green), two peaks at -10 mV and 210 mV, respectively, are found. With respect to the center of the Kagomé pore, this means that the onset of the first and all subsequent bound states is shifted to lower energies.

At positions halfway between the center and the rim of the pore (blue and magenta for both paths), first, two peaks are observed. The lower energy corresponds to the first state that is also found in the center, but at reduced intensity, whereas the second peak coincides with a minimum at the central position at 75 mV. As for the Kagomé network, the second state features a torus geometry with a depression in the center and a maximum halfway between the center and the edge. The slightly different relative intensities along the two paths in 6.2.5 (a&c) are only due to the slightly different distance from the pore center at which the spectra were taken. The light blue spectrum was taken in both cases very close to the network rim. While both show a shoulder coinciding with the first bound state as the previously discussed spectra, the second peak only along path I in 6.2.5 (a) coincides with the second confined state in the pore. Close to the Co site on path II (6.2.5 (c)) a peak at intermediate energy between the first and

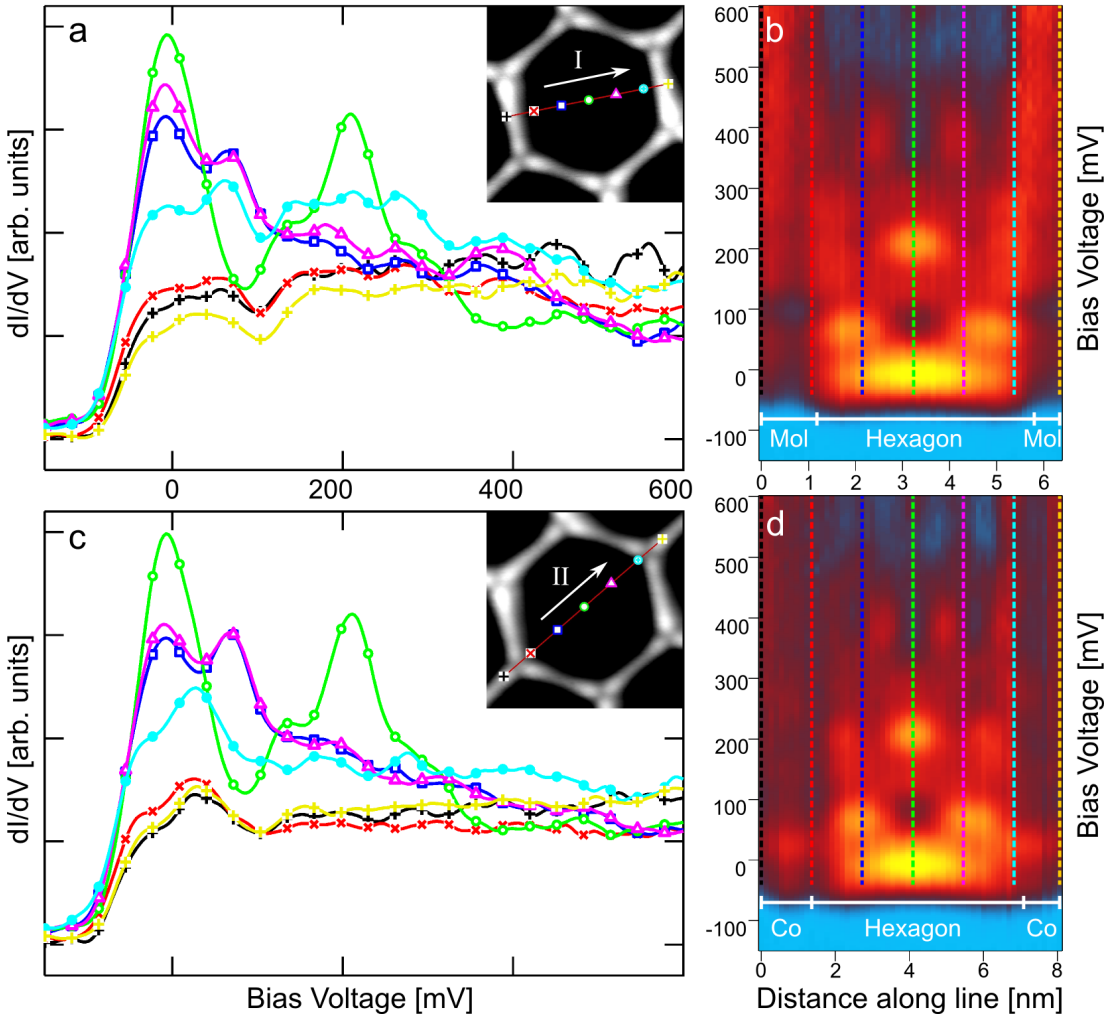

Figure 6.2.5: Spectroscopy within the Honeycomb Pores. (a&c) Point spectra at selected positions within the hexagonal pore and on the surrounding molecules. A discrepancy in the scattering properties of the metal-ligand bonds and the molecular backbones is observed (light blue curve), whereas other features are consistent along both directions. (b&d) Color plot of spectral density along the given lines. Characteristic points are labeled with the same colors respectively as for the point spectra. Close to the red and light blue position the different spectral distribution and intensity are distinctive.

second state at 45 mV is found. Therefore the scattering behavior of the molecule backbone and the Co sites can be assumed to be different even at relatively low energies. Spectra taken on the molecules (black, red and

yellow) show similar behavior to the positions just inside the cavity (light blue) along both paths. Generally, a lower intensity compared to features in the pore is observed on top of the molecules. Towards the end of the investigated energy range, the intensity on the molecules and in the pore reaches similar levels.

In a next step, the spatial and energetic distribution of both line-traces are compared in a color plot, see Figure 6.2.5 (b&d). Please note that due to drift during the measurements of the lines of point spectra, the light blue spectra are taken slightly within the cavity, accounting the differences at nominally identical positions, as already pointed out for the point spectra extracted for the previous analysis. To serve as a better guide to the eyes, the nominal positions of the spectra are indicated by respectively colored dashed lines along with section markers for the hexagonal pore and the molecule backbones (path I) or Co sites (path II).

The hexagonal cavity shows four distinct bound electron states confined within. The first bound state, showing a single feature, is situated at -5 mV and extends approximately over the energy interval between -75 and +25 mV. The state spanning across the entire cavity is followed at higher energy by a two-lobe feature with maximum intensity at 68 mV reaching up to ∼100 mV. The third bound state shows a three feature structure. However, where only a single lobe is observed at 205 mV in the center of the cavity, the two satellites show different behavior for the two directions in which the spectra were obtained. Along path I (Figure 6.2.5 (b)), side lobe is segmented into a lower energy part at 175 mV and a higher energy part at 250 mV. In contrast, the intensity of the higher energy lobe is strongly reduced close to the Co sites on path II (Figure 6.2.5 (d)), pointing to a discrepancy in the electron density along these two axis. Finally, the highest bound state, featuring four peaks, starts to appear at 350 mV, reaches maximum intensity at 400 mV and fades out at ∼450 mV. Again, a strong difference between the two directions is observed, where only the two central features are present in both cases, however close to the Co sites the intensity is again reduced and only very little intensity is present on the cavity rim itself.

The different scattering properties of the metal-coordination sites and the molecular backbones of the ligands are evident. The cavity rims along with the molecules and Co sites in both cases show distinct differences in spectral distribution and intensity at energies exceeding 120 mV. For the molecular backbones (Figure 6.2.5 (b)) high intensity is found on the molecule as well as directly in the cavity for in this energy range. No clear modulation in the intensity pattern that would point towards occupied or unoccupied molecular states is observed. At the Co-sites however, the intensity is reduced close to the bond and a slight modulation showing a maximum at 250 mV is found.

The analysis of the line spectra shows that only for energies up to 100 mV a spatially uniform quantum dot state can be expected. In an effort to investigate this more thoroughly, 2D spectral maps were obtained by recording 84x84 point spectra on a grid, for details see Section 6.2.1. Maps at selected energies close to the features observed in the previous analysis are displayed in Figure 6.2.6.

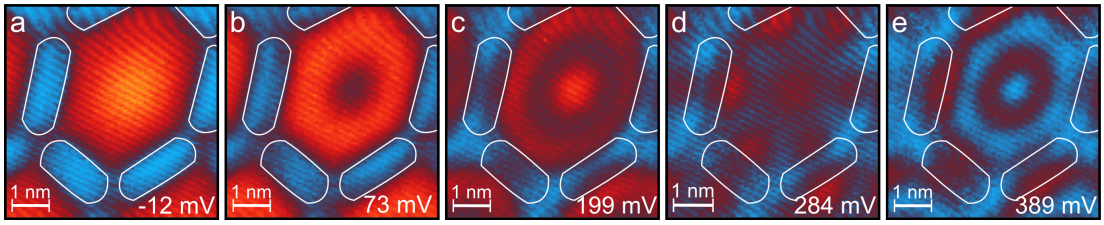

Figure 6.2.6: Spectroscopy maps showing the nanoscale confinement of surface electrons within the honeycomb network pores. At energies up to 73 mV (a&b) the spectroscopy maps reveal a uniform electron density distribution along all directions within the pore, whereas for higher energies (c-e) a strong modulation of the confined state close to the cavity rims is observed. This effect originates from the different scattering properties of molecular linkers and metal-coordination sites. For a full analysis, see [40, 139].

As already indicated by the analysis of line spectra taken across the cavity, only for energies up to 100 mV the LDOS pattern is homogeneous and no modulation related to the Co sites is observed (Figure 6.2.6 (a&b)). For energies exceeding this limit, an increasingly strong modulation of the features

towards the cavity rim sets in (Figure 6.2.6 (c-e)). As was shown by a detailed analysis in [40, 139] this is rationalized by a parametrized scattering barrier modeling. It was conclusively shown that Co centers in this network act as negative scattering potentials opposed to the positive potential nature of the molecules. This is significantly different from isolated Co atoms, which act as positive scatterers on the Ag(111) surface [141]. Therefore, by acting as attractive centers rather than repulsive ones, the scattering properties of the Co atoms are drastically changed upon the incorporation into the metal-organic network. This motivates a subsequent, thorough analysis of the scattering properties of the ligands and co-deposited atoms introduced in the previous sections.

6.3 Comparison of Scattering Properties

The confinement of surface electrons depends strongly on the properties of the molecular ligands and atoms enclosing and sectioning the surface. The energetic onset and spacing of confined states depends for infinitely high potential barriers inversely on the enclosed area. By confining carriers to smaller areas the lowest confined state will shift to more elevated energies. The distribution of higher confined states, however, depends for finite barriers heights and widths strongly on the exact potential amplitude. When electron energies approach the barrier height, effects like resonant tunneling through the barrier and increasing penetration dictate the energetic distribution of states. Since molecules and atomic adsorbates, due to their internal structure and their bonding properties to the surface and between them in networks, introduce complex scattering barriers, an analysis of the employed species discussed earlier will be presented in the following.

First, the effect of feature size is discussed briefly, see Figure 6.3.1. The smallest confinement length is found for the 1D case between DOA nanogratings. The width of the cavity in the case studied was 2.2 nm. Here, the lowest bound state is found at 0 mV (red panel in Figure 6.3.1). The second state then is situated at 125 mV.

In the case of the hexagonal pore in the Kagomé lattice, the diameter of the 0D confinement area is slightly bigger (3.2 nm) and therefore the lowest confined state is found at lower energy (-5 mV). Consequently also the second and third state are shifted to 85 mV and 250 mV, respectively (green panel in Figure 6.3.1). In the most spatially extended structure, the metal-coordinated honeycomb lattice, featuring a cavity diameter of 5.5 nm, the lowest onset energy for the bound state is observed (-10 mV). In turn also the second and third state are shifted to lower energies compared to the hexagonal pore of the Kagomé network and are observed at 73 mV and 200 mV, respectively (blue panel in Figure 6.3.1). The impact of the confinement length can be observed even more clearly, when not only the maximum intensity, but rather the onset energy of the individual confined states is considered (see dashed lines in Figure 6.3.1 as guide for the eyes).

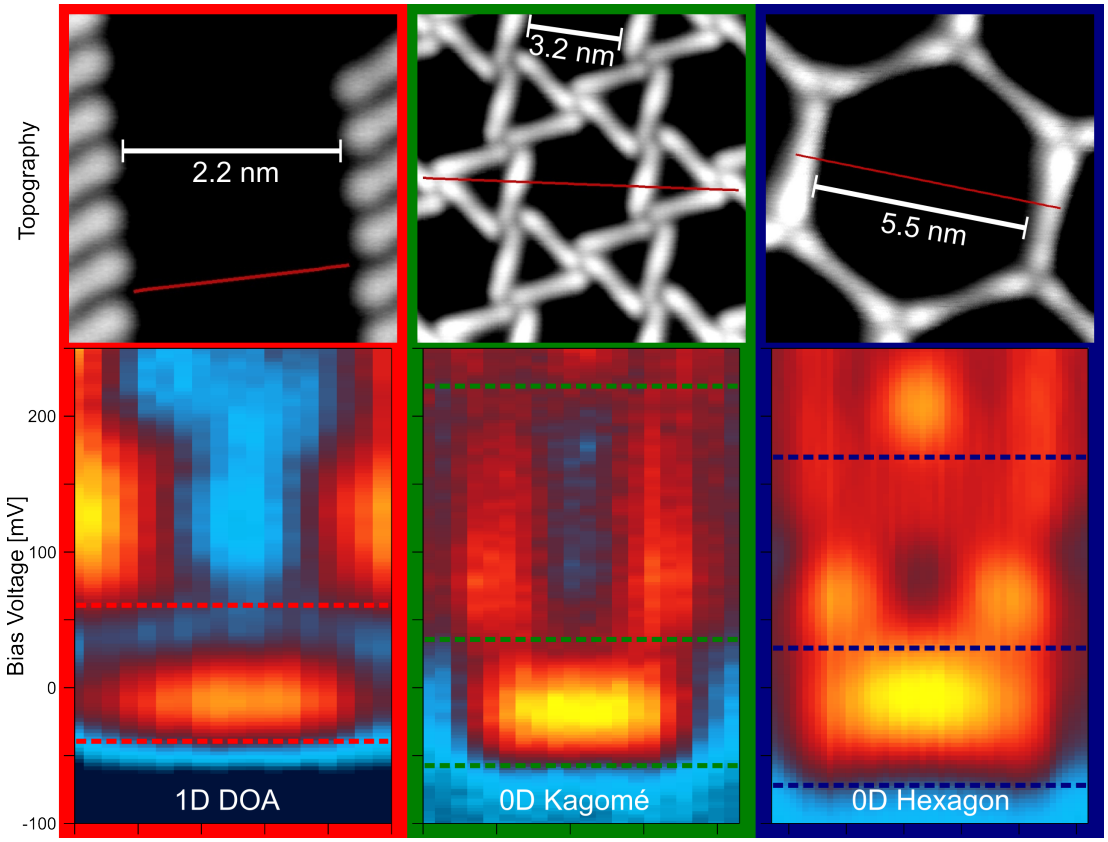

Figure 6.3.1: Comparison of energetics of the first, second and third state in the confining structures described previously. With increasing feature size, the onset energy of the individual states shifts to lower energies. This effect is consistent with the expected particle in a box behavior well established in quantum mechanics. Only the intensity pattern in the center of the discussed pores is depicted in the color plots.

To study the effect of different bonds and adsorbates on the scattering properties of the cavity rim, we can first shortly consider the effect of Co. As mentioned above, single isolated Co atoms act as positive scattering potentials on the Ag(111) surface. The same holds true for single Co atoms adsorbed on top of a phenyl ring of the DOA molecule. As discussed in Section 6.1, the adsorption entails a stronger scattering potential than observed without any adsorbates. This is rationalized by calculations predicting an induced dipole moment in the Co-phenyl half-sandwich com-

plex, pointing towards the phenyl ring [142, 143]. This results in a more negatively charged phenyl ring, since an electron is injected from the metal adsorbate to the phenyl moiety. In contrast, cobalt atoms engaged in metal-ligand coordination bonds in the honeycomb networks, were shown to reverse their scattering characteristics [40, 139]. Therefore, the mere presence of Co is not the decisive factor, whereas the chemical surroundings and state the atom is in are clearly the governing factor.

As a final consideration, the difference between CN···phenyl-bonded SDC molecules and metal-coordination bonds of SDC is addressed. To study both features at the same time, a spectral map of several unoccupied honeycomb pores and pores occupied by guest molecules forming a dimer and a trimeric rotator unit [96, 139] were obtained, see Figure 6.3.2. The molecule positions are indicated by white lines superimposed onto spectroscopy data.

At the first displayed energy of 91 mV (Figure 6.3.2 (a)) the difference between the CN···phenyl and the metal-coordination bonds starts to appear. The molecule backbones display a homogeneous, featureless intensity distribution in the honeycomb lattice, whereas for the trimeric rotator and dimer the intensity is modulated along the molecule. At the Co positions a clear separation of the molecules appears. In contrast, the CN···phenyl bonds between the molecules appear as continuous structures. This has apparently still little effect on the states in the cavities. The smaller confined areas in the occupied hexagons only show a higher onset of the first bound state due to the smaller confined area, as is expected based on previous observations. Also the coupling between individual pores can be expected to be low, due to the low energy in comparison to the height of the scattering barrier. At higher energies however, the situation is different. As can be seen in Figure 6.3.2 (b), at 237 mV the appearance of the molecules changes between the metal-coordinated and CN···phenyl bonded ligands. The molecules forming the hexagonal lattice show a decreased intensity close to the CN terminations along with a notable spatial extension, pointing towards a high transparency of the functional groups and binding motifs

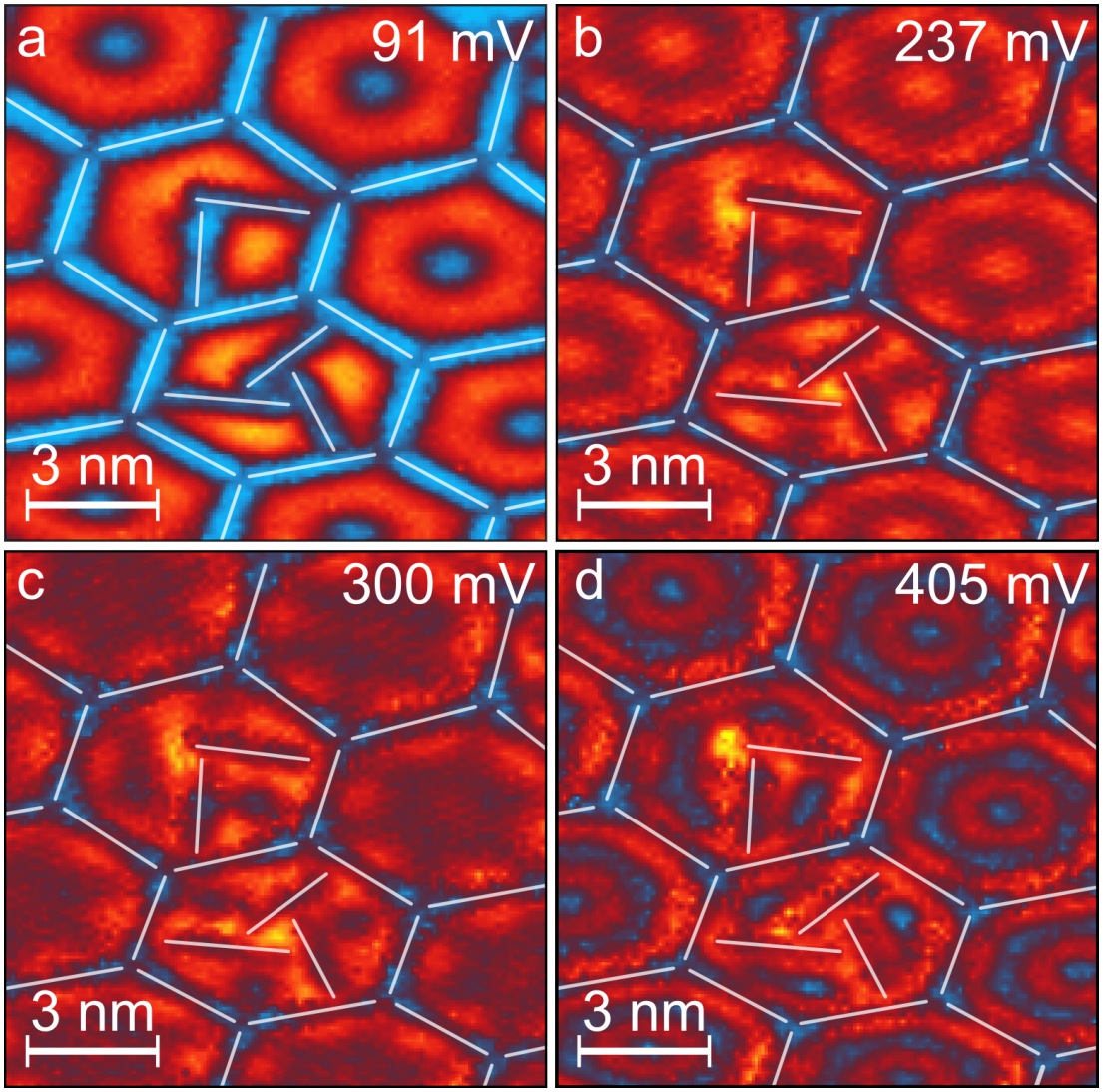

Figure 6.3.2: Comparison of Scattering properties between SDC engaged in CN···phenyl motifs in dimer and trimer units and Co-coordination sites in the honeycomb lattice. The molecule positions are indicated by white lines for clarity. (a) Molecules and SDC-SDC appear as featureless depressions, whereas Co sites appear as distinct separators. (b) Coupling between individual occupied and unoccupied, adjacent pores is observed through the Co sites. The expression of a mode confined within the entire occupied cavity is encouraged by penetration into and tunneling through the molecules. These effects persist with increasing energy (c&d).

for surface electrons. In contrast the rotator and dimer already show substantially higher intensity than the molecules of the host lattice and no distinctive appearance of the CN groups is observed. Further, an intensity peak clearly localized in the small inner pore of the trimer unit appears. According to the scaling behavior with confinement length discussed above, the first bound state within the small pore (radius of r <0.45 nm) would be expected to appear at approximately 700 mV (scaling behavior $1/r^2$, Kagomé pore as reference with r = 1.6 nm, [144]), which can be expected to lie above the scattering barrier height of the molecules. Therefore, this state most likely is linked to a bound state confined within the entire cavity. As is clear from the unoccupied pores, a central node is expected at this energy. Therefore, sufficient penetration into and tunneling through the molecules and CN···phenyl bonds at this energy is reached to ensure a confined state for the entire cavity. A similar observation in the cavity occupied by the dimer unit is made, however here the central node is shifted away from the center of the cavity towards the unsaturated carbonitrile unit at the end of the top guest molecule. For even higher energies (Figure 6.3.2 (c&d)) the effects described above concerning scattering properties of Co sites and molecular backbones persist. Co and the related CN groups on the molecules display low intensity at all energies. The center of the molecules shows significantly increased dI/dV signal, therefore electrons penetrate far into the molecule and are also localized there, whereas the Co sites are now transparent for surface electrons and therefore show low intensity. In the occupied pores, the expression of a cavity mode that is modulated by the structure within is further emphasized, as the energy of the surface state is in the same regime as the scattering barrier height of the molecules and CN···phenyl motifs. The same effect was observed in the Kagomé network, where at 400 mV the CN···phenyl bonds also showed strong localized intensity, see Figure 6.2.3.

The observation of bound states within the occupied pores in the case of the rotator unit is further intriguing due to the rotational dynamics of this system [96]. Once rotational motion of the guest molecules has set in, this will lead to dynamic quantum confinement effects. Therefore, the spatial

LDOS distribution is temporally modulated depending on the position of the rotational unit. This could lead to interesting properties when high rotation speeds and frequencies are reached, as the temporal average of the LDOS in the pore will strongly depend on the guest molecule dynamics.

6.4 Comparative Study of Measurement Techniques

In this final section, the experimental intricacy of LDOS mapping with the STM is addressed. As already mentioned in Chapter 3.1.2, it is possible to acquire spectroscopic data by recording the dI/dV signal while scanning the STM tip in constant current (CC) mode. However, this technique is known to be problematic since the perpetual change in tip-sample-separation results in a convolution of the LDOS related signal with the topography. Therefore, strictly speaking, the spectroscopic data obtained by this method cannot be interpreted as the LDOS. Often this effect is regarded to be a perturbation leading only to a small change of the quantitative aspect of the LDOS. However, here it will be shown that this convolution results in experimental artifacts that are strong enough to produce even qualitatively misleading 2D spectroscopy maps when acquired in CC mode. Further, by applying a renormalization procedure to the previously discussed 2D open-feedback-loop (OFL) maps, the incorrect CC maps can be reproduced. Thereby, the origin of the observed signal in CC mode, induced by the convolution of topography and LDOS, can be well understood.

First, the expected signal for measuring the dI/dV signal while scanning the tip in CC mode is calculated in a simplified model system for several scenarios. We consider a topographically flat surface with spatially varying LDOS, similar to the case of confined surface electrons on silver.

To simulate the effect of feedback-loop operation, a variable tip-sample separation during CC measurements is taken into account. This effect is an expression of the tunneling current depending on the tunneling probability, which in turn depends strongly on the tip-sample separation [135, 136]. Variable tip-sample separations are often not considered, as this parameter can be assumed as constant while taking a single spectrum (see Chapter 2.1.1.2). In a more detailed picture, the tunneling current has to be considered in full, especially, when accurate measurements and conclusions are to be drawn from laterally extended LDOS measurements. When, in contrast to Chapter 2.1.1.2, the density of states on the tip (ρ_T), on the sample

(ρ_S) and the tunneling probability T are not assumed to be constant, the tunneling current, at an energy given by the bias voltage V, is [34]:

$$I = \int_{E_F}^{E_F+eV} \rho_T(E-V)\, \rho_S(\vec{r}_T, E)\, T(z, eV, E)\, dE \tag{6.4.1}$$

In this description, the tunneling probability T is given by

$$T(z, eV, E) = exp\left(-z(\vec{r})\sqrt{\frac{4m}{\hbar^2}\,(\Phi_T + \Phi_S + eV - 2E)}\right) \tag{6.4.2}$$

with tip-sample separation $z(\vec{r})$ at the lateral position $\vec{r}$, the electron mass m and Φ_T and Φ_S the work function of the tip and sample material, respectively.

Even when the DOS on the tip (ρ_T) is assumed to be constant, the differential conductance now depends on the LDOS on the sample ρ_S and the transmission probability T [34]:

$$\begin{aligned} \frac{dI}{dV} &= \frac{d\int_{E_F}^{E_F+eV} \rho_S(\vec{r}_T, E)\, T(z, eV, E)\, dE}{dV} \\ &\propto \rho_S(eV + E_F)\, T(z, eV + E_F) + \int_{E_F}^{E_F+eV} \rho_S(E)\, \frac{dT(E, eV)}{dV}\, dE \end{aligned} \tag{6.4.3}$$

The second term represents a higher energy correction and can, therefore, be neglected at low energies up to several hundreds of mV:

$$\frac{dI}{dV} \propto \rho_S(eV + E_F)\, T(z, eV + E_F) \tag{6.4.4}$$

Nonetheless, it becomes clear that the dI/dV signal depends exponentially on the tip-sample separation. Therefore, when dI/dV spectra are recorded simultaneously with the feedback in CC mode, the measured signal will not reproduce ρ_S.

To show this more clearly, the convolution of the change in tip-sample separation was studied in a simple model system (see Figure 6.4.1).

First, we assume three distinct, linear energy dependencies for the DOS in two regions (*I* and *II*) of the otherwise featureless surface (Figure 6.4.1 (a&b)) in an energy interval between $E_F = 0$ and E_1. When the LDOS is then probed at $E=E_1$, the signal is expected to show two different LDOS traces (Figure 6.4.1 (c)). In one case (black) the LDOS at $E=E_1$ is flat, whereas in the other a step-like behavior (red and blue dashed line) with two distinct D(E) (for reference see the respectively colored traces in Figure 6.4.1 (a&b)) is encountered.

We then calculate the tip-sample separation for a constant tunneling current at $E=E_1$ according to Equation (6.4.1). For the simulation we chose the experimental scenario of a W tip over the Ag(111) surface. Therefore, the work functions were chosen as $\Phi_T = 4.55$, $\Phi_S = 4.74$ and the investigated energy range considered was $E_F = 0$ eV$\rightarrow$ $E_1 = 0.1$ eV which corresponds to a bias voltage of 100 mV; m is the electron mass. From this we can derive the transmission probability in both regions via Equation (6.4.2), which finally allows us to calculate the differential conductance signal (Equation (6.4.4)) when the LDOS is measured in CC mode. The results of the simulated dI/dV traces for the model system are plotted in Figure 6.4.1 (d). Clearly, the obtained signal deviates strongly from the expected behavior (Figure 6.4.1 (c)). Only in one case (blue), the measured dI/dV shows qualitative agreement with the expected LDOS trace, however the intensity ration in regions *I* & *II* is not reproduced correctly. In the other two cases (black and red), the measured differential conductance shows an inverted signal for the red case and a step for black, where a constant LDOS was defined. When an energetically constant D(E) for the step-like LDOS (red and blue) is assumed, the simulation even shows that the dI/dV will only increase by $\sim$ 1 % for a LDOS ratio of 2 in the two regions (not shown). Therefore, we can conclude that dI/dV acquired simultaneously while operating the feedback loop to scan the tip in CC mode does in general not reproduce the correct LDOS.

To illustrate the findings from the model system simulations, we will now compare LDOS-maps acquired in CC-mode with the experiments discussed in previous sections. Therefore, we will first compare a constant current

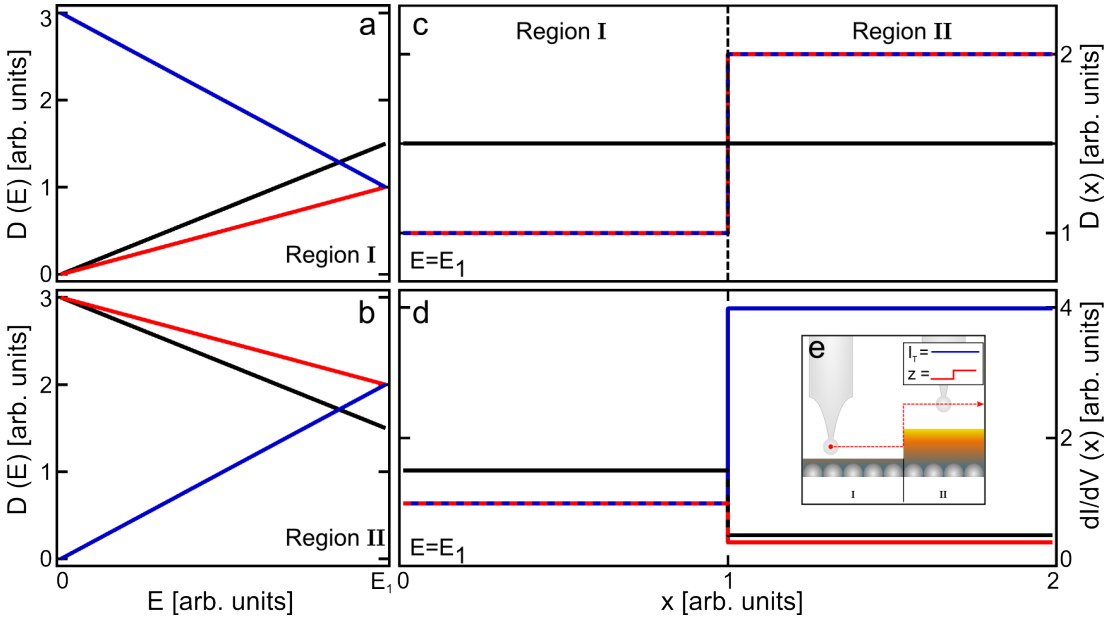

Figure 6.4.1: (a)&(b) Three different energy dependencies of the DOS in two regions (*I* and *II*) of the otherwise featureless surface are used to investigate the convolution of CC mode and simultaneous *dI/dV* measurements. Three different cases of linear energy dependencies (black, blue and red) are compared. At the energy of CC-LDOS map acquisition (E_1), the DOS is either identical (black) or shows a 2:1 ratio (red and blue). (c) Two spatial distribution types for the DOS were chosen at energy E_1: black shows a constant LDOS in both regions, whereas the red and blue dashed line illustrates a step-like behavior. (d) The calculated *dI/dV* signals in region *I* and *II* illustrates the strong artifacts in the *dI/dV* signal in CC mode. For constant LDOS (black), lower intensity is observed in region *II*, for the red case even an inversion of the expected signal occurs. Only the blue case reproduces the *dI/dV* trace qualitatively, however the intensity in region *II* is increased by a factor of 2 compared to the expected signal. The inset (e) illustrates the tip movement, in the red and blue case, that is convoluted with the *dI/dV* signal.

dI/dV line-scan to a physically equivalent trace at a given energy extracted from the series of open-feedback loop spectra acquired across the pores of the Kagomé lattice presented earlier (see in Figure 6.4.2).

Following the trace (red line across the triangular and quasi-hexagonal pore) measured at V_B = -50 mV, the OFL spectra (Figure 6.4.2 (b)), display a

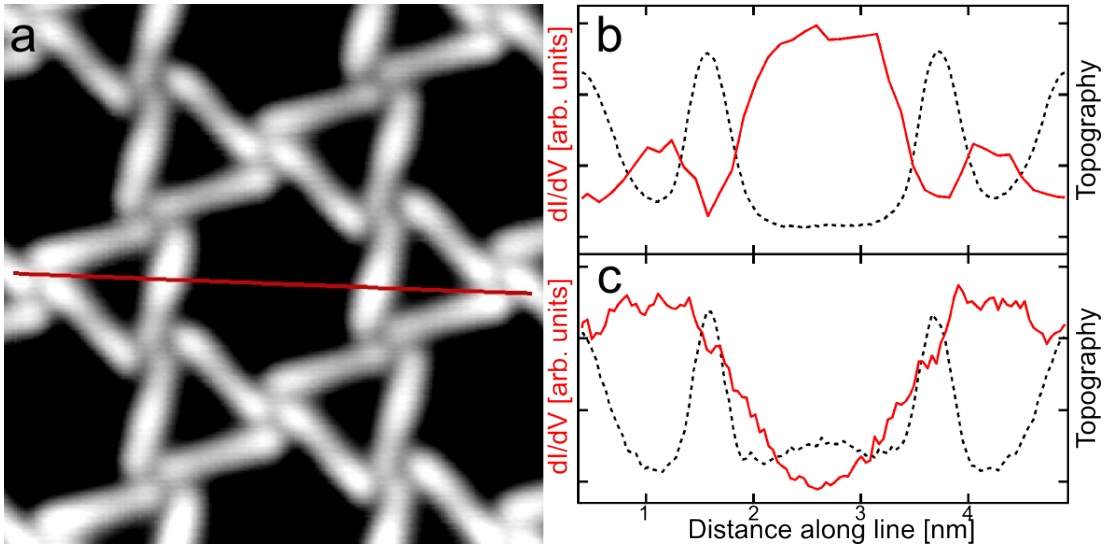

Figure 6.4.2: (a) Topograph of the Kagomé lattice. A red line indicates the cross-section to be investigated by different spectroscopy methods. (b) Black dashed line indicates topography features, whereas the red line shows the LDOS extracted at V_B = -50 mV from the dataset in Figure 6.2.2. The onset of the first bound state in both pores is evident. (c) In contrast the *dI/dV* trace acquired in CC mode shows constant LDOS over the smaller pores and molecules and a depression in the central pore. Therefore, in CC mode a correct reproduction of the LDOS is not possible due to the strong corrugation imposed by the molecules.

high LDOS within each individual pore. In contrast, in the CC *dI/dV* line-scan (Figure 6.4.2 (c)), a depression in the quasi-hexagonal pore and a nearly constant LDOS for both the triangular pores and the molecules is observed. Therefore, in CC *dI/dV* measurements, the extracted LDOS not only strongly deviates from the physically correct case (Figure 6.4.2 (b)), but even shows inverted contrast due to the change in tip-sample separation during the scan across the molecule network.

To further investigate the origin and expression of this effect, CC spectral maps acquired at different energies will be compared to open feedback loop point spectra maps of the Kagomé lattice discussed in a previous section. The application of a modified normalization procedure to the point spectra

maps will illuminate the influence of the CC measurement technique and the convolution of the change in tip-sample separation and the LDOS under investigation.

First, LDOS maps for V_B =-50 mV are shown in the upper row of Figure 6.4.3. CC *dI/dV*, renormalized OFL and the original OFL maps are shown in the left, middle and right column, respectively. Please take note that the different chiralities of the investigated networks are not expected to impact the scattering properties and therefore the bound states can be assumed identical. From the original OFL spectral maps (right, blue border, also see Section 6.2.1) and the line-scan presented above, we expect the onset of the first confined state within both pores of the network at this energy. The CC *dI/dV* map (left, red border) shows a depression within the central pore and nearly constant LDOS on the molecules and triangular pores, as expected from the line-scan in Figure 6.4.2 (c).

The renormalization procedure (as already mentioned in Section 6.2.1) applied to the open-feedback loop maps considers the spectral density in a given energy interval. In the defined energy range the average of the *dI/dV* signal is calculated and all spectra are normalized in order for the average to be identical for all spectra. When data is normalized in the flat, featureless region of the spectra before the onset of the surface state (V_B = -200 to -100 mV), the impact of the change in tunneling probability on the relative intensity at different tip-heights after stabilization is removed.

However, when the renormalization procedure is applied, similar features as in CC mode appear (central column, green border in Figure 6.4.3). The renormalization procedure works similar to the standard normalization, but instead uses the energy interval between the Fermi energy E_F, which in this case is at zero bias, and the bias at which the data is extracted. The renormalized maps are displayed with identical ratios for minimum and maximum intensity as for the CC maps. After renormalization over $[E_F..E]$ (in this case $[0\text{ mV}..-50\text{ mV}]$), a depression is observed in the central pore and the higher intensity on the molecules and the triangular pores. The good agreement between renormalized OFL and CC maps is striking, apart

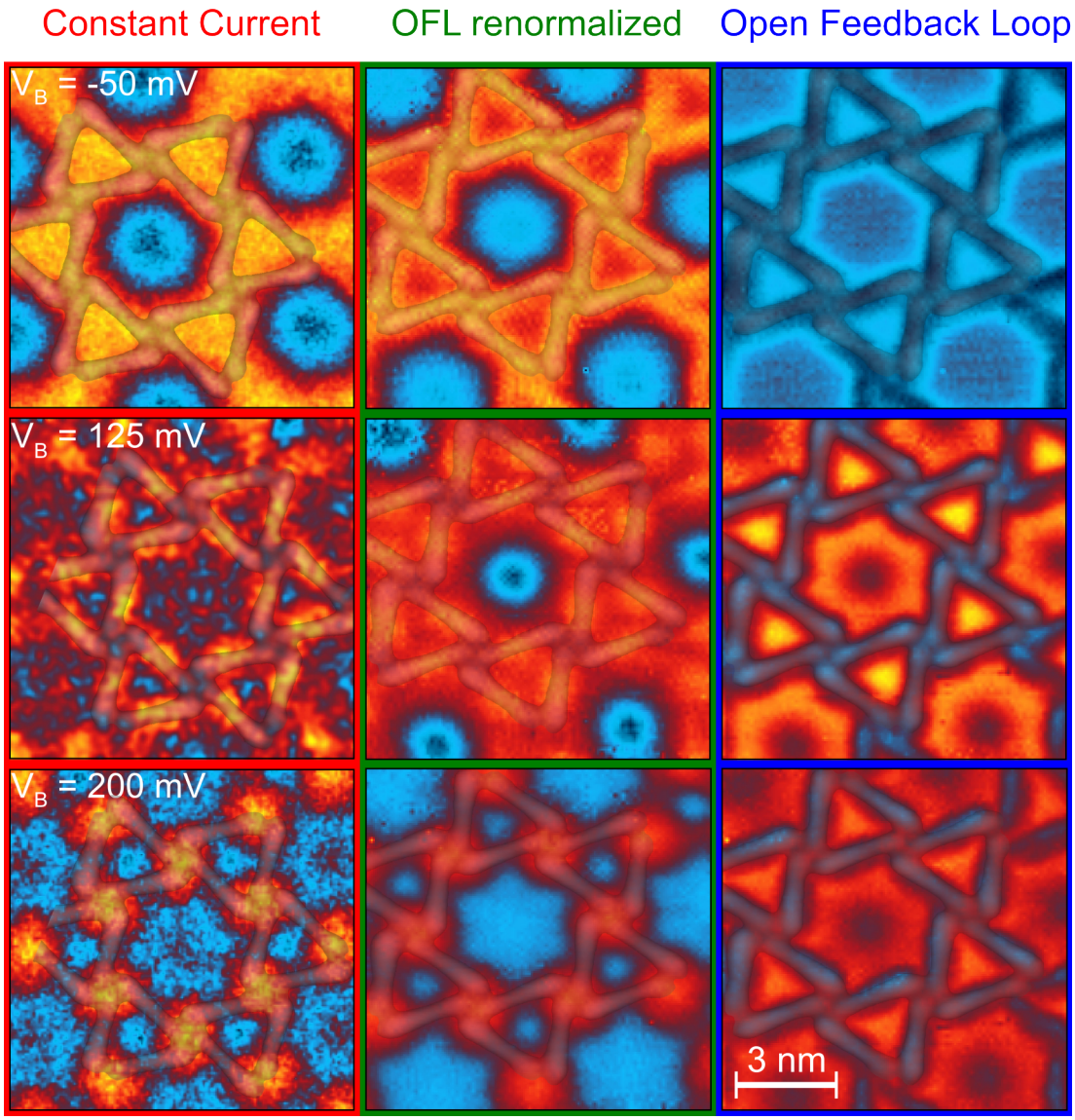

Figure 6.4.3: Constant Current dI/dV maps acquired at energy V_B (left, red panel), open-feedback loop maps renormalized from E_F to E (middle, green panel), OFL maps normalized in the flat, featureless energy range ([−200 mV.. − 100 mV]) of the spectra (right, blue panel). The maps acquired in CC mode (red) do not reproduce the LDOS correctly, as can be directly observed by comparison to the open-feedback loop maps (blue). After renormalization (green) the open-feedback loop maps however reproduce the CC maps in fair (-50 mV and 125 mV) and good agreement (200 mV). Please note that the different chiralities of the investigated networks are not expected to impact the scattering properties and therefore the bound states can be assumed identical.

from the slightly reduced intensity in the triangular pores observed after the renormalization.

At the first bound state within the triangular pores (V_B = 125 mV, second row in Figure 6.4.3) the CC *dI/dV* maps (red border) only show slightly increased intensity along the molecule backbones, depressions in the triangular pores and no clear fine-structure is observed within the central pore. Again, the real LDOS from open-feedback loop measurements (blue) is not reproduced even vaguely, since here the molecules show very little intensity compared to the features of the bound states in the pores. After renormalization (green) over [0 mV..125 mV], a depression in the center of the quasi-hexagonal pore is observed similar to the second bound state found at this energy in the OFL maps. However, the intensity on the molecules is strongly increased accompanied by slight depressions in the triangular pores, similar to the data from CC measurements. Even though ultimately, the renormalization does not reproduce the CC maps in full detail at this energy, the trend towards higher intensity on the molecules and depressions in the pores is the same.

For higher energies, the renormalization procedure simulates the findings from CC maps in great detail. At V_B = 200 mV (bottom row in Figure 6.4.3) the dominant feature observed in CC mode is the high intensity at the 4-fold CN$\cdots$phenyl motifs. The central pore features a slight increase in the center, whereas the triangular pores rather show slight depressions. Upon renormalization, high emphasis in spectral intensity on the binding motifs is observed in combination with inverted intensity patterns in the central and triangular pores. Overall CC mode and renormalized maps show good agreement at this energy.

In the next step, we extend the comparison of the observed features to higher energies. The agreement between CC *dI/dV* maps and renormalized maps is remarkable for the higher energy regime (V_B = 250 mV - 400 mV) as can be seen in Figure 6.4.4.

In this energy range, the renormalization procedure reproduces the CC *dI/dV* maps in high detail. The fine structure and lateral extension of observed features is the same in both cases. First a single peak in the central

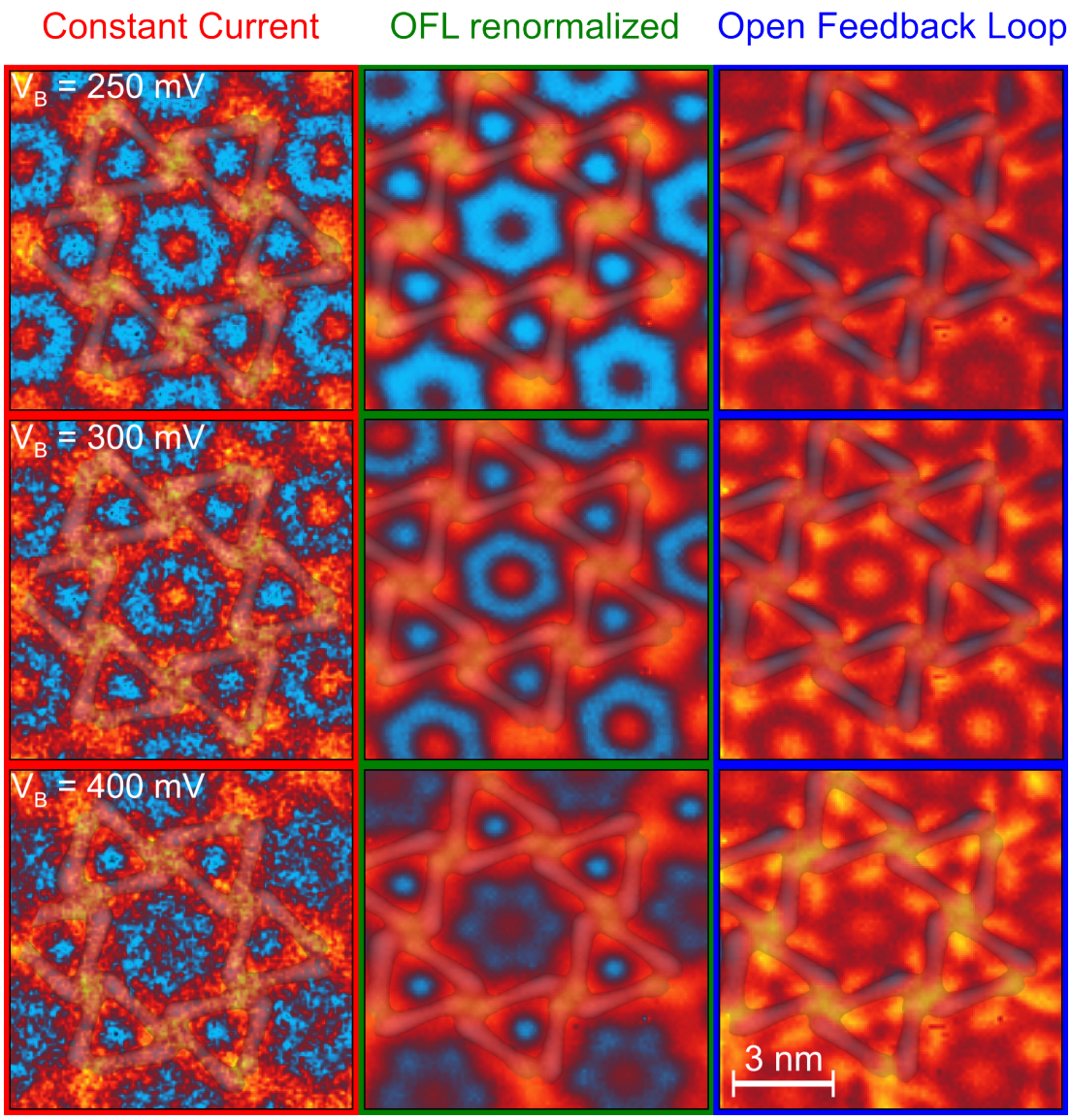

Figure 6.4.4: Constant Current *dI/dV* maps acquired at energy *E* (red panel), open-feedback loop maps renormalized from E_F to *E* (green panel), open-feedback loop maps normalized in the flat, featureless energy range ([−200 mV.. − 100 mV]) of the spectra (blue panel). In the energy range between 250 mV and 400 mV the renormalization of the open-feedback loop maps (green) reproduce the maps acquired in CC mode (red) in terms of spatial distribution and relative intensity in great detail. Please note that the different chiralities of the investigated networks are not expected to impact the scattering properties and therefore the bound states can be assumed identical.

pore with slightly lower intensity than the 4-fold bonding motifs and low intensity in the triangular pores is observed. At V_B = 300 mV the LDOS intensity of the feature in the central pore and at the CN$\cdots$phenyl positions is similar, before a more complex lateral distribution within the central pore accompanied by lower overall intensity occurs at V_B = 400 mV. At the highest investigated energy, the entire molecules again show increased intensity compared to the high emphasis of the binding motifs at lower energies. These features are observed in good agreement and in high detail also after renormalization.

The good agreement between CC dI/dV maps and renormalized OFL maps is based on the convolution of variable tunneling probability with the physically correct LDOS. A procedure to renormalize CC dI/dV maps in order to reproduce only the LDOS rather than the convoluted signal was already introduced in Reference [136]. The procedure is based on a reconstruction method in which the distance dependent transmission probability $T(z)$ was calculated according to Equation (6.4.2). For low bias voltage, the second term in Equation (6.4.3) was found to be negligible and therefore the correct LDOS could be recovered via division by $T(z)$.

In the study presented here, for the reconstruction of CC dI/dV maps from open-feedback loop measurements, the underlying physical considerations are similar. By averaging spectra over the energy range with several features and bound states, a variable tunneling probability at the individual acquisition positions is thereby simulated. Finally, by applying the renormalization, the individual spectra are then multiplied with a factor that is proportional to the tunneling probability at this energy and position.

The contribution of all spectral features in the considered energy interval, even though electrons close to E_F are considered to mainly contribute to the tunneling current, to the dI/dV maps in constant current mode is essential factor here. As shown in Figure 6.4.5, the relative intensities and spatial extension of the features observed in the CC dI/dV maps (Figure 6.4.5 (a)) are only reproduced for the renormalization in the interval [0 mV..300 mV] (Figure 6.4.5 (b)), whereas the renormalization

[0 mV..150 mV] and [150 mV..300 mV] only reproduces the overall symmetry but not the exact appearance (Figures 6.4.5 (c&d), respectively). Specific features are overemphasized in (c) and (d), whereas in (b) the relative intensity is observed in accordance to the CC *dI/dV* map.

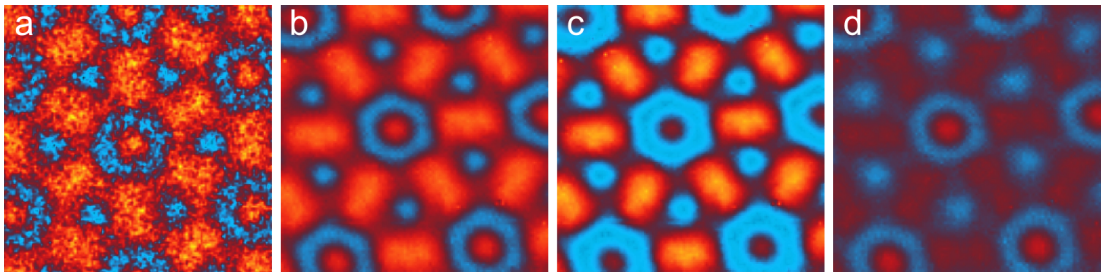

Figure 6.4.5: (a) Constant current *dI/dV* map acquired at V_B = 300 mV. (b) Open-feedback loop map after renormalization [0 mV..300 mV] shows exact agreement in spatial distribution and relative intensities. (c) Renormalization over the energy range [0 mV..150 mV] reproduces the overall symmetry, however the binding motifs are overemphasized in intensity. (d) When only energies close to the acquisition energy are considered ([150 mV..300 mV]), the feature in the central pore shows too high intensity compared to CN···phenyl positions.

Overall, for quantitative and even qualitative data interpretation in LDOS spectroscopy mapping with the STM, great care has to be taken. Constant current spectroscopy mapping typically does not reproduce the actual local density of states on the surface. The recovery of the LDOS from CC *dI/dV* maps is only possible for rather well known systems and only for atomically flat surfaces [136]. To circumvent this obstacle, maps constructed from single point spectra, for which the tunneling current was stabilized far away from spectral features and which are properly normalized, are a viable and correct alternative, even though the process is more time-consuming if only a map at one energy is of interest. However, when OFL maps are acquired, a full dataset in the given energy range is produced and, therefore, similar time is required compared to recording a comparable dataset of CC *dI/dV* maps. Further, the exact lateral positions of the investigated features is constant throughout all maps, which allows a direct comparison and thereby reduces the proneness to error.

Chapter 7

Summary and Outlook

Within this thesis, the prospects of employing supramolecular templates to steer the assembly and formation of nanostructures as well as controlling and tuning electronic properties at the nanoscale have been explored. Thereby, it was shown that molecular architectures formed via self-assembly are systems that can be adapted to the exact requirements demanded from them and are therefore highly versatile. However, there are still challenges that have to be faced in fundamental research, before potential applications can be realized. Nonetheless, steps towards understanding the mechanisms behind the investigated model systems and the possibilities for their further functionalization have been made.

The presented study on the site-selective positioning of single atoms or clusters proposes supramolecular templates as host systems. By investigating in a first step the formation of nanogratings and saturated monolayers from N,N'-diphenyl oxalic amide via self-assembly, it could be shown that the Ag(111) substrate plays a key role in determining the exact assembly protocol. The molecules assemble in the sub-monolayer case into more strongly bound pairs, whereas the entire structure is dictated by the substrate registry. In the dense packed phase the pairing disappears as the molecular layer is compressed and rectified. Further, it was shown that the dense packed assembly is more robust. This became clear, when the

adsorption of atomic cobalt onto the molecular nanograting and the monolayer template was studied, respectively. The more stable molecular monolayer did not show any adsorbate induced deformations even at high coverages, whereas the nanogratings were more susceptible to defect formation. The formation of Co-phenyl half-sandwich complexes was then investigated further and a fairly complex organization dynamics was observed at variable substrate temperatures and adsorbate coverages. Therefore, employing molecular ligands for the templating of surfaces to gain control over the exact positioning of adsorbates was demonstrated. There are still open questions concerning the magnetic properties of the Co-phenyl half-sandwich complexes. Even though there are indications pointing towards the conservation of the cobalts magnetic properties, the respective gas phase calculations for these structures need not hold true in the presence of a metal surface. However, the presented study demonstrates the great potential of site-selective adsorption and positioning processes by employing molecular templates. In further steps this concept could be extended to build architectures reaching into the third dimension by attaching structures to selectively adsorbed atoms and thereby forming sandwich or multilayer architectures.

Furthermore, in an attempt to mimic an assembly process found in many biological systems, namely hierarchically driven self-assembly, the organization of bi-component molecular networks from sexiphenyl-dicarbonitrile (SDC) and N,N’-diphenyl oxalic amide (DOA) was investigated on Ag(111). Thereby, it was found that the organization into networks depends mainly on the stoichiometric ratio of the provided constituents. The observed novel binding mechanism between DOA and SDC was found to be satisfied first, as preferential bonding of the constituents at low molecule coverages was found to occur. The SDC-DOA interaction proved to be the essential binding motif for all subsequently discovered network geometries. This observation indicated that the SDC-DOA binding is the energetically most favorable of all the bonds involved. However, the exact arrangement of the molecules is dictated by the surface registry of the Ag(111) substrate. Therefore, detailed adsorption modeling for all network types was necessary to unravel

the origin of long range order and chirality in the different phases. This led to the conclusion that all formed assemblies are commensurate with the Ag(111) lattice and we could thereby extract the exact alignment of the molecules relative to one another with atomic precision. In a final step, by simulating the binding energetics in the system in an adlayer focused approach, we identified the SDC-DOA binding in combination with a cooperative effect stabilizing the entire assembly as the strongest bond, thereby confirming the experimentally observed hierarchic principles for the growth process. By tailoring molecular systems towards assembly following hierarchic organization principles, higher control could be achieved by introducing higher degrees of sophistication in terms of ligand and constituent design. Ultimately, by incorporating hierarchic energetics for the desired lateral interactions, this approach represents a viable route towards incorporating and addressing functional units like single molecule transistors, switches or magnets.

Finally, the modification of surface electronic properties via molecular adsorbates and networks was addressed. In the presented systems, the effect of decreasing dimensionality and size leading to the quantum confinement of surface electrons was demonstrated. Even though the studied systems could be experimentally assessed and theoretically analyzed in great detail, the intricacy of mapping the local density of states with the STM showed to be non-trivial and great caution is advised. It was shown that molecular assemblies represent an extremely versatile approach towards controlling surface electronic properties. By extending the confinement picture away from the very localized effect of quantum wire or dot formation, this route is a promising candidate for controlled macroscopic electronic property modification of surfaces and interfaces. By structuring entire surfaces with well-defined molecular templates, the resulting coupled nanosystems can, when properly designed, lead to the formation of a new, modified surface electronic structure. It was very recently demonstrated that, by a similar approach via the positioning individual adsorbates into a hexagonal lattice, surface electrons on Cu(111) can show similar properties as those found in graphene [145]. Ultimately, by patterning surfaces

via molecular superstructures, a controlled modification of the surface band structure could be achieved, which might be applied in interface devices.

Since the conceptual idea of using self-assembly protocols to realize functional nanoarchitectures and -structures has been proposed more than 20 years ago, scientific and technological progress has steadily advanced toward this goal. Even though by now many ideas have been demonstrated in model systems, fully operational devices and applications are still out of reach. Nonetheless, the studies presented in this thesis have demonstrated that the foundations can be rationalized at this point in time. Therefore, by exploring the routes into the nanoworld many new and exciting discoveries are still awaiting.

List of Publications

- **Dichotomous Array of Chiral Quantum Corrals by a Self-Assembled Nanoporous Kagomé Network**
  F. Klappenberger, D. Kühne, W. Krenner, I. Silanes, A. Arnau, F. J. G. de Abajo, S. Klyatskaya, M. Ruben, J.V. Barth, *Nano Lett.* **9**, 3509-3514 (2009)

- **Magnetism in a Mn modulation-doped InAs/InGaAs heterostructure with a two-dimensional hole system**
  B. Rupprecht, W. Krenner, U. Wurstbauer, Ch. Heyn, T. Windisch, M. A. Wilde, W. Wegscheider, D. Grundler, *J. Appl. Phys.* **107**, 093711 (2010)

- **Rotational and Constitutional Dynamics of Caged Supramolecules**
  D. Kühne, F. Klappenberger, W. Krenner, S. Klyatskaya, M. Ruben, and J.V. Barth, *Proc. Nat. Acad. Sci.* **107**, 21332-21336 (2010)

- **Tunable Quantum Dot Arrays Formed from Self-Assembled Metal-Organic Networks**
  F. Klappenberger, D. Kühne, W. Krenner, I. Silanes, A. Arnau, F.J.G. de Abajo, S. Klyatskaya, M. Ruben, J.V. Barth, *Phys. Rev. Lett.* **106**, 026802 (2011)

- **Surface-Confined Self-Assembly of Di-carbonitrile Polyphenyls**
  S. Klyatskaya, F. Klappenberger, U. Schlickum, D. Kühne, M. Marschall, J. Reichert, R. Decker, W. Krenner, G. Zoppellaro, H. Brune, J. V. Barth, M. Ruben, *Adv. Func. Mat.* **21-7**, 1230-1240 (2011)

- **Uniform π-system Alignment in thin Films of Template-Grown Dicarbonitrile-Oligophenyls**
  F. Klappenberger, D. Kühne, M. Marschall, S. Neppl, W. Krenner, A. Nefedov, T. Strunskus, Ch. Wöll, S. Klyatskaya, M. Ruben, J.V. Barth, *Adv. Func. Mat.* **21-7**, 1631-1641 (2011)

- **Positioning of Single Co Atoms Steered by a Self-Assembled Organic Molecular Template**
  W. Krenner, F. Klappenberger, D. Kühne, K. Diller, Z.-R. Qu, M. Ruben, J.V. Barth, *J. Phys. Chem. Lett.* **2**, 1639-1645 (2011)

- **Hierarchically Organized Bimolecular Ladder Network Exhibiting Guided One-Dimensional Diffusion**
  Y. Makoudi, E. Arras, N. Kepčija, W. Krenner, S. Klyatskaya, F. Klappenberger, M. Ruben, A.P. Seitsonen, J.V. Barth, *ACS Nano* **6 (1)**, 549-556 (2012)

- **Unraveling the Hierarchic Formation of Open-porous Bimolecular Networks**
  W. Krenner, F. Klappenberger, N. Kepčija, E. Arras, Y. Makoudi, D. Kühne, S. Klyatskaya, M. Ruben, J.V. Barth, *J. Phys. Chem. C* **116**, 16421-16429 (2012)

References

[1] W. B. Shockley, J. Bardeen, and W. H. Brattain. **Noble Lecture, Elsevier Publishing Company**. *Nobel Lectures, Physics 1942-1962*, 1964. 1

[2] R. Feynman. **There's Plenty of Room at the Bottom**. *Engineering and Science*, **23**:22–26, 1960. 1

[3] A. B. Fowler, F. F. Fang, W. E. Howard, and P. J. Stiles. **Magneto-Oscillatory Conductance in Silicon Surfaces**. *Phys. Rev. Lett.*, **16**:901–903, 1966. 1

[4] F. Stern and W. E. Howard. **Properties of Semiconductor Surface Inversion Layers in the Electric Quantum Limit**. *Phys. Rev.*, **163**:816–835, 1967. 1

[5] K. v. Klitzing, G. Dorda, and M. Pepper. **New Method for High-Accuracy Determination of the Fine-Structure Constant Based on Quantized Hall Resistance**. *Phys. Rev. Lett.*, **45**:494–497, 1980. 1

[6] D. C. Tsui, H. L. Stormer, and A. C. Gossard. **Two-Dimensional Magnetotransport in the Extreme Quantum Limit**. *Phys. Rev. Lett.*, **48**:1559–1562, 1982. 1

[7] G. Binnig, H. Rohrer, Ch. Gerber, and E. Weibel. **Surface Studies by Scanning Tunneling Microscopy**. *Phys. Rev. Lett.*, **49**:57–61, 1982. 2, 8

[8] G. Binnig and H. Rohrer. **Scanning Tunneling Microscopy - From Birth to Adolescence (Nobel Lecture)**. *Angew. Chem. Int. Ed.*, **26**:606–614, 1987. 2

[9] J. Repp, G. Meyer, S. Paavilainen, F. E. Olsson, and M. Persson. **Imaging Bond Formation Between a Gold Atom and Pentacene on an Insulating Surface**. *Science*, **312**:1196–1199, 2006. 3, 91

[10] S.-W. Hla, L. Bartels, G. Meyer, and K.-H. Rieder. **Inducing All Steps of a Chemical Reaction with the Scanning Tunneling Microscope Tip: Towards Single Molecule Engineering**. *Phys. Rev. Lett.*, **85**:2777–2780, 2000. 3

[11] K. McElroy, R. W. Simmonds, J. E. Hoffman, D.-H. Lee, J. Orenstein, H. Eisaki, S. Uchida, and J. C. Davis. **Relating Atomic-scale Electronic Phenomena to Wave-like Quasiparticle States in Superconducting $Bi_2Sr_2CaCu_2O_{8+\delta}$**. *Nature*, **422**:592–596, 2003. 3, 91

[12] B. C. Stipe, M. A. Rezaei, and W. Ho. **Single-Molecule Vibrational Spectroscopy and Microscopy**. *Science*, **280**:1732–1735, 1998. 3

[13] S. Loth, M. Etzkorn, C. P. Lutz, D. M. Eigler, and A. J. Heinrich. **Measurement of Fast Electron Spin Relaxation Times with Atomic Resolution**. *Science*, **329**:1628–1630, 2010. 3

[14] G.M. Whitesides, J.P. Mathias, and C.T. Seto. **Molecular Self-assembly and Nanochemistry: A Chemical Strategy for the Synthesis of Nanostructures**. *Science*, **254**:1312–1319, 1991. 3, 25, 71

[15] J.-M. Lehn. **Supramolecular Chemistry: Molecular Information and the Design of Supramolecular Materials**. *Makromolekulare Chemie. Macromolecular Symposia*, **69**:1–17, 1993. 3, 71

[16] J. H. Burroughes, D. D. C. Bradley, A. R. Brown, R. N. Marks, K. Mackay, R. H. Friend, P. L. Burns, and A. B. Holmes. **Light-emitting Diodes Based on Conjugated Polymers**. *Nature*, **347**:539–541, 1990. 3

[17] L. Kouwenhoven. **Single-Molecule Transistors**. *Science*, **275**:1896–1897, 1997. 3

[18] L. Bogani and W. Wernsdorfer. **Molecular Spintronics Using Single-Molecule Magnets**. *Nat. Mater.*, **7**:179–186, 2008. 3, 71

[19] J. Bardeen. **Tunnelling from a Many-Particle Point of View**. *Phys. Rev. Lett.*, **6**:57–59, 1961. 9

[20] J. Tersoff and D. R. Hamann. **Theory and Application for the Scanning Tunneling Microscope**. *Phys. Rev. Lett.*, **50**:1998–2001, 1983. 10, 11, 15

[21] J. Tersoff and D. R. Hamann. **Theory of the Scanning Tunneling Microscope**. *Phys. Rev. B*, **31**:805–813, 1985. 10, 15

[22] Y. Kohsaka, C. Taylor, K. Fujita, A. Schmidt, C. Lupien, T. Hanaguri, M. Azuma, M. Takano, H. Eisaki, H. Takagi, S. Uchida, and J. C. Davis. **An Intrinsic Bond-Centered Electronic Glass with Unidirectional Domains in Underdoped Cuprates**. *Science*, **315**:1380–1385, 2007. 10

[23] Y. Pennec, N. J. C. Ingle, I. S Elfimov, E. Varene, Y. Maeno, A. Damascelli, and J. V. Barth. **Cleaving-Temperature Dependence of Layered-Oxide Surfaces**. *Phys. Rev. Lett.*, **101**:216103, 2008. 10

[24] R. Waser. **Resistive Non-volatile Memory Devices**. *Microelectron. Eng.*, **86**:1925 – 1928, 2009. 10

[25] V. M. Hallmark, S. Chiang, J. F. Rabolt, J. D. Swalen, and R. J. Wilson. **Observation of Atomic Corrugation on Au(111) by Scanning Tunneling Microscopy**. *Phys. Rev. Lett.*, **59**:2879–2882, 1987. 11

[26] J. Wintterlin, J. Wiechers, H. Brune, T. Gritsch, H. Höfer, and R. J. Behm. **Atomic-Resolution Imaging of Close-Packed Metal Surfaces by Scanning Tunneling Microscopy**. *Phys. Rev. Lett.*, **62**:59–62, 1989. 11

[27] P. H. Lippel, R. J. Wilson, M. D. Miller, Ch. Wöll, and S. Chiang. **High-Resolution Imaging of Copper-Phthalocyanine by Scanning-Tunneling Microscopy**. *Phys. Rev. Lett.*, **62**:171–174, 1989. 11

[28] J. V. Barth, H. Brune, G. Ertl, and R. J. Behm. **Scanning Tunneling Microscopy Observations on the Reconstructed Au(111) Surface: Atomic Structure, Long-range Superstructure, Rotational Domains, and Surface Defects**. *Phys. Rev. B*, **42**:9307–9318, 1990. 11

[29] B. Das and J. Mahanty. **Spatial Distribution of Tunnel Current and Application to Scanning Tunneling Microscopy: A Semiclassical Treatment**. *Phys. Rev. B*, **36**:898–903, 1987. 11

[30] C. J. Chen. **Origin of Atomic Resolution on Metal Surfaces in Scanning Tunneling Microscopy**. *Phys. Rev. Lett.*, **65**:448–451, 1990. 12

[31] L. Gross, N. Moll, F. Mohn, A. Curioni, G. Meyer, F. Hanke, and M. Persson. **High-Resolution Molecular Orbital Imaging Using a *p*-Wave STM Tip**. *Phys. Rev. Lett.*, **107**:086101, 2011. 14

[32] A. Selloni, P. Carnevali, E. Tosatti, and C. D. Chen. **Voltage-dependent Scanning Tunneling Microscopy of a Crystal Surface: Graphite**. *Phys. Rev. B*, **31**:2602–2605, 1985. 15

[33] N. D. Lang. **Spectroscopy of Single Atoms in the Scanning Tunneling Microscope**. *Phys. Rev. B*, **34**:5947–5950, 1986. 15

[34] R. J. Hamers. **Atomic-resolution Surface Spectroscopy With the Scanning Tunneling Microscope**. *Annu. Rev. Phys. Chem.*, **40**:531–559, 1989. 15, 118

[35] J. A. Kubby and J. J. Boland. **Scanning Tunneling Microscopy of Semiconductor Surfaces**. *Surf. Sci. Rep.*, **26**:61 – 204, 1996. 15

[36] N. Memmel. **Monitoring and Modifying Properties of Metal Surfaces by Electronic Surface States**. *Surf. Sci. Rep.*, **32**:91 – 163, 1998. 16, 17, 18

[37] F. Reinert, G. Nicolay, S. Schmidt, D. Ehm, and S. Hüfner. **Direct Measurements of the *L* -gap Surface States on the (111) face of Noble Metals by Photoelectron Spectroscopy**. *Phys. Rev. B*, **63**:115415, 2001. 19, 103

[38] J. Li, W.-D. Schneider, R. Berndt, and S. Crampin. **Electron Confinement to Nanoscale Ag Islands on Ag(111): A Quantitative Study**. *Phys. Rev. Lett.*, **80**:3332–3335, 1998. 20, 92

[39] M. F. Crommie, C. P. Lutz, and D. M. Eigler. **Imaging Standing Waves in a 2-Dimensional Electron-Gas**. *Nature*, **363**:524–527, 1993. 20, 91

[40] F. Klappenberger, D. Kühne, W. Krenner, I. Silanes, A. Arnau, F. J. G. de Abajo, S. Klyatskaya, M. Ruben, and J. V. Barth. **Dichotomous Array of Chiral Quantum Corrals by a Self-Assembled Nanoporous Kagome Network**. *Nano Lett.*, **9**:3509–3514, 2009. 20, 75, 92, 97, 109, 110, 113

[41] F. Klappenberger, D. Kühne, W. Krenner, I. Silanes, A. Arnau, F. J. García de Abajo, S. Klyatskaya, M. Ruben, and J. V. Barth. **Tunable Quantum Dot Arrays Formed from Self-Assembled Metal-Organic Networks**. *Phys. Rev. Lett.*, **106**:026802, 2011. 20, 75, 92, 97

[42] L. Bürgi, O. Jeandupeux, A. Hirstein, H. Brune, and K. Kern. **Confinement of Surface State Electrons in Fabry-Pérot Resonators**. *Phys. Rev. Lett.*, **81**:5370–5373, 1998. 20, 92

[43] A. Messiah. *Quantum Mechanics*. Dover Publications, 1999. 21

[44] V. Myroshnychenko, E. Carbó-Argibay, I. Pastoriza-Santos, J. Pérez-Juste, L. M. Liz-Marzán, and F. J. García de Abajo. **Modeling the Optical Response of Highly Faceted Metal Nanoparticles with a Fully 3D Boundary Element Method**. *Adv. Mater.*, **20**:4288–4293, 2008. 22

[45] J. V. Barth. *Properties of Single Organic Molecules on Crystal Surfaces*. Imperial College Press, London, 2006. 24

[46] J. V. Barth. **Transport of Adsorbates at Metal Surfaces: From Thermal Migration to Hot Precursors**. *Surf. Sci. Rep.*, **40**:75–149, 2000. 24, 65

[47] H. Brune. **Microscopic View of Epitaxial Metal Growth: Nucleation and Aggregation**. *Surf. Sci. Rep.*, **31**:125–229, 1998. 24, 65

[48] S. Clair. *Investigation of Low-Dimensional Supramolecular Architectures by Low-Temperature Scanning Tunneling Microscopy*. PhD thesis, Ecole Polytechnique Federale de Lausanne, 2004. 27, 32

[49] K. Besocke. **An Easily Operable Scanning Tunneling Microscope**. *Surf. Sci.*, **181**:145 – 153, 1987. 27, 28

[50] J. Frohn, J. F. Wolf, K. Besocke, and M. Teske. **Coarse Tip Distance Adjustment and Positioner for a Scanning Tunneling Microscope**. *Rev. Sci. Instr.*, **60**:1200–1201, 1989. 27, 28

[51] S. H. Pan. **Piezo-electric Motor**. *International Patent Publication No. WO 93/19494*, **International Bureau**:World Intellectual Property Organization, 30 September 1993. 27, 28

[52] **SPECS Surface Nano Analysis GmbH, Berlin, Germany**. 27, 38

[53] G. Meyer. **A Simple Low-temperature Ultrahigh-vacuum Scanning Tunneling Microscope Capable of Atomic Manipulation**. *Rev. Sci. Instr.*, **67**:2960, 1996. 32

[54] **CreaTec Fischer & Co. GmbH, Erligheim/Berlin, Germany**. 32

[55] J. Klein, A. Léger, M. Belin, D. Défourneau, and M. J. L. Sangster. **Inelastic-Electron-Tunneling Spectroscopy of Metal-Insulator-Metal Junctions**. *Phys. Rev. B*, **7**:2336–2348, 1973. 37

[56] B. C. Stipe, M. A. Rezaei, and W. Ho. **A Variable-temperature Scanning Tunneling Microscope Capable of Single-molecule Vibrational Spectroscopy**. *Rev. Sci. Instr.*, **70**(1):137–143, 1999. 37

[57] L. Zhang, T. Miyamachi, T. Tomanic, R. Dehm, and W. Wulfhekel. **A Compact sub-Kelvin Ultrahigh Vacuum Scanning Tunneling Microscope with High Energy Resolution and High Stability**. *Rev. Sci. Instr.*, **82**:103702, 2011. 38

[58] P. Gambardella, M. Blanc, H. Brune, K. Kuhnke, and K. Kern. **One-Dimensional Metal Chains on Pt Vincinal Surfaces**. *Phys. Rev. B*, **61**:2254, 2000. 51

[59] P. Gambardella, S. Stepanow, A. Dmitriev, J. Honolka, F. M. F. de Groot, M. Lingenfelder, S. Sen Gupta, D. D. Sarma, P. Bencok, S. Stanescu, S. Clair, S. Pons, N. Lin, A. P. Seitsonen, H. Brune, J. V. Barth, and K. Kern. **Supramolecular Control of the Magnetic Anisotropy in Two-Dimensional High-Spin Fe Arrays at a Metal Interface**. *Nat. Mater.*, **8**:189–193, 2009. 51, 71

[60] H. Wende, M. Bernien, J. Luo, C. Sorg, N. Ponpandian, J. Kurde, J. Miguel, M. Piantek, X. Xu, Ph. Eckhold, W. Kuch, K. Baberschke, P. M. Panchmatia, B. Sanyal, P. M. Oppeneer, and O. Eriksson. **Substrate-Induced Magnetic Ordering and Switching of Iron Porphyrin Molecules**. *Nat. Mater.*, **6**:516–520, 2007. 51, 71

[61] P. Gambardella, S. Rusponi, M. Veronese, S. S. Dhesi, C. Grazioli, A. Dallmeyer, I. Cabria, R. Zeller, P. H. Dederichs, K. Kern, C. Carbone, and H. Brune. **Giant Magnetic Anisotropy of Single Cobalt Atoms and Nanoparticles**. *Science*, **300**:1130–1133, 2003. 51

[62] N. Weiss, T. Cren, M. Epple, S. Rusponi, G. Baudot, S. Rohart, A. Tejeda, V. Repain, S. Rousset, P. Ohresser, F. Scheurer, P. Bencok, and H. Brune. **Uniform Magnetic Properties for an Ultrahigh-Density Lattice of Noninteracting Co Nanostructures**. *Phys. Rev. Lett.*, **95**:157204, 2005. 51

[63] S. Pick, V. S. Stepanyuk, A. L. Klavsyuk, L. Niebergall, W. Hergert, J. Kirschner, and P. Bruno. **Magnetism and Structure on the Atomic Scale: Small Cobalt Clusters in Cu(001)**. *Phys. Rev. B*, **70**:224419, 2004. 51

[64] C. F. Hirjibehedin, C. P. Lutz, and A. J. Heinrich. **Spin Coupling in Engineered Atomic Structures**. *Science*, **312**:1021–1024, 2006. 51

[65] P. Wahl, P. Simon, L. Diekhoner, V. S. Stepanyuk, P. Bruno, M. A. Schneider, and K. Kern. **Exchange Interaction between Single Magnetic Adatoms**. *Phys. Rev. Lett.*, **98**:056601, 2007. 51

[66] W. Krenner, F. Klappenberger, D. Kühne, K. Diller, Z.-R. Qu, M. Ruben, and J. V. Barth. **Positioning of Single Co Atoms Steered by a Self-Assembled Organic Molecular Template**. *J. Phys. Chem. Lett.*, **2**:1639–1645, 2011. 51, 71, 75, 80

[67] R. Meyer and A. Seeliger. **Über die Einwirkung von Oxaläther auf Aromatische Amidokörper**. *Chem. Ber.*, **29**:2640–2645, 1896. 52

[68] F. Klappenberger, M. E. Cañas-Ventura, S. Clair, S. Pons, U. Schlickum, Z. R. Qu, H. Brune, K. Kern, T. Strunskus, C. Wöll, A. Comisso, A. De Vita, M. Ruben, and J. V. Barth. **Conformational Adaptation in Supramolecular Assembly on Surfaces**. *ChemPhysChem*, **8**:1782–1786, 2007. 53, 55, 75, 84, 87

[69] F. Klappenberger, M. E. Cañas-Ventura, S. Clair, S. Pons, U. Schlickum, Z. R. Qu, T. Strunskus, A. Comisso, C. Wöll, H. Brune, K. Kern, A. DeVita, M. Ruben, and J. V. Barth. **Does the Surface Matter? Hydrogen Bonded Chain Formation of an Oxalic Amide Derivative in Two and Three Dimensional Environment**. *ChemPhysChem*, **9**:2522–2530, 2008. 53, 55, 56, 71, 75

[70] J. V. Barth, J. Weckesser, C. Cai, P. Günter, L. Bürgi, O. Jeandupeux, and K. Kern. **Building Supramolecular Nanostructures at Surfaces by Hydrogen Bonding**. *Angew. Chem. Int. Ed.*, **39**:1230–1234, 2000. 53

[71] A. Schiffrin, A. Riemann, W. Auwärter, Y. Pennec, A. Weber-Bargioni, D. Cvetko, A. Cossaro, A. Morgante, and J. V. Barth. **Zwitterionic Self-aAsembly of l-Methionine Nanogratings on the Ag(111) Surface**. *Proc. Natl. Acad. Sci. U. S. A.*, **104**:5279–5284, 2007. 53

[72] Y. Pennec, W. Auwärter, A. Schiffrin, A. Weber-Bargioni, A. Riemann, and J. V. Barth. **Supramolecular Gratings for Tuneable Confinement of Electrons on Metal Surfaces**. *Nat. Nano.*, **2**:99–103, 2007. 53, 92, 93

[73] R. Xiao, D. Fritsch, M. D. Kuz'min, K. Koepernik, H. Eschrig, M. Richter, K. Vietze, and G. Seifert. **Co Dimers on Hexagonal Carbon Rings Proposed as Subnanometer Magnetic Storage Bits**. *Phys. Rev. Lett.*, **103**:187201, 2009. 58, 63, 69

[74] R. Xiao, D. Fritsch, M. D. Kuz'min, K. Koepernik, M. Richter, K. Vietze, and G. Seifert. **Prediction of Huge Magnetic Anisotropies of Transition-metal Dimer-benzene Complexes from Density Functional Theory Calculations**. *Phys. Rev. B*, **82**:205125, 2010. 58, 63, 69

[75] C. Cao, M. Wu, J. Jiang, and H.-P. Cheng. **Transition Metal Adatom and Dimer Adsorbed on Graphene: Induced Magnetization and Electronic Structures**. *Phys. Rev. B*, **81**:205424, 2010. 58, 63, 69, 95

[76] X. Y. Zhang and J. L. Wang. **Structural, Electronic, and Magnetic Properties of Co_n-$Benzene_m$ Complexes**. *J. Phys. Chem. A*, **112**:296–304, 2008. 58, 61, 95

[77] R. Pandey, B. K. Rao, P. Jena, and M. A. Blanco. **Electronic Structure and Properties of Transition Metal-Benzene Complexes**. *J. Am. Chem. Soc.*, **123**:3799–3808, 2001. 58, 61

[78] R. Pandey, B. K. Rao, P. Jena, and J. M. Newsam. **Unique Magnetic Signature of Transition Metal Atoms Supported on Benzene**. *Chem. Phys. Lett.*, **321**:142–150, 2000. 58, 61

[79] K. Morgenstern, J. Kibsgaard, J. V. Lauritsen, E. Laegsgaard, and F. Besenbacher. **Cobalt Growth on Two Related Close-Packed Noble Metal Surfaces**. *Surf. Sci.*, **601**:1967–1972, 2007. 58

[80] R. Decker, U. Schlickum, F. Klappenberger, G. Zoppellaro, S. Klyatskaya, M. Ruben, J. V. Barth, and H. Brune. **Using Metal-Organic Templates to Steer the Growth of Fe and Co Nanoclusters**. *Appl. Phys. Lett.*, **93**:243102–1–3, 2008. 59, 75

[81] U. Schlickum, R. Decker, F. Klappenberger, G. Zoppellaro, S. Klyatskaya, M. Ruben, I. Silanes, A. Arnau, K. Kern, H. Brune, and J. V. Barth. **Metal-Organic Honeycomb Nanomeshes with Tunable Cavity Size**. *Nano Lett.*, **7**:3813–3817, 2007. 59, 71

[82] D. Kühne, F. Klappenberger, R. Decker, U. Schlickum, H. Brune, S. Klyatskaya, M. Ruben, and J. V. Barth. **High-Quality 2D Metal-Organic Coordination Network Providing Giant Cavities Within Mesoscale Domains**. *J. Am. Chem. Soc.*, **131**:3881–3883, 2009. 59, 71, 75, 97, 98

[83] S. Klyatskaya, F. Klappenberger, U. Schlickum, D. Kühne, M. Marschall, J. Reichert, R. Decker, W. Krenner, G. Zoppellaro, H. Brune, J. V. Barth, and M. Ruben. **Surface-Confined Self-Assembly of Di-carbonitrile Polyphenyls**. *Adv. Func. Mat.*, **21**:1230–1240, 2011. 61, 71, 97

[84] M. Marschall, J. Reichert, A. Weber-Bargioni, K. Seufert, W. Auwärter, S. Klyatskaya, G. Zoppellaro, M. Ruben, and J. V. Barth. **Random Two-Dimensional String Networks Based on Divergent Coordination Assembly**. *Nat. Chem.*, **2**:131–137, 2010. 61, 71

[85] S. Clair, S. Pons, S. Fabris, S. Baroni, H. Brune, K. Kern, and J. V. Barth. **Monitoring Two-Dimensional Coordination Reactions: Directed Assembly of Co-Terephthalate Nanosystems on Au(111)**. *J. Phys. Chem. B*, **110**:5627–5632, 2006. 61

[86] J. Kliewer, R. Berndt, J. Minár, and H. Ebert. **Scanning Tunnelling Microscopy and Electronic Structure of Mn Clusters on Ag(111)**. *Appl. Phys. A: Mater. Sci. Process.*, **82**:63–66, 2006. 63

[87] N. N. Negulyaev, V. S. Stepanyuk, L. Niebergall, P. Bruno, W. Auwärter, Y. Pennec, G. Jahnz, and J. V. Barth. **Effect of Strain Relaxations on Heteroepitaxial Metal-on-Metal Island Nucleation and Superlattice Formation: Fe on Cu(111)**. *Phys. Rev. B*, **79**:195411, 2009. 65

[88] J. V. Barth. **Fresh Perspectives for Surface Coordination Chemistry**. *Surf. Sci.*, **603**:1533 – 1541, 2009. 69

[89] N. Lin, S. Stepanow, M. Ruben, and J. V. Barth. **Surface-Confined Supramolecular Coordination Chemistry**. *Top. Curr. Chem.*, **287**:1–44, 2009. 69, 71

[90] S. Zhang. **Emerging Biological Materials Through Molecular Self-assembly**. *Biotech. Adv.*, **20**:321 – 339, 2002. 71

[91] J. V. Barth, G. Costantini, and K. Kern. **Engineering Atomic and Molecular Nanostructures at Surfaces**. *Nature*, **437**:671–679, 2005. 71

[92] J. V. Barth. **Molecular Architectonic on Metal Surfaces**. *Annu. Rev. Phys. Chem.*, **58**:375–407, 2007. 71

[93] H. Liang, Y. He, Y. Ye, X. Xu, F. Cheng, W. Sun, X. Shao, Y. Wang, J. Li, and K. Wu. **Two-dimensional Molecular Porous Networks Constructed by Surface Assembling**. *Coord. Chem.y Rev.*, **253**:2959 – 2979, 2009. 71

[94] J. K. Gimzewski, C. Joachim, R. R. Schlittler, V. Langlais, H. Tang, and I. Johannsen. **Rotation of a Single Molecule Within a Supramolecular Bearing**. *Science*, **281**:531–533, 1998. 71

[95] N. Wintjes, D. Bonifazi, F. Cheng, A. Kiebele, M. Stöhr, T. Jung, H. Spillmann, and F. Diederich. **A Supramolecular Multiposition Rotary Device**. *Angew. Chem. Int. Ed.*, **119**:4167–4170, 2007. 71

[96] D. Kühne, F. Klappenberger, W. Krenner, S. Klyatskaya, M. Ruben, and J.V. Barth. **Rotational and Constitutional Dynamics of Caged Supramolecules**. *Proc. Natl. Acad. Sci. U. S. A.*, **50**:21332–21336, 2010. 71, 75, 83, 97, 98, 113, 115

[97] H. L. Tierney, C. J. Murphy, A. D. Jewell, A. E. Baber, E. V. Iski, H. Y. Khodaverdian, A. F. McGuire, N. Klebanov, and E. C. H. Sykes. **Experimental Demonstration of a Single-molecule Electric Motor**. *Nat. Nano.*, **6**:625–629, 2011. 71

[98] M. Mannini, F. Pineider, P. Sainctavit, C. Danieli, E. Otero, C. Sciancalepore, A. M. Talarico, M.-A. Arrio, A. Cornia, D. Gatteschi, and R. Sessoli. **Magnetic Memory of a Single-Molecule Quantum Magnet Wired to a Gold Surface**. *Nat. Mater.*, **8**:194–197, 2009. 71

[99] A. R. Rocha, V. M. Garcia-Suarez, S. W. Bailey, C. J. Lambert, J. Ferrer, and S. Sanvito. **Towards Molecular Spintronics**. *Nat. Mater.*, **4**:335–339, 2005. 71

[100] J. Kong, N. R. Franklin, C. Zhou, M. G. Chapline, S. Peng, K. Cho, and H. Dai. **Nanotube Molecular Wires as Chemical Sensors**. *Science*, **287**:622–625, 2000. 71

[101] O.K. Varghese, P.D. Kichambre, D. Gong, K.G. Ong, E.C. Dickey, and C.A. Grimes. **Gas Sensing Characteristics of Multi-wall Carbon Nanotubes**. *Sensor Actuat. B-Chem.*, **81**:32 – 41, 2001. 71

[102] K. Seufert, W. Auwärter, and J. V. Barth. **Discriminative Response of Surface-Confined Metalloporphyrin Molecules to Carbon and Nitrogen Monoxide**. *J. Am. Chem. Soc.*, **132**:18141–18146, 2010. 71

[103] K. Seufert, M.-L. Bocquet, W. Auwärter, A. Weber-Bargioni, J. Reichert, N. Lorente, and J. V. Barth. **Cis-dicarbonyl Binding at Cobalt and Iron Porphyrins with Saddle-shape Conformation**. *Nat. Chem.*, **3**:114–119, 2011. 71

[104] M. E. Cañas-Ventura, X. Wende, D. Wasserfallen, K. Müllen, H. Brune, J. V. Barth, and R. Fasel. **Self-Assembly of Periodic Bicomponent Wires and Ribbons**. *Angew. Chem. Int. Ed.*, **46**:1814–1818, 2007. 71

[105] A. Schiffrin, J. Reichert, W. Auwärter, G. Jahnz, Y. Pennec, A. Weber-Bargioni, V. S. Stepanyuk, L. Niebergall, P. Bruno, and J. V. Barth. **Self-Aligning Atomic Strings in Surface-Supported Biomolecular Gratings**. *Phys. Rev. B*, **78**:035424, 2008. 71

[106] D. Kühne, F. Klappenberger, R. Decker, U. Schlickum, H. Brune, S. Klyatskaya, M. Ruben, and J. V. Barth. **Self-Assembly of Nanoporous Chiral Networks with Varying Symmetry from Sexiphenyl-dicarbonitrile on Ag(111)**. *J. Phys. Chem. C*, **113**:17851–17859, 2009. 71, 75, 80, 81, 83, 97

[107] D. Philp and J. F. Stoddart. **Self-Assembly in Natural and Unnatural Systems**. *Angew. Chem. Int. Ed.*, **35**:1155–1196, 1996. 72

[108] A. Aggeli, I. A. Nyrkova, M. Bell, R. Harding, L. Carrick, T. C. B. McLeish, A. N. Semenov, and N. Boden. **Hierarchical Self-assembly of Chiral Rod-like Molecules as a Model for Peptide β-sheet Tapes, Ribbons, Fibrils, and Fibers**. *Proc. Natl. Acad. Sci. U. S. A.*, **98**:11857–11862, 2001. 72

[109] T. Kawasaki, M. Tokuhiro, N. Kimizuka, and T. Kunitake. **Hierarchical Self-Assembly of Chiral Complementary Hydrogen-Bond Networks in Water: Reconstitution of Supramolecular Membranes**. *J. Am. Chem. Soc.*, **123**:6792–6800, 2001. 72

[110] J. A. A. W. Elemans, A. E. Rowan, and R. J. M. Nolte. **Mastering Molecular Matter. Supramolecular Architectures by Hierarchical Self-Assembly**. *J. Mater. Chem.*, **13**:2661–2670, 2003. 72

[111] Y. He, T. Ye, M. Su, C. Zhang, A. E. Ribbe, W. Jiang, and C. Mao. **Hierarchical Self-assembly of DNA into Symmetric Supramolecular Polyhedra**. *Nature*, **452**:198–201, 2008. 72

[112] T. P. J. Knowles, T. W. Oppenheim, A. K. Buell, D. Y. Chirgadze, and M. E. Welland. **Nanostructured Films from Hierarchical Self-assembly of Amyloidogenic Proteins**. *Nat. Nano.*, **5**:204–207, 2010. 72

[113] H. Spillmann, A. Dmitriev, N. Lin, P. Messina, J. V. Barth, and K. Kern. **Hierarchical Assembly of Two-Dimensional Homochiral Nanocavity Arrays**. *J. Am. Chem. Soc.*, **125**:10725–10728, 2003. 72

[114] G. Ashkenasy, R. Jagasia, M. Yadav, and M. R. Ghadiri. **Design of a Directed Molecular Network**. *Proc. Natl. Acad. Sci. U. S. A.*, **101**:10872–10877, 2004. 72

[115] M. Ruben, U. Ziener, J.-M. Lehn, V. Ksenofontov, P. Gätlich, and G. B. M. Vaughan. **Hierarchical Self-Assembly of Supramolecular Spintronic Modules into 1D- and 2D-Architectures with Emergence of Magnetic Properties**. *Chem. Eur. J.*, **11**:94–100, 2005. 72

[116] M.-C. Blüm, E. Čavar, M. Pivetta, F. Patthey, and W.-D. Schneider. **Conservation of Chirality in a Hierarchical Supramolecular Self-Assembled Structure with Pentagonal Symmetry**. *Angew. Chem. Int. Ed.*, **44**:5334–5337, 2005. 72

[117] S. Clair, S. Pons, H. Brune, K. Kern, and J. V. Barth. **Mesoscopic Metallosupramolecular Texturing by Hierarchic Assembly**. *Angew. Chem. Int. Ed.*, **44**:7294–7297, 2005. 72

[118] P. A. Staniec, L. M. A. Perdigao, A. Saywell, N. R. Champness, and P. H. Beton. **Hierarchical Organisation on a Two-dimensional Supramolecular Network**. *ChemPhysChem*, **8**:2177–2181, 2007. 72

[119] D. Ećija, K. Seufert, D. Heim, W. Auwärter, C. Aurisicchio, C. Fabbro, D. Bonifazi, and J. V. Barth. **Hierarchic Self-Assembly of Nanoporous Chiral Networks with Conformationally Flexible Porphyrins**. *ACS Nano*, **4**:4936–4942, 2010. 72

[120] H. Liang, W. Sun, X. Jin, H. Li, J. Li, X. Hu, B. K. Teo, and K. Wu. **Two-Dimensional Molecular Porous Networks Formed by Trimesic Acid and 4,4'-Bis(4-pyridyl)biphenyl on Au(111) through Hierarchical Hydrogen Bonds: Structural Systematics and Control of Nanopore Size and Shape**. *Angew. Chem. Int. Ed.*, **50**:7562–7566, 2011. 72

[121] H. L. Zhang, W. Chen, H. Huang, L. Chen, and A. T. S. Wee. **Preferential Trapping of C60 in Nanomesh Voids**. *J. Am. Chem. Soc.*, **130**:2720–2721, 2008. 72

[122] L. Kampschulte, T. L. Werblowsky, R. S. K. Kishore, M. Schmittel, W. M. Heckl, and M. Lackinger. **Thermodynamical Equilibrium of Binary Supramolecular Networks at the Liquid-Solid Interface**. *J. Am. Chem. Soc.*, **130**:8502–8507, 2008. 72

[123] Z. Shi and N. Lin. **Structural and Chemical Control in Assembly of Multicomponent Metal-Organic Coordination Networks on a Surface**. *J. Am. Chem. Soc.*, **132**:10756–10761, 2010. 72

[124] S. Jensen, J. Greenwood, H. A. Früchtl, and C. J. Baddeley. **STM Investigation on the Formation of Oligoamides on Au111 by Surface-Confined Reactions of Melamine with Trimesoyl Chloride**. *J. Phys. Chem. C*, **115**:8630–8636, 2011. 72

[125] Z. Shi, T. Lin, J. Liu, P. N. Liu, and N. Lin. **Regulating a Two-dimensional Metallo-supramolecular Self-assembly of Multiple Outputs**. *CrystEngComm*, **13**:5532–5534, 2011. 72

[126] W. Krenner, F. Klappenberger, N. Kepčija, E. Arras, Y. Makoudi, D. Kühne, S. Klyatskaya, M. Ruben, and J.V. Barth. **Unraveling the Hierarchic Formation of Open-porous Bimolecular Networks**. *J. Phys. Chem C*, **116**:16421–16429, 2012. 72

[127] X. Gonze, G.-M. Rignanese, M. Verstraete, J.-M. Beuken, Y. Pouillon, R. Caracas, F. Jollet, M. Torrent, G. Zerah, M. Mikami, Ph. Ghosez, M. Veithen, J.-Y. Raty, V. Olevano, F. Bruneval, L. Reining, R. Godby, G. Onida, D.R. Hamann, and D.C. Allan. **A Brief Introduction to the ABINIT Software Package.** *Zeit. Kristallogr.*, **220**:558–562, 2005. 74

[128] M. Torrent, F. Jollet, F. Bottin, G. Zerah, and X. Gonze. **Implementation of the Projector Augmented-Wave Method in the ABINIT code. Application to the study of iron under pressure.** *Comput. Mat. Science*, **42**:337, 2008. 74

[129] Y. Makoudi, E. Arras, N. Kepčija, W. Krenner, S. Klyatskaya, F. Klappenberger, M. Ruben, A. P. Seitsonen, and J. V. Barth. **Hierarchically Organized Bimolecular Ladder Network Exhibiting Guided One-Dimensional Diffusion**. *ACS Nano*, **6**:549–556, 2012. 90

[130] L. Bürgi, O. Jeandupeux, H. Brune, and K. Kern. **Probing Hot-Electron Dynamics at Surfaces with a Cold Scanning Tunneling Microscope**. *Phys. Rev. Lett.*, **82**:4516–4519, 1999. 91

[131] T.-M. Chuang, M. P. Allan, Jinho Lee, Yang Xie, Ni Ni, S. L. Bud'ko, G. S. Boebinger, P. C. Canfield, and J. C. Davis. **Nematic Electronic Structure in the "Parent" State of the Iron-Based Superconductor Ca($Fe_{1x}Co_x$)$_2As_2$**. *Science*, **327**:181–184, 2010. 91

[132] L. Scudiero, D. E. Barlow, U. Mazur, and K. W. Hipps. **Scanning Tunneling Microscopy, Orbital-Mediated Tunneling Spectroscopy, and Ultraviolet Photoelectron Spectroscopy of Metal(II) Tetraphenylporphyrins Deposited from Vapor**. *J. Am. Chem. Soc.*, **123**:4073–4080, 2001. 91

[133] A. Weber-Bargioni, W. Auwärter, F. Klappenberger, J. Reichert, S. Lefrançois, T. Strunskus, C. Wöll, A. Schiffrin, Y. Pennec, and J. V. Barth. **Visualizing the Frontier Orbitals of a Conformationally Adapted Metalloporphyrin**. *ChemPhysChem*, **9**:89–94, 2008. 91

[134] W. Auwärter, K. Seufert, F. Klappenberger, J. Reichert, A. Weber-Bargioni, A. Verdini, D. Cvetko, M. Dell'Angela, L. Floreano, A. Cossaro, G. Bavdek, A. Morgante, A. P. Seitsonen, and J. V. Barth. **Site-specific Electronic and Geometric Interface Structure of Co-tetraphenylporphyrin Layers on Ag(111)**. *Phys. Rev. B*, **81**:245403, 2010. 91

[135] J. Kliewer, R. Berndt, and S. Crampin. **Scanning Tunnelling Spectroscopy of Electron Resonators**. *New J. Phys.*, **3**:22, 2001. 92, 117

[136] J. T. Li, W. D. Schneider, and R. Berndt. **Local Density of States from Spectroscopic Scanning Tunneling Microscope Images: Ag(111)**. *Phys. Rev. B*, **56**:7656–7659, 1997. 92, 103, 117, 126, 127

[137] K. Morgenstern, K.-F. Braun, and K.-H. Rieder. **Surface-State Depopulation on Small Ag(111) Terraces**. *Phys. Rev. Lett.*, **89**:226801, 2002. 92, 93

[138] F. Klappenberger, D. Kühne, M. Marschall, S. Neppl, W. Krenner, A. Nefedov, T. Strunskus, K. Fink, C. Wöll, S. Klyatskaya, O. Fuhr, M. Ruben, and J. V. Barth. **Uniform π-System Alignment in Thin Films of Template-Grown Dicarbonitrile-Oligophenyls**. *Adv. Funct. Mater.*, **21**:1631–1642, 2011. 97

[139] D. Kühne. *Self-Assembly of Para-sexiphenyl-dicarbonitrile on Ag(111)*. PhD thesis, Technische Universität München, 2011. 97, 109, 110, 113

[140] O. Jeandupeux, L. Bürgi, A. Hirstein, H. Brune, and K. Kern. **Thermal damping of quantum interference patterns of surface-state electrons**. *Phys. Rev. B*, **59**:15926–15934, 1999. 103

[141] M.A. Schneider, L. Vitali, P. Wahl, N. Knorr, L. Diekhöner, G. Wittich, M. Vogelgesang, and K. Kern. **Kondo State of Co Impurities at Noble Metal Surfaces**. *Appl. Phys. A: Mater. Sci. Process.*, **80**:937–941, 2005. 110

[142] J. Wang, L. Zhu, X. Zhang, and M. Yang. **Size- and Shape-Dependent Polarizabilities of Sandwich and Rice-Ball Co_nBz_m Clusters from Density Functional Theory**. *J. Phys. Chem. A*, **112**:8226–8230, 2008. 113

[143] K. Imura, H. Ohoyama, and T. Kasai. **Structures and Its Dipole Moments of Half-sandwich Type Metal-Benzene (1:1) Complexes Determined by 2-m Long Electrostatic Hexapole**. *J. Chem. Phys.*, **301**:183–187, 2004. 113

[144] S. Crampin, M. Nekovee, and J. E. Inglesfield. **Embedding Method for Confined Quantum Systems**. *Phys. Rev. B*, **51**:7318–7320, 1995. 115

[145] K. K. Gomes, W. Mar, W. Ko, F. Guinea, and H. C. Manoharan. **Designer Dirac Fermions and Topological Phases in Molecular Graphene**. *Nature*, **483**:306–310, 2012. 131

Acknowledgments

I would like to thank everybody who directly or indirectly contributed to the development and conclusion of this thesis and PhD project. Over the past years, many people helped me succeed with my work and research. You made this time very constructive, fulfilling and joyful, therefore it is a great privilege and pleasure for me to express my gratitude to all of you. I am especially thankful and eternally grateful to:

- My supervisor Prof. Johannes V. Barth for giving me the opportunity to work in the field of surface science, which was a completely new area of physics for me, when I started working at E20. Thank you for giving me the privilege to experience this great and stimulating environment at the cutting edge of science.
- Dr. Florian Klappenberger and Dr. Dirk Kühne for introducing me to STM and surface science. You were and are great colleagues, mentors and friends. Thank you for teaching me a lot of new things and helping me grasp the new challenges that I was facing. It was always a pleasure to spend time with you in- and outside the lab.
- Claudia Majer, Daniel Gerster, Dirk Kühne, Knud Seufert, Matthias Marschall, Sebastian Jakob, and finally Richard Steinacher - the people in the greatest office in the world. Thank you for creating a great environment to work and spend time in. It was also always a great pleasure to kill time with you in- and outside of work, as the time we kill keeps us alive. The same goes for Felix Bischoff and Florian Blobner, who dropped by ever so often, but just for a little while.

- Dr. Willi Auwärter and Dr. Joachim Reichert for being great colleagues and also for passing on their expertise on what conferences are supposed to be like.

- Prof. Peter Feulner for helping whenever, wherever and however he could with his vast knowledge and wisdom.

- Peter Weber for his support to set up the JT-STM as well as the people working on this project at SPECS, especially Simon Rast and Nils Henningsen.

- Dr. Younes Makoudi, Dr. Emmanuel Arras, and Nenad Kepčija - it was great working with you, thank you for your expertise, support, and contributions.

- Prof. Mario Ruben and Dr. Svetlana Klyatskaya at the Institute of Nanotechnology in Karlsruhe for contributing great ideas, synthesizing molecules, and a very fruitful collaboration.

- Prof. Andrés Arnau, Prof. Javier García de Abajo, and Dr. Iñaki Silanes for their expertise in the theoretical modeling of surface state electron confinement.

- Prof. Douglas Bonn, Prof. Sarah Burke, Dr. Yan Pennec, Adam Shaw, Katherine Cochrane, Stephanie Grothe, Ben MacLeod, Graeme Adamson, and Gregory McMurtrie for the great time I could enjoy in Vancouver at AMPEL and the University of British Columbia. Time really flies.

- Kamila Wilson and Viktoria Blaschek for not having me worry about paperwork and other everyday nuisances.

- Everyone at E20 for the great time and making everyday life more than worthwhile.

- The TUM IAS and IGSSE for their great work and financial support.

- My parents, Hans and Therese, for their love, support, advice and understanding.
- My brother Hubert and our newly extended family, Johanna and Ludwig, for providing some perspective at times and always having an open ear.
- My brother Michael for rocking.
- Florian, Hans-Martin, Johannes, Marc, Markus, Max, and Tobias for all the Wednesday nights and the other days of the week.
- Andreas K., Andreas S., David, Sebastian, Stefan, and Tom for the second best thing in the world.
- All the people with whom I crossed paths but unintentionally forgot to mention.

I hope you all enjoyed the last years as much as I did. Thank you.